Isern, A.R., Anselmetti, F.S., Blum, P., et al., 2002
Proceedings of the Ocean Drilling Program, Initial Reports Volume 194

5. Site 1194[1]

Shipboard Scientific Party[2]

INTRODUCTION

Site 1194 (proposed Site CS-02A; Fig. F1) lies on regional line MAR13 (shotpoint [SP] 3951) and at the crossing of line MAR24 (SP 355) and MAR27 (SP 1123) in 368 m of water (Fig. F2). The site is located ~31 km east of Site 1193 (Fig. F2). Two holes were drilled at this site. Hole 1194A penetrated 169.9 meters below seafloor (mbsf), and Hole 1194B penetrated 427.1 mbsf. Recovery was 100% until a hardground was encountered at 115 mbsf, below which recovery dropped to ~25% for the remainder of the drilled interval. The sediments at this site were early Miocene to Pleistocene in age and predominantly hemipelagic, with a 60 m interval of late Miocene neritic sediments (117.4–177 mbsf). Approximately 3 m of acoustic basement, which consisted of reddish black, metamorphosed rhyolitic rocks, was recovered at Hole 1194B.

Drilling at Site 1194 provided information on the age and facies making up Megasequences A, B, and D. This site was primarily located to investigate the growth history of the northern carbonate platform recorded in the adjacent marginal slope sediments. The prominent horizon overlying these slope sediments can be traced to the drowning unconformity on the adjacent platform recovered at Site 1193. At Site 1194, this horizon was represented by a submarine hardground surface. This horizon is likely to contain a detailed record of the northern platform drowning. Site 1194 also provided information on the age and duration of the unconformities within the prograding, proximal slope sediments shed from the adjacent platform that are part of Megasequence B; the age of Megasequence A that represents the initial marine transgression over basement; and the nature of the basement.

F1. Bathymetry map, p. 32.

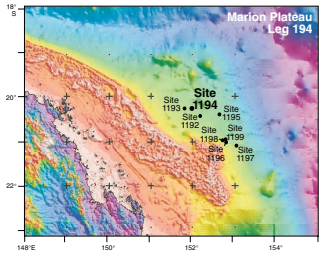

F2. Seismic line MAR13, p. 33.

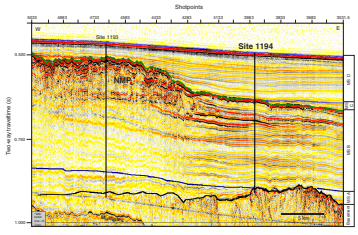

[1]Examples of how to reference the whole or part of this volume.
[2]Shipboard Scientific Party addresses.

Ms 194IR-105

OPERATIONS

A beacon was dropped at Site 1194 (proposed Site CS-02A) at 2253 hr on 22 January 2001. The corrected precision depth recorder depth was 377 meters below sea level.

Hole 1194A

Hole 1194A was spudded with the advanced piston corer (APC) at 0350 hr on 23 January and established a water depth of 374 m (Table T2, p. 87, in the "Leg 194 Summary" chapter; Tables T1, T2). Piston coring advanced to refusal depth at 117.4 mbsf, with the last core advancing only 8.2 m. The average recovery for the piston cored interval was 104.1%. Downhole temperature measurements were taken at 33.2, 61.7, 90.2, and 117.4 mbsf. Cores were oriented starting with Core 4H.

The hole was deepened with the extended core barrel (XCB) system. At 145.3 mbsf, the drill string became stuck, and circulation was lost. After working the stuck pipe for 30 min and applying as much as 40 kilopounds of overpull, limited circulation was regained. It was obvious from the higher pump pressure (a 550-psi increase), that several, if not all, of the bit nozzles were plugged. Coring resumed but was terminated at 169.9 mbsf because of poor recovery. The overall penetration with the XCB was 52.5 m, and the average recovery was 7.6%. Inspection of the bit revealed that all four bit nozzles were still plugged with sediment.

T1. Coring summary, p. 87.

T2. Expanded coring summary, p. 88.

Hole 1194B

The vessel was offset 20 m east of Hole 1194A. Hole 1194B was spudded with the rotary core barrel (RCB) system at 0235 hr on 24 January and drilled ahead with a wash barrel to 110.0 mbsf. RCB coring advanced without incident to the target depth at 427.1 mbsf. Basement was penetrated at 426 mbsf. The cored interval for this hole was 317.1 m; average recovery was 28.1%. After the hole was flushed with a 40-barrel (bbl) sepiolite sweep, the bit was released on bottom, the hole was displaced with 127 bbl of sepiolite mud, and the drill pipe was pulled up to logging depth. Wireline logging operation in Hole 1194B started at 0530 hr on 25 January. The triple combination (triple combo; natural gamma ray, density, porosity, and resistivity) tool string was deployed with the Lamont-Doherty Earth Observatory (LDEO) temperature tool at the bottom and the LDEO multichannel gamma ray logging tool at the top. The hole size varied from 13 in at the bottom to 17 in in the middle portion. The tools reached total depth at 423 mbsf.

The Formation MicroScanner (FMS) and dipole shear sonic imager (DSI) were deployed for the second run. Problems with the DSI precluded the collection of sonic data. One successful pass was completed with the FMS before the DSI was replaced with the long-spaced sonic logging (LSS) tool. A tight spot at ~230 mbsf was passed after several attempts.

A check shot survey with the well seismic tool (WST) was the third run. Because this is a light tool, it is difficult to move it beyond obstructions. The plan for this log was to compare the signals of the water gun with those of the air gun. The air gun developed a serious leak, so only the water gun could be used. Downhole measurements were also complicated because of a strong current that generated considerable drill

string vibration. The end of the drill pipe was placed at 78.2 mbsf, and the deepest station was at 156.2 mbsf. Software problems were also encountered with the selection of the arrival waveforms from the water gun. Stacks were made at three stations, but the data were not very good. The plan for the remainder of Leg 194 sites was to use the air gun after it was repaired. Logging operations ended at 0030 hr on 26 January.

After rigging down from logging, the drill string was retrieved and the beacon was recovered. The vessel departed for Site 1195 at 0242 hr on 26 January.

LITHOSTRATIGRAPHY AND SEDIMENTOLOGY

Site 1194 was drilled through a sequence of hemipelagic drift deposits into underlying slope-sediments of the Northern Marion Platform (NMP) as indicated on seismic profiles (see "Seismic Stratigraphy," p. 27). The ~420-m-thick sediment sequence was divided into six units according to variations in sedimentological structures and texture, grain size, inferred organic matter content, terrigenous material content, and biotic assemblages (Fig. F3; Table T3).

Unit I is characterized by 3.8 m of yellow skeletal grainstone, with a sharp boundary to a 114-m-thick hemipelagic mudstone/wackestone interval (Unit II). Unit III is capped by a ferromanganese hardground and consists of a bryozoan/foraminifer dominated packstone/floatstone interval. Unit III was initiated on the upper slope, developing into a middle to inner neritic ramp at the top of the unit. Unit IV is characterized by very fine grained packstone to grainstone with skeletal components, suggesting abrasion during transport. Unit V consists of weakly layered grainstone, with bioturbation often crosscutting the layering. Unit VI, representing acoustic basement, consists of a reddish olivine basalt.

Most of the sediments recovered at Site 1194 are poorly to moderately lithified. Core recovery at this site is good above 117 mbsf and poor below this depth. The drop in recovery corresponds to seismic Megasequence Boundary B/D (see "Seismic Stratigraphy," p. 27), which was inferred to be an exposure surface/hardground that correlates with the boundary between lithologic Units II and III.

Lithologic Units

Unit I (0–3.8 mbsf; Pleistocene)

Unit I consists of 3.8 m of pale yellow, well-sorted skeletal grainstone (Fig. F3). Skeletal components are dominated by planktonic foraminifers but include benthic foraminifers, pteropods, echinoids, and gastropods (Fig. F4). The base of this unit is erosional as indicated by the presence of a scoured surface.

Unit II (3.8–117.4 mbsf; Pliocene to Late Miocene)

Unit II consists of 114 m of light olive to greenish gray mudstone/wackestone interbedded with minor packstone intervals (Figs. F3, F5). Skeletal components are dominated by planktonic foraminifers. Benthic foraminifers are common, whereas shell and echinoids fragments are rare. Overall, skeletal components are coarse sand sized, and

F3. Lithologic summary, p. 34.

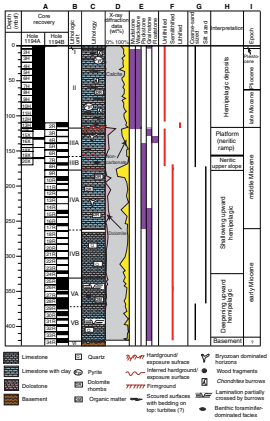

T3. Lithologic units and subunits, p. 93.

F4. Skeletal grainstone of Unit I, p. 35.

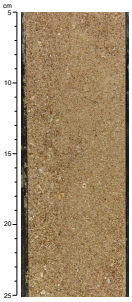

F5. Close-up photograph of Unit II, p. 36.

the matrix is clay to silt sized. Dolomite rhombs are rare. Well-preserved wood fragments are observed at the bottom and the top of Unit II. Black stains ~1 cm in diameter occur throughout this unit. Smear slide analysis revealed that these are nonoxidized framboidal pyrite infilling structures similar to burrows. Bioturbation is extensive in this unit, with common Chondrites and rare *Thalassinoides, Taenidium,* and *Zoophycus*.

Scoured surfaces overlain by coarse sand–sized calcareous sediment, typically 1–5 cm thick, are observed at five different levels within this unit (see Fig. F3, column C, 35–105 mbsf, and Fig. F6).

Unit III (117.4–177.3 mbsf, Middle Miocene)

Unit III is 60 m thick and includes two subunits identified by their biotic assemblage (Fig. F3). Both subunits consist of skeletal packstone, comprising coarse sand–sized skeletal components in a dark gray matrix indicating the presence of terrigenous clay. A 1-m-thick hardground (see below) marks the boundary between Unit II and Unit III. This interval is considered to be a depositional hiatus developed through the alteration of Unit III sediments and as such was included in Subunit IIIA.

Subunit IIIA (117.4–158.0 mbsf)

The top of Subunit IIIA consists of a 1-m-thick interval, which has a sharp, scoured surface coated with a 1-cm-thick reddish brown crust (Fig. F7). A 10-cm-deep and 2-cm-wide fissure filled with fine-grained pale yellow carbonate sediment occurs in this surface. The dark reddish brown crust is composed of wavy phosphatic and ferromanganese laminae, as can be seen in thin section (Fig. F8). The underlying 1-m-thick interval is extensively dolomitized (Fig. F3, column C, and Fig. F9), with up to 40 wt% dolomite (see "Geochemistry," p. 16). Dolomite appears to be mostly confined to skeletal particles, and no dolomitized cement was observed. This dolomitized interval consists of a pale yellow skeletal grainstone with quartz, bryozoans, small benthic foraminifer fragments, and molds of gastropods. Other skeletal components are not identifiable in hand samples, possibly because of recrystallization and/or fragmentation. Thin section analysis reveals that the hardground is composed of well-preserved organisms mixed with angular quartz. Cements consist mainly of syntaxial overgrowths on high-Mg calcite particles that later recrystallize to single-crystal low-Mg calcite (Fig. F10). Calcite cement, typical of the vadose zone, was not found. Glauconitized bioclasts are common in this interval, which has a distinct uranium peak in the downhole natural gamma ray log (see "Downhole Measurements," p. 22) that is typical of hardgrounds. A second interval, which was not recovered in the cores, has a similar natural gamma ray signature in the downhole logs at ~160 mbsf (Subunit IIIB). This second interval was included in the lithologic column of this site (Fig. F3, column D).

From 118.4 to 158 mbsf, Subunit IIIA consists of 30 m of dark gray packstone overlain by a 10-m-thick interval of skeletal floatstone (Figs. F11, F12). Skeletal components within Subunit IIIA are dominated by well-preserved bryozoans. Bivalve fragments are common, and benthic foraminifers are present.

F6. Close-up photograph of scoured surfaces in Section 194-1194A-1H-1, p. 37.

F7. Close-up photograph of hardground interval at the top of Unit III, p. 38.

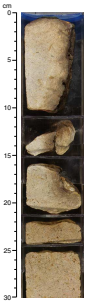

F8. Photomicrograph of the top of recovered hardground in Core 194-1194A-14X, p. 39.

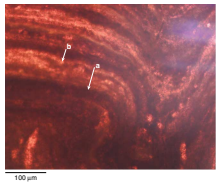

F9. Close-up photograph of dolomitized interval below the phosphatized crust of Unit III, p. 40.

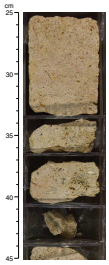

Subunit IIIB (158.0–177.3 mbsf)

The main difference between Subunits IIIA and IIIB is the near-total absence of bryozoans and the predominance of benthic foraminifers in the latter interval. This subunit is composed of skeletal packstone with clay and coarse sand–sized skeletal components dominated by small benthic foraminifers. Although most skeletal fragments are well preserved, minor amounts of silt-sized, unidentifiable skeletal components first occur downcore in this subunit (Fig. F13).

Unit IV (177.3–331.1 mbsf; Early–Middle Miocene)

This unit consists of 153.8 m of silt-sized packstone to grainstone (Fig. F3). It is capped by a 1-cm-thick layer of grainstone with a sharp contact to Subunit IIIB. Skeletal components are not identifiable in hand samples because of extensive fragmentation and/or recrystallization, which is the characteristic feature of this unit. Unit IV was divided into two subunits based on mineralogy and clay content.

Subunit IVA (177.3–264.5 mbsf; Late Early–Middle Miocene)

This subunit consists of light olive-gray silt-sized packstone (Figs. F14, F15). The bottom of the interval has a packstone/grainstone texture. No skeletal components are identifiable except for an interval at ~230 mbsf, which is rich in bryozoans. Dolomitic rhombs are abundant in smear slides, suggesting partial dolomitization or transport of dolomitized material. This interval is rich in clay (up to 50 wt% noncarbonate components; see "Geochemistry," p. 16; Fig. F3, column C) and is well sorted.

Subunit IVB (264.5–331.1 mbsf; Early Miocene)

This subunit is distinctive because of the common occurrence of angular quartz sand (Figs. F16, F17). It consists of well-cemented, silt-sized grainstone that is partially dolomitized (see Fig. F3, column C). The interval is moderately well sorted and shows neither bioturbation nor layering. Glauconite is common and is often observed to be infilling burrows. Clay is absent.

Unit V (331.1–421.1 mbsf; Early Miocene)

This 90-m-thick packstone unit (Fig. F3) features centimeter-scale dark layers. Clay was not observed in Unit V. Bioturbation is common but not extensive as shown by the partial preservation of layering. The burrows and layering distinguish Unit V from previous units. Based on grain size, quartz content, and color variation, this unit was divided into two subunits.

Subunit VA (331.1–372.1 mbsf)

The distinctive feature of Subunit VA is the dominance of silt-sized components (Figs. F18, F19). The sediments are primarily greenish gray packstone with skeletal components that are not identifiable in a hand sample because of extensive fragmentation/recrystallization. One wood fragment was found.

F10. Photomicrograph of the recovered hardground in Core 194-1194A-14X, p. 41.

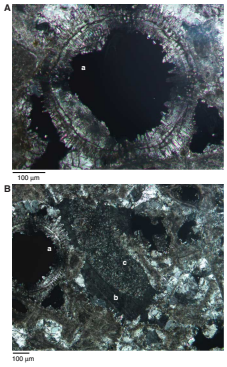

F11. Close-up photograph of skeletal floatstone of Subunit IIIA, p. 42.

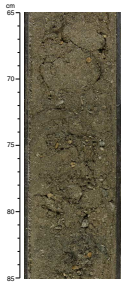

F12. Photomicrograph of the lithology of Subunit IIIA, p. 43.

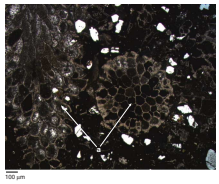

F13. Close-up photograph of skeletal packstone dominated by larger benthic foraminifers, p. 44.

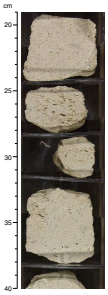

Subunit VB (372.1–421.1 mbsf)

This subunit is composed of well-sorted, light greenish gray to pale yellow skeletal packstone (Figs. F20, F21). The major difference between Subunits VA and VB is that, in the latter, skeletal components are coarse sand–sized. Planktonic foraminifers are the dominant skeletal particles for the upper part of the subunit with larger benthic foraminifers increasing in importance downsection and becoming dominant in the 2-m interval immediately overlying the basement. In this 2-m interval, a robust, thick-walled shallow-water form of the larger foraminifer *Lepidocyclina* dominates (Fig. F22). This foraminifer occurs in discrete, parallel-laminated fining-upward sequences. About half of the *Lepidocyclina* are filled with glauconite, indicating potential reworking of the species within Subunit VB. Quartz is rare to absent.

Unit VI (421.1–? mbsf)

This unit consists of 3 m of olivine basalt basement (Figs. F3, F23, F24). The lithology is a reddish black, amygdaloidal extrusive rock with olivine, feldspar, and epidote. Several generations of cracks filled with calcite are visible.

Discussion

Unit I

The predominance of coarse-grained skeletal particles, the absence of mud, the high degree of sorting, and the erosive boundary to Unit II suggest that Unit I is winnowed. This unit was likely to have been deposited on a current-swept seafloor. It is laterally equivalent to Unit I at Sites 1192 and 1193 (see **"Lithostratigraphy and Sedimentology,"** p. 4, in the "Site 1192" chapter and **"Lithostratigraphy and Sedimentology,"** p. 6, in the "Site 1193" chapter).

Unit II

The scoured surfaces overlain by a centimeter-scale normal graded bed of coarse carbonate sand present within Unit II are interpreted to be gravity flow deposits. This unit was likely deposited in a distal, hemipelagic setting (see **"Biostratigraphy and Paleoenvironments,"** p. 9) with frequent input of coarser sediment from gravity flows. It is laterally equivalent to Unit II at Site 1193 (see **"Lithostratigraphy and Sedimentology,"** p. 6, in the "Site 1193" chapter).

Unit III

The hardground surface separating Units II and III was likely formed in a submarine setting. Evidence to support this interpretation includes boring by organisms, phosphatization, and a positive peak in the uranium curve of gamma ray analysis (see **"Downhole Measurements,"** p. 22). However, the fact that the hardground is submarine does not, in itself, rule out the possibility of subaerial exposure prior to drowning. The question of subaerial exposure of this hardground requires further investigation (e.g., using stable isotopes). Biostratigraphic data indicate that this surface represents a maximum time gap of 4 m.y. Subunit IIIA represents shallow-water deposition possibly on a neritic ramp (~30–50 m water depth) (see **"Biostratigraphy and Paleoenvironments,"** p. 9)

F14. Close-up photograph of silt-sized packstone/grainstone, p. 45.

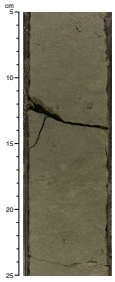

F15. Photomicrograph of Subunit IVA, p. 46.

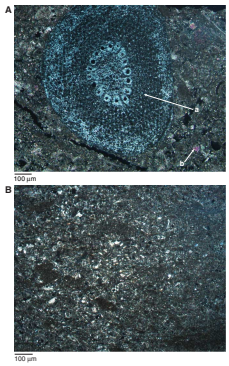

F16. Close-up photograph of the sediment of Subunit IVB, p. 47.

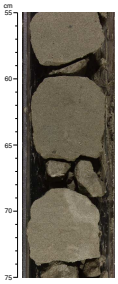

F17. Photomicrograph of Subunit IVB, p. 48.

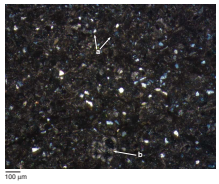

with bryozoans being the dominant organisms. Subunit IIIB was deposited in a deeper setting (~120–200 m) (see **"Biostratigraphy and Paleoenvironments,"** p. 9), such as on a neritic upper slope. Skeletal components are dominated by small benthic foraminifers. The sharp surface at the base of Subunit IIIB is interpreted to be the top of a firmground as supported by the fact that its gamma ray signature resembles that of the previously discussed hardground (see **"Downhole Measurements,"** p. 22). In both subunits the clay fraction is relatively important and the skeletal fragments are still preserved, indicating a low- to medium-energy environment.

Unit IV

Physically abraded silt-sized particles are the dominant bioclasts in Unit IV. This is indicative of long-distance transport in a high-energy environment or possibly of bioerosion. The source for this fine carbonate material could be the NMP or a more distant, time-equivalent carbonate platform. Unit IV was deposited in a hemipelagic setting at water depths ranging from 120 to 200 m (see **"Biostratigraphy and Paleoenvironments,"** p. 9). This range in water depth, together with the seismic geometry of seismic sequences that show gently inclined reflections, imply a slope depositional environment for Unit IV. Overall, a shallowing-upward trend is seen between Units IV and III; water depths of Subunit IVB are weakly constrained, whereas those water depths of Subunits IVA and IIIB ranged between 120 and 200 m. Subunit IIIA was deposited in 30–50 m water depth.

Unit V

Unit V may represent the initial sedimentation on the underlying basement surface and thus maybe a transgressive system tract. This interpretation is supported by the ratio of planktonic to benthic foraminifers showing a gradation from larger benthic, shallow-dwelling species to small benthic species and eventually to a planktonic foraminifer-dominated environment (see **"Biostratigraphy and Paleoenvironments,"** p. 9). This transition takes place over a 20-m interval. The general absence of terrigenous components in this unit is striking, especially when compared with Unit V at Site 1193, where the first lithology over basement is dominated by siliciclastics (see **"Lithostratigraphy and Sedimentology,"** p. 6, in the "Site 1193" chapter). This can be explained by the fact that Site 1194 was located on a basement high that became an island just before the transgression and, thus, during subsequent flooding, had a small siliciclastic source area (see **"Seismic Stratigraphy,"** p. 27, and Fig. **F3,** p. 63, in the "Leg 194 Summary" chapter). A fining-upward trend is seen between Subunits VB and VA, indicative of a deepening-upward sequence. Conditions at the water/sediment interface might have been slightly dysaerobic, an assumption that could explain the darker layers that have been partially burrowed by organisms. The base of the unit is rich in benthic foraminifers, and planktonic foraminifers become increasingly important. Thus, Unit V is interpreted as a shallow marine transgression over a topographic high, eventually developing into an outer neritic setting.

F18. Close-up photograph of silt-sized packstone, p. 49.

F19. Photomicrograph of section in Subunit VA, p. 50.

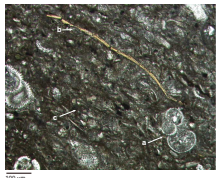

F20. Close-up photograph of skeletal packstone of Subunit VB, p. 51.

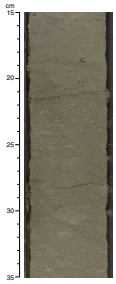

F21. Photomicrograph of skeletal components of the upper part of Subunit VB, p. 52.

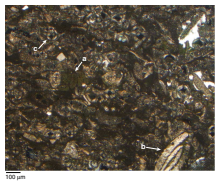

F22. Photomicrograph of lower part of Subunit VA, p. 53.

Unit VI

Thin section analysis of the basement revealed that it consists of an olivine basalt. The well-crystallized porphyries of olivine suggest that this rock was intruded close to the surface, but was not a basaltic flow. It is unclear whether this unit represents Paleozoic extrusive basaltic rocks subsequently metamorphosed during the Tasman orogeny or extrusive rocks linked to early rifting of the Coral Sea Basin (Late Jurassic–Early Cretaceous) (Struckmeyer and Symonds, 1997). However, the general absence of metamorphic minerals and the overall good preservation of the rock seems to favor a synrift or slightly prerift emplacement.

The following geological events were recorded by the succession drilled at Site 1194:

1. During the Early Cretaceous, rifting led to the opening of the Coral Sea. During this phase and/or later, the volcanic basement was subaerially exposed and eroded (Unit VI) and a high was created at the location of Site 1194 (see **"Seismic Stratigraphy,"** p. 27) that, before final flooding, became an elevated island separated from the mainland to the west.
2. During the early Miocene, sea level flooded this elevated area (Subunit VB). However, flooding might have occurred earlier if the resulting sediments were subsequently eroded. As water depth increased, the sediment source became more distant, and thus finer-grained sediments were deposited at Site 1194 (Subunit VA). Seafloor conditions may have been somewhat dysaerobic as shown by the presence of laminations. Additionally, abraded skeletal carbonate particles observed in the recovered sediments may have come from the nearby NMP.
3. During the early to early middle Miocene, sediments were abraded and fragmented to silt size during transport. Rare quartz grains indicate a minor terrigenous influence within this interval. Paleoenvironment data obtained from benthic foraminifers (see **"Biostratigraphy and Paleoenvironments,"** p. 9) indicate a deepening upward toward more clay-rich intervals that is followed by a shallowing-upward succession.
4. In the late middle Miocene, sea level fell and a middle to inner neritic ramp environment developed, where a bryozoan-dominated facies was deposited. Paleowater depth in Subunit IIIA ranges from 30 to 50 m, placing the seafloor in the euphotic zone (Subunit IIIA).
5. A late Miocene (~8–11.5 Ma) sea level lowstand was probably not low enough to expose Unit III to subaerial conditions, but shutdown of the adjacent carbonate factory led to a depositional hiatus. Seismic sequence geometry indicates that flooding of Unit II did not result in immediate deposition but that a time lag occurred between flooding and onset of sedimentation, presumably as a result of current activity (see **"Seismic Stratigraphy,"** p. 27). A phosphatic hardground was formed.
6. During the late late Miocene to Pliocene, hemipelagic, fine-grained sediments were mixed with coarse sand–sized distal mass flow deposits to form Unit II.
7. In the late Pliocene to Pleistocene, strong bottom-water currents swept the seafloor, creating winnowed deposits of skeletal grainstones (Unit I). This process is still active today.

F23. Close-up photograph of weathered olivine basalt, p. 54.

F24. Photomicrograph of the olivine basalt, p. 55.

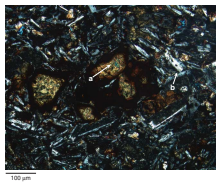

BIOSTRATIGRAPHY AND PALEOENVIRONMENTS

Nannofossils and foraminifers were examined from core catcher samples at Site 1194 and from a number of samples and observations within selected intervals. Table T4 details the nannofossil and planktonic datums used for age assignments. Core catcher samples from Hole 1194A (which penetrated to a depth of 160.3 mbsf) generally contained well-preserved calcareous microfossils ranging from the late Pleistocene to late Miocene. Hole 1194B commenced coring at ~110 mbsf to sample the NMP slope. The calcareous microfossils in this hole are low in abundance to barren and poorly preserved, resulting in loosely constrained biostratigraphic age assignments. Microscopic analysis of biogenic constituents >63 µm, including benthic foraminifers, provided data for paleoenvironmental interpretation (Table T5).

T4. Biostratigraphic datums, p. 94.

T5. Summary of paleoenvironmental interpretations, p. 95.

Calcareous Nannofossils

Calcareous nannofossils are abundant and moderately well preserved from Core 194-1194A-13H upward and are generally rare and poorly preserved below this core. Upper Pliocene through middle Miocene nannofossils were identified, and nine nannofossil datums were established for age-depth construction (Table T4; see "Age Model," p. 15, for age vs. depth and sedimentation rate plots). A brief summary of the nannofossil biostratigraphy is given below.

Discoaster brouweri, Discoaster pentaradiatus, and *Discoaster surculus* were found in Sample 194-1194A-1H-CC. The presence of these taxa in the absence of *Sphenolithus abies* and *Reticulofenestra pseudoumbilica* constrains the age of the sample to 2.6–3.8 Ma (late Pliocene). Much of the Pleistocene and part of the upper Pliocene section thus appears to be missing or very condensed at the site.

The upper Pliocene/lower Pliocene boundary is generally approximated by the last occurrence (LO) of *R. pseudoumbilica,* which is located between Samples 194-1194A-3H-CC and 4H-CC. Both *R. pseudoumbilica* and *S. abies* are common in the lower sample, whereas only the latter species is present in the upper sample. This sequence of occurrences is normal in the tropical ocean. The next nannofossil datum recognized is the LO of *Amaurolithus* spp. (5.6 Ma), between Samples 194-1194A-5H-CC and 6H-CC.

The Miocene/Pliocene boundary, as approximated by the LO of *Discoaster quinqueramus,* is placed between Samples 194-1194A-7H-CC and 8H-CC, based on the presence of the index species in the latter sample. *D. surculus* occurs down to Sample 194-1194A-12H-CC and constrains the age of interval 194-1194A-8H-CC to 12H-CC to 5.6–7.5 Ma. Sample 194-1194A-13H-CC contains *D. quinqueramus* but no *D. surculus* and thus can be assigned an age range of 7.5–8.6 Ma.

Cyclicargolithus floridanus was first encountered in Sample 194-1194A-14X-1, 48–50 cm, suggesting that this sample is older than 11.9 Ma. A hiatus is thus indicated between this sample and the sample above (194-1194A-13X-CC), coinciding with a major lithologic boundary (see "Lithostratigraphy and Sedimentology," p. 3). The upper stratigraphic range of *C. floridanus* is apparently truncated by this hiatus. With the recognition of the LO of *Sphenolithus heteromorphus* (13.6 Ma) at a lower stratigraphic level in Hole 1194B (see below), the duration of the hiatus could be constrained to be 3–6 m.y. long.

Samples from Hole 1194B generally contain few to rare nannofossils. A useful datum identified in this hole is the LO of *S. heteromorphus* between Samples 194-1194B-5R-CC and 9R-CC. The lowest sample from Hole 1194B that enables a relatively useful age determination is Sample 194-1194B-27R-CC, which yielded few nannofossils, including *S. heteromorphus,* which suggests an age range of 13.6–18.2 Ma. The core catcher samples below this level yielded only rare nannofossils, and the low abundance did not allow a reliable determination of the evolutionary first occurrence of *S. heteromorphus*.

Planktonic Foraminifers

Planktonic foraminifers were well preserved and highly abundant in Hole 1194A from Samples 194-1194A-1H-CC through 14H-CC, below which the samples were barren of index fossils. The samples in Hole 1194B have low planktonic abundance (generally <10% sample volume), pervasive crystal overgrowths, and species contamination. Because of this, the planktonic foraminifer biostratigraphy is limited to the interval cored in Hole 1194A.

Hole 1194A

Pulleniatina primalis, Sphaeroidinella dehiscens, and *Globorotalia truncatulinoides* were found in Sample 194-1194A-1H-2, 45 cm. These taxa, coupled with the absence of *Globorotalia tosaensis* and its LO datum, constrain the sample to Zone N23. Both *Dentoglobigerina altispira* and *Sphaeroidinellopsis seminulina* are last observed in Sample 194-1194A-2H-CC; thus, their LO datums occur between Samples 1H-CC and 2H-CC. Both datums mark the Zone N20/N21 boundary. Sample 194-1194A-1H-CC contains *Globigerinoides extremus, Globorotalia pseudomiocenica,* and *S. dehiscens,* whose datums infer a Zone N19 age. This implies the presence of a condensed Pleistocene to upper Pliocene sequence within the first core. Zone N19 extends to Sample 194-1194A-4H-CC, where the presence of *Globorotalia plesiotumida, S. dehiscens,* and *Globorotalia margaritae,* together with the absence of *Globigerina nepenthes,* confirm this zonal assignment. In addition, the first occurrence (FO) datum of *Globorotalia puncticulata* is observed between Samples 194-1194A-6H-2, 80 cm, and 6H-5, 80 cm. This datum approximates the middle of Zone N19 and thus strengthens the zonal assignment.

Sample 194-1194A-5H-CC contains both *G. margaritae* and *Globorotalia tumida* and lacks *S. dehiscens,* implying a Zone N18 age. Samples 194-1194A-6H-CC through 8H-CC contain *G. nepenthes* and *Neogloboquadrina acostaensis* in addition to the aforementioned taxa and thus can also be assigned to Zone N18. Sample 194-1194A-9H-CC represents the base of Zone N18, as specimens of *G. margaritae* and *Globorotalia cibaoensis* were observed. The presence of *N. acostaensis, G. plesiotumida,* and *Globorotalia lenguaensis* in Sample 194-1194A-10H-CC indicates an age near the top of Subzone N17a. Sample 194-1194A-13H-CC, the last sample from Hole 1194A, was observed to contain *G. extremus* and *G. plesiotumida,* whose FO datums indicate an early Zone N17 age. Cores 194-1194A-14X through 20X were barren of planktonic foraminifer index species and therefore could not be assigned to a zone.

Hole 1194B

Many of the samples from this hole contain reworked planktonic foraminifers, making age assignments difficult. Samples 194-1194B-3R-CC through 8R-CC are devoid of index fossils and are not ascribed to a particular range zone. Sample 194-1194B-9R-CC contains a mixed zonation assemblage of planktonic foraminifers, including *Globigerina druryi* (Zones N15–N7) and *Neogloboquadrina mayeri* (Zones N14–N4). The lack of additional index fossils makes this sample difficult to assign to a specific zone. Samples 194-1194B-10R-CC through 14R-CC are also difficult to assign to a specific zone, as these samples contain rare planktonic foraminifers that do not constitute a viable assemblage for zone assignments.

Globigerinoides trilobus and *Globigerinoides sicanus* are present in Sample 194-1194B-16R-CC, which is tentatively assigned to Zones N8–N9. Samples 194-1194B-17R-CC, 20R-CC, 21R-CC, and 22R-CC contain *G. sicanus, N. mayeri, Globoquadrina dehiscens, Globigerinella obesa,* and *Praeorbulina transitoria,* but the successive samples did not produce a clear age-diagnostic fauna. Sample 194-1194B-27R-CC contains specimens of *Globigerinoides immaturus, G. dehiscens, Globigerinella praesiphonifera,* and *Globigerina ciperoensis* and can be placed in the range of Zone N4b–N5. Samples 194-1194B-31R-CC through 33R-CC lack age-diagnostic taxa.

Benthic Foraminifers

Hole 1194A

The sand-sized fraction of Sample 194-1194A-1H-CC (4.6 mbsf) is overwhelmingly dominated by very small planktonic foraminifers (Table T5). A minor sand- and fine gravel–sized fraction of siliciclastic material is also present. Small bryozoan colonies and bivalves are rare in this fraction. Benthic foraminifers are rare but include conspicuous nodosarids and agglutinated specimens indicating a bathyal depositional environment. The sand-sized fractions of Samples 194-1194A-2H-CC (14.4 mbsf) through 6H-CC (52.6 mbsf) appear bimodal, visually predominated by adult globigerinid planktonic foraminifers but with a substantial component of very small planktonic foraminifers and planktonic debris. The relative proportions of coarser and finer planktonic fractions varies among samples, possibly indicating changes in current winnowing. Benthic foraminifers are generally rare, and the species present indicate bathyal depths of deposition. Gray or blackened grains become increasingly common downward and are significant components of Samples 194-1194A-9H-CC (80.8 mbsf) through 13H-CC (117.4 mbsf). The proportions of very fine sand–sized debris vary from sample to sample; the source appears to be broken planktonic foraminiferal tests. These hemipelagic sediments with some reworked components make up lithologic Unit II (see **"Lithostratigraphy and Sedimentology,"** p. 3).

Samples 194-1194A-14X-CC (119.4 mbsf) through 20X-CC (161.0 mbsf), representing lithologic Unit III (see **"Lithostratigraphy and Sedimentology,"** p. 3), are dominated by small bryozoan colonies, fragments of bryozoan branches, echinoid fragments, benthic foraminifers, and sometimes quartz or glauconite grains (Table T5). In Sample 194-1194A-16X-CC (132.9 mbsf), the prevalence of *Amphistegina hauerina* and *Amphistegina radiata,* both of intermediate robustness, indicate middle neritic water depths of ~30–50 m. In addition, the lack of rounding of the *Amphistegina* specimens, along with *Lepidocyclina* specimens that show minimal breakage and well-preserved surface detail, in-

dicate relatively limited transport. The bryozoan and larger foraminiferal bioclastic sands appear similar to modern sediments described from middle neritic depths on the west Australian shelf by James et al. (1999). In Samples 194-1194A-18X-CC (145.5 mbsf) and 20X-CC, the sediments are finer and more poorly preserved.

Hole 1194B

Samples 194-1194B-2R-CC (119.6 mbsf) through 8R-CC (177.2 mbsf) represent lithologic Unit III (see **"Lithostratigraphy and Sedimentology,"** p. 3) and are similar to those described for this interval in Hole 1194A (Table **T5**). In particular, the distinctive *A. hauerina–A. radiata* foraminiferal assemblage was found in Sample 194-1194B-4R-CC, indicating middle neritic water depths of ~30–50 m. Samples 194-1194B-7R-CC (167.6 mbsf) and 8R-CC (177.2 mbsf) are heavily recrystallized fine sands that may represent transport into outer neritic depths.

Samples 194-1194B-9R-CC (177.6 mbsf) and 10R-CC (191.4 mbsf), at the top of lithologic Unit IV (see **"Lithostratigraphy and Sedimentology,"** p. 3), are characterized by mud and a few ostracode shells. The depositional environment is unknown. Samples 194-1194B-11R-CC (197.9 mbsf) and 15R-CC (238.4 mbsf) are characterized by mud and fine- to medium-sized bioclastic fragments consisting of bryozoan, echinoid fragments, and benthic foraminifers, which are interpreted as representing proximal periplatform deposition at outer neritic water depths. Samples 194-1194B-16R-CC (244.9 mbsf) through 22R-CC (303.9 mbsf) are characterized by fine bioclastic debris that contains both neritic (bryozoan, echinoid, and benthic foraminifers) and pelagic (whole and broken planktonic foraminifers) components. A distal periplatform depositional environment at upper bathyal water depths is tentatively interpreted for this interval (Table **T5**). Sediments are highly recrystallized, and preservation is generally poor throughout this unit.

Samples 194-1194B-30R-CC (388.8 mbsf) through 33R-CC (417.5 mbsf), which occur in lithologic Subunit VB (see **"Lithostratigraphy and Sedimentology,"** p. 3), are dominated by poorly preserved fine bioclastic material with minor quartz and reworked bioclasts that include larger benthic foraminifers. Based on these latter components, a proximal periplatform depositional environment at outer neritic depths is interpreted.

Sample 194-1194B-34R-CC (421.0 mbsf) is a larger benthic foraminifer–dominated grainstone (Table **T5**). White, relatively fresh-appearing specimens, as well as pyrite and glauconite-infilled *Lepidocyclina* and *Miogypsina* and either *Operculina* or *Cycloclypeus* are abundant. Additional thin sections are needed to determine the range of taxa present. A platform depositional environment at middle neritic depths is interpreted based on the presence of these taxa and their relatively flat morphologies. This sample is representative of the base of lithologic Subunit VB (see **"Lithostratigraphy and Sedimentology,"** p. 3).

Interpretation

Microscopic analysis of the sand-sized sediment constituents from Site 1194 reveal that sediments of neritic origin are significant components of lithologic Units III through V (see **"Lithostratigraphy and Sedimentology,"** p. 3). The larger benthic foraminiferal grainstones of lithologic Unit V represent sedimentation in inner to middle neritic depths shortly after flooding of the basement. Sediments of Unit V generally indicate deepening-upward conditions. Although constituents

are relatively poorly preserved, the presence of quartz and larger benthic foraminifers in Subunit VB are indicative of middle to outer neritic paleodepths. The abundance of planktonic foraminifers, coupled with the benthic foraminiferal assemblage, indicates probable upper bathyal depths in a distal periplatform depositional environment for Subunit VA. These depositional conditions continued through the deposition of Subunit IVB, whose neritic component is predominantly in the mud to very fine sand fractions. Medium sand–sized fragments of neritic bryozoan, echinoid, and foraminiferal components are prevalent in most of Subunit IVA, indicating greater proximity to the neritic source of bioclasts and thus a proximal periplatform depositional setting. Subunit IVA also represents a shallowing-upward trend that culminates in middle to inner neritic water depths in Unit III.

Biogenic constituents of nannoplankton and planktonic foraminiferal origin totally dominate lithologic Units I and II. Bathyal benthic foraminifers are a rare but conspicuous component. Differences in sorting and breakage of the planktonic foraminiferal tests among samples within these units are indicative of the influence of an active current regime.

PALEOMAGNETISM

The natural remanent magnetization (NRM) of whole-round sections from Site 1194 was measured at 5-cm intervals using the pass-through cryogenic magnetometer. A 30-mT alternating-field (AF) demagnetization was used. The Tensor tool was deployed to orient the APC cores from Core 194-1194A-4H to 13H. Tests were run to investigate the effects of a superposed laboratory field on the cores by storing the core sections in a mu-metal can prior to measurement. In the one case where the Tensor tool produced an independent test of the magnetization orientation, the 0° declination artifact was not seen in the whole-round measurement of the core section stored in the mu-metal can. When the archive half was measured afterwards, the 0° declination artifact had reappeared. In addition, there was good agreement between the orientation of the whole round and Tensor tool.

Discrete samples were collected from Holes 1194A and 1194B at an average sample rate of two per core. These were used to aid the interpretation of the long-core record of magnetization by providing additional measurements of polarity and basic magnetic characterization. Most of these samples were demagnetized at 5, 10, 15, 20, 40, 60, and 80 mT to permit principal component analysis, but the signal was frequently too weak to permit reliable analysis. For rock magnetic characterization, anhysteretic remanent magnetization (ARM) was measured in 0.2 DC and 200-mT AC fields, and isothermal remanent magnetization (IRM) was measured in a DC field of 1 T. Samples were also progressively magnetized in fields up to 1.0 T to study the acquisition of the IRM.

Results

Long-Core Measurements and Magnetostratigraphy

The long-core measurements for the uppermost 100 mbsf were seriously corrupted by core-top magnetic anomalies (Fig. F25). Unlike at Hole 1192A, where the intensity of magnetization in the uppermost 100 m away from core-top anomalies was ~10^{-3} to 10^{-4} A/m, the intensity was much less at Site 1194. The core top anomalies in the first sec-

F25. Long-core measurements, 0 to 100 mbsf, p. 56.

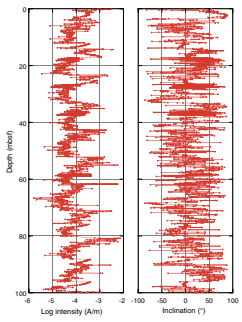

tions of cores at Site 1194 were 10^{-3} to 10^{-4} A/m. In most APC cores, the intensity decreased systematically through Cores 194-1194A-2H and 3H, so that in Cores 194-1194A-4H and 5H, it reached 10^{-5} A/m. These core-top anomalies were often accompanied by magnetic susceptibility peaks, indicating that new magnetic material had been introduced at the tops of cores and then magnetized in the direction of the downhole overprint. Thus, the true intensity of the uncontaminated sediments is ~10^{-5} A/m, and the contamination reaches 10^{-3} A/m. Iron oxide (rust) within the pipe string is a well-known contamination problem, and a small number of such particles would swamp the signal from the carbonates. The magnetization is acquired in the same field that gives the downward-directed drilling overprint, which likely comes from the drill bit in the bottom-hole assembly.

In the presence of this contamination, magnetostratigraphy becomes problematic at the very top of the borehole instead of from ~100 mbsf, as it did at Site 1192. However, low-pass filtering removes these high-intensity values associated with core tops (using an arbitrary cut-off intensity of 10^{-4} A/m) (Fig. F26). The inclinations are adjusted using the intensity cut off by simply deleting the inclinations associated with the high-intensity amplitudes (Fig. F26). Furthermore, it is clear that from ~50 to 110 mbsf, a sequence of inclination changes gives an indication of the polarity. The inclination is not symmetrical about the zero baseline because of the positive overprint. Between ~85 and 95 mbsf, there is a prominent reverse-magnetized interval. Assuming that the biostratigraphy is correct, this interval can be assigned to Chron C3Ar (see "Biostratigraphy and Paleoenvironments," p. 9).

When overprint is a problem, it is sometimes useful to compare the z-component intensity with inclination. A simple filtering approach is to balance the positive and negative z intensities by biasing the zero line (Fig. F26). Doing this confirms the earlier suggestion of a negative interval between ~85 and 95 mbsf, which is assigned to Chron C3Ar. Beneath is an interval of 15 m, which shows a normal-reversed-normal sequence in less strongly magnetized material. This could then represent the Chron sequence C3Bn-C3Br1r-C3Br1n. Higher in the section, above the hiatus, the magnetostratigraphy is less clear. The age assignment of the reversal sequence is not an independent determination from the paleomagnetic record; however, it is dependent upon the biostratigraphic age constraints. Between 100 and 300 mbsf, recovery was insufficient to produce a useful magnetic record, but between 330 and 370 mbsf, recovery improved and reversals could be recognized so that a sequence could be constructed (Fig. F27). However, no useful magnetostratigraphy is possible with such a short sequence.

Overall, the record from the long cores does not allow a clear magnetostratigraphic interpretation. In the upper part of the section, where we had good recovery, the magnetization of the sediments was weak, so that core-top anomalies obscured the record. Downcore, poor recovery precluded useful magnetostratigraphy.

F26. Long-core measurements, 0 to 100 mbsf, p. 57.

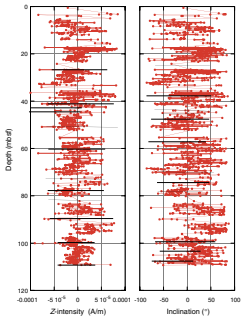

F27. Long-core measurements, 300 to 400 mbsf, p. 58.

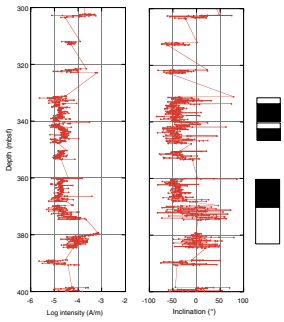

Discrete Samples

Discrete samples were used to try to improve the NRM determinations and to attempt to correlate rock magnetic properties to the lithologies observed in the cores, so that magnetic proxies could be used to interpret environmental changes.

The NRM of most of the Site 1194 sediments was too weak for useful shipboard analysis, but could be successfully measurable onshore with

magnetometers designed to measure discrete samples. Only two samples gave convincing evidence of the isolation of a single direction of magnetization that appeared to be converging to the origin of the Zijderfeld diagram (Fig. **F28**). Sample 194-1194B-34R-2, 45–47 cm, from near the basement, is strongly magnetized. It has a soft component with a declination of 215°, an inclination of –18°, and a maximum angular deviation angle of 1.7°. The apparent characteristic remanent magnetization is shallowly inclined down to the east-northeast (declination = 67°, inclination = 14°, and maximum angular deviation = 4.9°). The basement Sample 194-1194B-34R-5, 12–14 cm, is strongly magnetized with a steep downward direction of magnetization (declination = 242°, inclination = –61°, maximum angular deviation = 2.4°). Further analysis onshore should better determine these directions and may permit useful comparison with the Australian apparent polar wander path to date the magnetization and associated alteration events.

Figure **F29** is a remanent magnetization characterization plot. The IRM acquisition shows almost complete saturation by 100 mT, which is a strong indication of the dominance of magnetite in the sample. The intersection of the IRM demagnetization and acquisition curves shows weak negative interactions. The stability of IRM against AF demagnetization can be measured by the ratio of IRM after demagnetization to 30 mT to saturation IRM. Values between 60% and 40% for magnetite are suggestive of bacterial magnetite, as is the high value of the ratio of normalized ARM to IRM.

Environmental magnetists (e.g., Maher and Thompson, 1999) have developed a method to identify magnetic phases based on simple measurements similar to those made aboard the *JOIDES Resolution*. Magnetic stability measured by the fraction of IRM remaining after demagnetization to 40 mT is plotted vs. the ratio of ARM susceptibility to IRM. Such a plot calculated for Sample 194-1194B-4R-1, 22–24 cm (Fig. **F29**), shows that the values fall in the field of disaggregated chains of magnetite (fine detrital magnetite field). Downhole variations in NRM, ARM, and IRM show that at Site 1194 most magnetic material occurs in the basement and immediately above it (Fig. **F30**). The ratio of IRM acquisition at 100 mT to 1T, which is near 1 with the exception of the hardground that is near 110 mbsf, indicates that magnetite dominates the magnetic mineralogy. In the region of the hardground there is evidence for a much higher coercivity phase, possibly hematite, which would be in concert with the red staining of the samples.

AGE MODEL

The age model for the 427-m-thick early Miocene to Pleistocene sequence cored at Site 1194 is biostratigraphically defined by nine calcareous nannofossil datums and five planktonic foraminifer datums (Table **T6**; Fig. **F31**) (see **"Biostratigraphy and Paleoenvironments,"** p. 9). Strong core-top intensity anomalies corrupted the magnetic inclination record in the upper part of the section. In the lower part of the section, low core recovery prevents construction of a polarity sequence (see **"Paleomagnetism,"** p. 13). Therefore, a magnetostratigraphy cannot be established at this site, and the biostratigraphic control points are used to construct the shipboard age model for Site 1194 (Fig. **F31**).

The low-resolution biostratigraphy in the early to middle Miocene Megasequence C (lithologic Units III to V) can be represented by one straight age-depth segment with an average sedimentation rate of 31

F28. Analysis of NRM by AF demagnetization, p. 59.

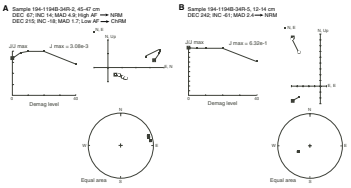

F29. Remanent magnetism characteristics, p. 60.

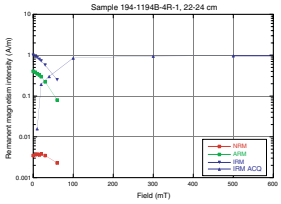

F30. Variation of remanent magnetism characteristics downhole, p. 61.

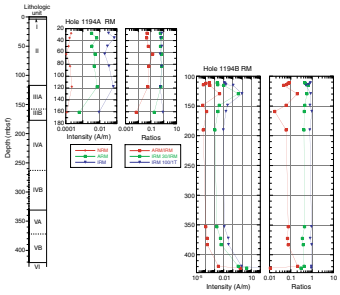

T6. Age-depth control points, p. 97.

F31. Age-depth model and sedimentation rates, p. 62.

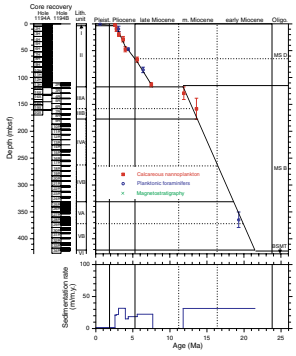

m/m.y. (Fig. F31). A hardground that caps lithologic Unit III at 117 mbsf contains a late middle to late Miocene hiatus, which lasted from ~11.8 to ~7.7 Ma. The late Miocene to Pliocene (8-2.6 Ma) is represented by lithologic Unit II, which is correlative with Megasequence D, a hemipelagic section with frequent gravity flow deposits. A significant hiatus or condensed section is indicated at the lithologic Unit I/II boundary (3.8 mbsf) and may have lasted as long as 2.5 to ~0.8 Ma.

Age picks for lithologic and seismic unit boundaries are summarized in Table T7.

T7. Age picks, p. 98.

GEOCHEMISTRY

Volatile Hydrocarbons

Concentrations of volatile hydrocarbon gases were measured from every core using the standard ODP headspace sampling technique and gas chromatographic analysis. Methane only occurred in very minor concentrations (1 to ~2.5 ppmv) (Table T8).

The low gas content at Site 1194 is likely a function of two characteristics of the sediment: appreciable pore water SO_4^{2-} concentrations are likely to be limiting methanogenesis, and the organic matter that does exist is immature relative to hydrocarbon expulsion and petroleum generation.

T8. Headspace gas composition, p. 99.

Interstitial Water Chemistry

Pore water samples in Hole 1194A were taken approximately every 10 m down to 132.6 mbsf. Sampling continued more intermittently to a depth of 418.0 mbsf in Hole 1194B, where cemented carbonate intervals and reduced recovery limited collection of pore waters (Fig. F32; Table T9). In some samples from Hole 1194B, it was not possible to collect sufficient water from the sediments to complete all analyses.

Pore water chloride increases from a value of 558 mM at 2.9 mbsf to 567 mM at 20.1 mbsf (Fig. F32A). From this depth to 300 mbsf, chloride concentration ranges narrowly, between 565 and 563 mM. Values are somewhat more variable through the remainder of the cored interval.

Alkalinity shows a slight increase, from 2 to 2.9 mM, in the upper 30 mbsf, then decreases in a linear fashion to ~0.68 mM at a depth of 254.9 mbsf and remains at that level to the bottom of the hole (Fig. F32B). The low alkalinity is unusual when considered together with significant bacterial sulfate reduction (discussed below). The 8 mol of sulfate reduction that occur in the upper 130 mbsf should add 16 mol of alkalinity to the pore fluids. This "missing" alkalinity is most likely precipitated as a carbonate mineral.

Sulfate concentration decreases steadily through the upper 120 mbsf, from 28.85 mM in the shallowest sample to ~18 mM within lithologic Unit IV (Fig. F32C) and remains relatively constant at 18 mM to the bottom of the cored section. The decrease in sulfate is likely due to bacterial sulfate reduction, with the modest removal of sulfate attributable to the low organic carbon content of the sediments (see "Sedimentary Geochemistry," p. 18).

Associated with the reoxidation of sedimentary organic matter via sulfate reduction is the release of ammonium to the pore waters. Thus, the ammonium profile mirrors the sulfate profile (Fig. F32C, F32D). Ammonium concentration increases steadily over the upper 130 m of

F32. Dissolved constituents vs. depth, p. 63.

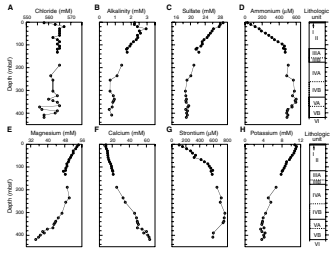

T9. Interstitial water chemistry, p. 100.

the sediments, reaching 600 µM near 340 mbsf, the depth where sulfate reduction ceases.

In lithologic Units I and II, the magnesium concentration decreases almost linearly from 54.5 mM at the surface to 48.26 mM at 132.6 mbsf (Fig. F32E). Below that depth, magnesium concentration remains relatively constant to ~300 mbsf then decreases to 34 mM at the base of Hole 1194B. The pore water calcium concentration increases in the uppermost 130 mbsf from 12.5 to 21.1 mM (Fig. F32F). Below 189 mbsf, the calcium concentration increases more rapidly with depth, reaching ~64 mM at 419 mbsf, the base of Hole 1194B.

In Hole 1194A, the concomitant decrease in pore water magnesium and increase in calcium concentration could be taken as evidence of minor dolomite formation by the reaction

$$Mg^{2+} + 2CaCO_3 \leftrightarrow CaMg(CO_3)_2 + Ca^{2+}.$$

Although the concentrations are linearly correlated (Fig. F33), the slope of the relationship is not as would be expected from this reaction. As at Site 1192, magnesium and sulfate are highly correlated with a slope close to one (Fig. F34), suggesting dolomite formation via the reaction

$$Mg^{2+} + HCO_3^- + CaCO_3 \leftrightarrow CaMg(CO_3)_2 + H^+,$$

with the necessary 2 mol of alkalinity supplied by bacterial sulfate reduction. Pore water alkalinity values support dolomite formation by this second reaction, which also explains the missing alkalinity sink.

The changes in pore water calcium and magnesium seen below 180 mbsf (Fig. F32E, F32F) in the more lithified lithologic Units IV and V are not likely to be the result of dolomite formation, as the concentration of the two ions does not show a 1:1 correlation (Fig. F33). It is more likely that the observed profiles result from alteration of mafic basement rocks and subsequent diffusive exchange with the pore fluids in the overlying sediments. Some combination of diffusion and further minor dolomitization of the sediments, however, cannot be ruled out.

Pore water strontium concentration increases nearly linearly through lithologic Units I and II, rising from 105 µM at 2.9 mbsf to ~580 µM at 132 mbsf (Fig. F32G). Calcite recrystallization in this interval releases strontium to the pore water. The lack of further increase with depth suggests either no further carbonate recrystallization or that the strontium concentration is limited by celestite solubility. The relatively high sulfate concentration would titrate strontium from the pore waters as it is released by recrystallization. Significant carbonate recrystallization, however, should eventually led to a pattern of decreasing sulfate concentration and increasing strontium concentration, which is not observed. Potassium concentration decreases nearly linearly from 11.13 mM at 10.6 mbsf to values near 3.5 mM at 360 mbsf after a slight increase in the uppermost 10 m of the hole (Fig. F32H). Below 360 mbsf, concentrations remain relatively constant.

X-Ray Diffraction Carbonate Mineralogy

Ninety-one sediment samples were analyzed for carbonate mineralogy from Site 1194. Data are presented in Figure F35 and Table T10. The hemipelagic sediments of lithologic Units I and II are composed almost entirely of calcite, with a few samples containing 2–3 wt% dolomite.

F33. Dissolved pore water magnesium vs. calcium, p. 64.

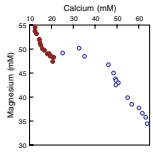

F34. Dissolved pore water magnesium vs. sulfate, p. 65.

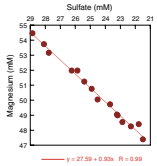

F35. Dolomite, calcite, and noncarbonate mineral percentages, p. 66.

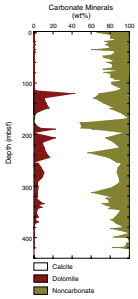

T10. Calcite, dolomite, and noncarbonate mineral percentages, p. 101.

Aragonite was not detected. The hardground at the transition to lithologic Unit III contains ~50 wt% dolomite. Lithologic Subunit IIIA averages ~20 wt% dolomite, whereas Subunit IIIB is nearly pure calcite. In lithologic Units IV and V, dolomite is consistently ~10 wt% except near the base of Unit V where the sediments are pure calcite.

Sedimentary Geochemistry

Results

Calcium carbonate ($CaCO_3$) content at Site 1194 ranges from ~45 to 99 wt% (Fig. **F36;** Table **T11**). The total organic carbon (TOC) content of all samples measured at Site 1194 is <0.5 wt%, with the highest values existing in the uppermost 100 m of the sediment section. Note that TOC content from Rock-Eval pyrolysis and carbon-nitrogen-sulfur analyses provide similar decreasing downsection profiles (Fig. **F36;** Tables **T11, T12**) and that TOC values covary inversely with $CaCO_3$ content (Fig. **F36**).

Hydrogen index (HI) values at Site 1194 range from 29 to 300 mg HC/g TOC (Fig. **F36;** Table **T12**). Oxygen index (OI) values vary from 0 to 45,400 mg CO_2/g TOC (Table **T12**). The high OI values measured are attributed to the thermal degradation of calcium carbonate during pyrolysis and are not considered in this interpretation. The low TOC values in some intervals at Site 1194 limit the reliability of some HI values. We performed duplicate and triplicate analyses on these samples, which indicated a reproducibility of ±10%. T_{max} values ranging from 368° to 422°C (Table **T12**), although the most reliable T_{max} values cluster between 400° and 420°C. Total S content in Site 1194 sediments range from 0 to ~0.67 wt% (Fig. **F36;** Table **T11**).

Discussion

Variations in the generally high calcium carbonate content (average = ~82 wt%) (Fig. **F36**) of sediments at Site 1194 mostly reflect fluctuations in the ratio of biogenic carbonate and terrigenous sedimentation to the seafloor through time. Calcium carbonate content exhibits an overall increase from 89 wt% at 2.2 mbsf to 95 wt% at 118 mbsf. This interval corresponds to lithologic Unit II (see **"Lithostratigraphy and Sedimentology,"** p. 3) and contains well-preserved foraminifers, and lesser amounts of calcareous nannofossils (see **"Biostratigraphy and Paleoenvironments,"** p. 9). The noncarbonate sediment in this interval is primarily clay, with between ~0.2 and 0.5 wt% TOC. Firmgrounds clustered between ~34 and 42 mbsf (see **"Lithostratigraphy and Sedimentology,"** p. 3) appear to correspond to a slight decrease in calcium carbonate content (~59 and ~70 wt%, respectively) and elevated percent TOC values (0.48 and 0.42 wt%, respectively) obtained from Rock-Eval pyrolysis. The relatively elevated TOC content with mostly low HI values and several extremely high C/N ratios likely indicate the presence of terrigenous organic matter. The very high C/N values may represent the presence of inertinite within the terrigenous debris. These interpretations are at least partially corroborated by observations of wood fragments at ~10–15 and ~110–115 mbsf (see **"Lithostratigraphy and Sedimentology,"** p. 3) and fusain in a number of the samples described in this section. The relatively high total S content in this interval (Fig. **F36**) and observations of pyrite (see **"Lithostratigraphy and Sedimen-**

F36. Carbon, HI, and sulfur results, p. 67.

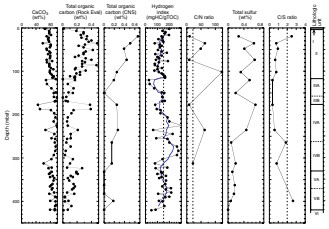

T11. Carbon, nitrogen, sulfur, and hydrogen values, p. 102.

T12. Rock-Eval pyrolysis results, p. 104.

tology," p. 3) suggest that pyrite formation was influenced by increased organic matter influx to the seafloor.

Sediments from ~118 to 300 mbsf can be organized into three geochemically defined units. Each unit consists of a conspicuous horizon of increased percent TOC values, low HI values, and relatively elevated percent total S content, overlying a broader interval of relatively high $CaCO_3$, low TOC, and higher HI values. The uppermost horizon appears to coincide with a firmground, and the uppermost unit, ranging from ~117 to 170 mbsf, corresponds to lithologic Unit III (see "Lithostratigraphy and Sedimentology," p. 3). A slight decrease in carbonate content between ~150 and 160 mbsf corresponds to the Subunit IIIA/IIIB boundary, an inferred hardground (see "Lithostratigraphy and Sedimentology," p. 3) and a prominent seismic reflection (see "Seismic Stratigraphy," p. 27).

The most prominent geochemical horizon exists between ~177 and 187 mbsf at Site 1194, marked by the lowest $CaCO_3$ content (45%) observed at the site, and appears to coincide with a second inferred firmground and the boundary between lithologic Units III and IV (see "Lithostratigraphy and Sedimentology," p. 3). It overlies a unit of relatively elevated carbonate and depressed TOC content from ~190 to 225 mbsf. The third prominent horizon at ~235 mbsf appears to correspond to a firmground (see "Site 1194 Visual Core Descriptions," p. 1) and again overlies an interval of elevated carbonate and HI values and depressed TOC content to a depth of ~295 mbsf. This horizon corresponds to a peak in the natural gamma ray log (see "Downhole Measurements," p. 22) and is interpreted as part of the deepest depositional environment recorded at Site 1194 (see "Biostratigraphy and Paleoenvironments," p. 9).

Calcium carbonate content decreases to ~61 wt% in the interval ~295–313 mbsf and then displays an overall increase to ~92 wt% toward the bottom of the hole. Through this same interval, TOC values increase to ~0.3 wt% at ~324 mbsf and then decrease to <0.1 wt% at total depth; sulfur values are depressed relative to samples higher in the section. This interval roughly corresponds to the lower portion of lithologic Unit IV (see "Lithostratigraphy and Sedimentology," p. 3). Below the percent TOC peak at ~324 mbsf, carbonate and TOC values covary inversely; this interval roughly corresponds to lithologic Subunits VA and VB (see "Lithostratigraphy and Sedimentology," p. 3).

CORE PHYSICAL PROPERTIES

Physical properties were measured and evaluated on whole cores, split cores, and core samples from Site 1194. The multisensor track (MST) was used on whole cores to perform nondestructive measurements of bulk density, magnetic susceptibility, and natural gamma radiation (NGR). Compressional wave velocities were measured in the x-, y-, and z-directions on split cores and core samples. Moisture and density (MAD) analyses were performed on core samples. Thermal conductivity was evaluated on unlithified whole cores and on samples from semilithified and lithified cores.

Density and Porosity

Two methods were used to evaluate the bulk density at Site 1194. Gamma ray attenuation (GRA) provided an estimate of bulk density

from whole cores. MAD samples facilitated a second, independent measure of bulk density while providing grain density and porosity data. From 0 to 117 mbsf (lithologic Units I and II), MAD values cored with the APC are approximately 0.1 g/cm³ lower than GRA bulk density (Fig. F37). Below 117 mbsf (lithologic Units III–VI), MAD bulk density correlates with maximum GRA values. The low GRA bulk density below 117 mbsf is likely a result of undersized cores and/or sample disturbance as a result of XCB and RCB coring (see "Core Physical Properties," p. 21, in the "Explanatory Notes" chapter).

Bulk density values show an overall increase downhole with small-scale variability superimposed (Fig. F37). Bulk density is 1.5 g/cm³ at the seafloor and increases to a maximum of 2.3 g/cm³ at 421 mbsf. The highest bulk density values (2.6–2.7 g/cm³) are associated with a hardground (117 mbsf; top of lithologic Unit III) and with the acoustic basement (lithologic Unit VI; see "Lithostratigraphy and Sedimentology," p. 3).

Grain density has an average value of 2.7 g/cm³ and has considerable scatter from 2.3 to 3.3 g/cm³ (Fig. F37). Values less than 2.5 g/cm³ or greater than 3.0 g/cm³ are rare and may be the result of grain volume measurement error.

Porosity, calculated from MAD data (see "Core Physical Properties," p. 21, in the "Explanatory Notes" chapter), decreases from 73% at 2 mbsf to less than 40% below 350 mbsf (Fig. F37). The lowest porosity (6%–8%) occurs in the hardground between lithologic Units II and III (117 mbsf) and in lithologic Unit VI (acoustic basement; see "Lithostratigraphy and Sedimentology," p. 3).

Porosity (ϕ) can be related to depth (z) using an exponential function and a porosity decay parameter with depth (k; e.g., Athy, 1930),

$$\phi(z) = \phi_o e^{-kz}.$$

A least-squares fit of this function yields ϕ_o = 65% and k = 0.002 m^{-1} (correlation coefficient = 0.91; Fig. F37). This normal compaction trend suggests hydrostatic fluid pressures that are likely the result of moderate to low sedimentation rates and moderate permeability allowing drainage and compaction during deposition and burial. This trend also implies that erosion events have not been significant at this site, as erosion often appears as a step decrease in porosity.

F37. Bulk density, grain density, and porosity, p. 68.

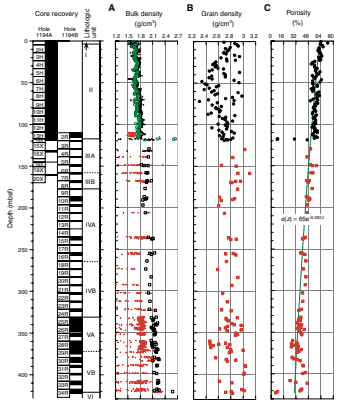

Compressional Wave Velocity

Compressional wave velocity was measured at discrete intervals for Site 1194. The raw data show an abrupt velocity shift at 50 mbsf (Fig. F38). This step increase in x-directed velocity probably represents measurement errors with the PWS3 sensor. To correct this velocity shift, all PWS3 data below 50 mbsf were decreased by 100 m/s (Fig. F38). The 100 m/s shift is the average discrepancy between y-, z- and x-directed velocity from 50 to 60 mbsf and assumes isotropic velocity because the overall velocity structure at Site 1194 is isotropic (Fig. F38; see "Core Physical Properties," p. 21, in the "Explanatory Notes" chapter).

Velocity generally increases from 1550 to 1600 m/s above 117 mbsf to 2800 m/s below 400 mbsf (Fig. F38). At a finer scale, abrupt increases in velocity are related to prominent lithologic boundaries. Velocity increases at 117, 160, 255, and 421 mbsf correspond to well-lithified boundaries with low porosity (e.g. hardground, firmground, and acous-

F38. Compressional wave velocity and adjusted velocity, p. 69.

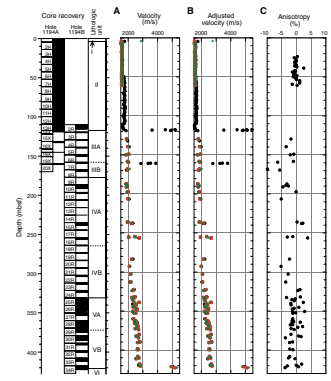

tic basement; see "Lithostratigraphy and Sedimentology," p. 3, and "Downhole Measurements," p. 22). The increase in velocity at 117 mbsf correlates with the top of lithologic Unit III (see "Lithostratigraphy and Sedimentology," p. 3), the presence of dolomite (see "Geochemistry," p. 16), and an increase in wireline log velocity values (see "Downhole Measurements," p. 22).

Velocity data often correlate with porosity. However, the porosity and velocity data from Site 1194 do not match the time-average relationship of Wyllie et al. (1956) (Fig. F39) (see "Core Physical Properties," p. 24, in the "Site 1193" chapter) but can be described with a power law relation,

$$V_P(\phi) = a\phi^{-b},$$

where V_P is the compressional wave velocity, and a (23,325 m/s) and b (0.65) are empirical constants determined from a least-squares regression (correlation coefficient = 0.92; Fig. F39). This power law correlation supports the porosity trend of consistent compaction and interpretation that if there has been any erosion, it has been minimal. Deviations from the velocity-porosity model in lithologic Units I–V may be indicative of hiatuses or exposures that have resulted in diagenesis, significant porosity loss, and velocity modification. High velocities (~5000 m/s) within lithologic Unit VI are controlled by lithology (acoustic basement) and do not represent diagenesis.

Temperature and Thermal Conductivity

The advanced piston corer temperature tool (APCT) was used to measure seafloor and downhole temperature. Four downhole temperature attempts were made, and three were successful (Cores 194-1194A-7H, 10H, and 13H; Fig. F40). The resulting temperature profile increases linearly with depth at an average gradient of 45°C/km (Fig. F41).

Thermal conductivity increases gradually with depth at Site 1194 (Fig. F41). The first three measurements (4, 8, and 18 mbsf) deviate significantly from this trend and are considered suspect because they are significantly elevated for unlithified, shallow sediments with high moisture content. From 27 to 420 mbsf, thermal conductivity increases from 1.1 to 1.9 W/(m·K). The scatter of thermal conductivity values below 117 mbsf may have resulted from variations in contact between samples and the half-space probe. Data above 117 mbsf were acquired with the full-space needle probe.

Thermal conductivity (K_{bulk}) can be described with a power law relationship (e.g., Keen and Beaumont, 1990)

$$K_{bulk}(\phi) = K_w\phi K_{grain}^{(1-\phi)},$$

where K_w is the thermal conductivity of the interstitial water, and K_{grain} is the thermal conductivity of the solid grain (see "Core Physical Properties," p. 21, in the "Explanatory Notes" chapter). The observed thermal conductivity follows this relationship within the range for the encountered sediments (Fig. F42). Together, the thermal conductivity and average thermal gradient provide a heat flow value of 49.5 mW/m².

F39. Velocity-porosity crossplot, p. 70.

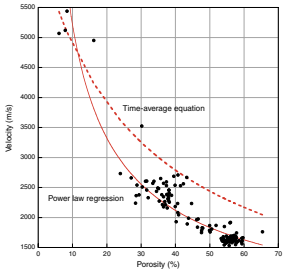

F40. APCT observations and temperature decay models, p. 71.

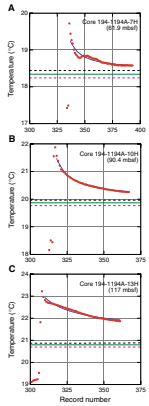

F41. Thermal conductivity and downhole temperature, p. 72.

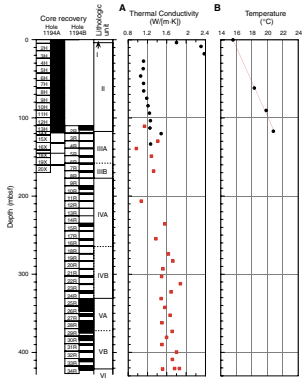

F42. Thermal conductivity as a function of porosity, p. 73.

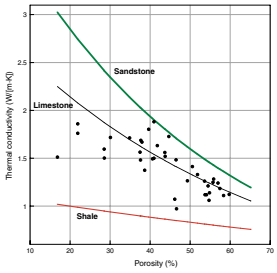

Magnetic Susceptibility, Natural Gamma Radiation, and Color Reflectance

Magnetic susceptibility (MS) has an average of 2.5 × 10^{-6} SI with 10- to 25-m scale variations superimposed (Figs. F43, F44). These variations are most apparent in lithologic Units I and II, where core recovery was nearly complete. NGR has similar trends to MS, including 10- to 25-m scale variations within lithologic Units I and II (Figs. F43, F44). Apparent cyclic variations are also observed in the downhole logs (see "Downhole Measurements," p. 22). Coincident increases in MS and NGR, a lack of glauconite, and the presence of gravity flow deposits (see "Lithostratigraphy and Sedimentology," p. 3) suggest that these variations may represent fining upward sediment packages and/or increased terrigenous clay content. The local NGR high at 117 mbsf correlates with a phosphatic hardground (see "Lithostratigraphy and Sedimentology," p. 3). Above 5 mbsf, sediment color (lightness), a common proxy for clay content, also shows a high. Below 5 mbsf, lightness variations do not correspond with MS and NGR in lithologic Units I and II (Fig. F44).

Below lithologic Unit II, poor recovery prevents detailed interpretation of MS and NGR trends. Local maxima, however, are identified at 233–238 mbsf and 252–258 mbsf. Within lithologic Unit V, small-scale (~10 m) variations are present in the MS and NGR data, but are not as well-defined as within lithologic Unit II. They may represent input variability of terrigenous clay. The olivine basalt basement (lithologic Unit VI; see "Lithostratigraphy and Sedimentology," p. 3) is characterized by a dramatic MS increase. This increase is not paralleled in the NGR.

F43. MS and NGR, p. 74.

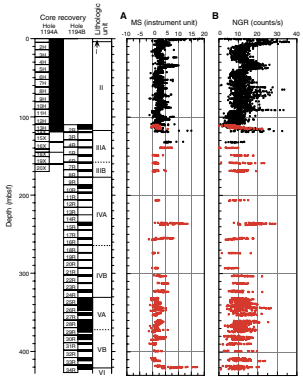

F44. Smoothed MS, NGR, and lightness, p. 75.

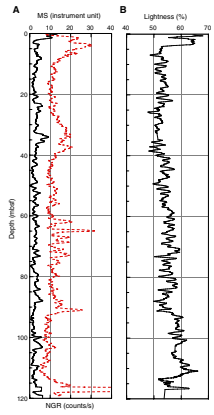

T13. Summary of logging operations, p. 105.

DOWNHOLE MEASUREMENTS

Logging Operations

Logging operations at Hole 1194B, which was drilled to a total depth (TD) of 427.1 mbsf, began at 0530 hr on 25 January 2001 with the deployment of the triple combination (triple combo) tool (natural gamma ray, density, porosity, and resistivity tool) that also carried the LDEO temperature tool on the bottom and the LDEO multisensor gamma ray tool (MGT) on the top (Table T13). In the first pass, data were collected with the triple combo and the temperature tool. For the second pass, power was switched to the downhole measurement lab to collect data with the MGT, which uses the same communication lines as the triple combo. To reach optimal resolution, the MGT requires a slower logging speed (700 ft/hr; 210 m/hr) (Table T13).

In the narrow but open hole, the tools reached a depth at 425 mbsf, which is only 2.1 m above the drilled TD of 427.1 mbsf. The seafloor was detected from the log signals at 385.5 mbrf. For the second run, the FMS and DSI combination was rigged up. Malfunctioning of the DSI tool was discovered while lowering the tool into the hole; later, this proved to be related to a hardware problem. Nevertheless, a first pass with the FMS was completed. For the third run, the DSI was replaced by the LSS tool. During the run, the borehole started to deteriorate, forming a tight spot at around 230 mbsf that was passed after several attempts. The last run was the check shot survey with the WST, using an 80-in^3 water gun, as the air gun was leaking. The WST tool could not pass a tight spot at ~158 mbsf; thus, only three stations were measured

at shallow depths of 143.2, 117.2, and 88.2 mbsf. The water gun signal was not clean because a low-frequency precursor interfered with the main peak. As a result, the first arrival of the *P*-wave signal/response could not be picked accurately. Logging operations ended at ~0030 hr on 26 January.

Log Quality

All logging data from the first run are of good quality. In the intervals between 197–211 mbsf and 260.5–272 mbsf, the caliper opened to its maximum of 17 in, indicating that the hole diameter was >17 in (43 cm). In these intervals, the eccentered tool string had no contact with the borehole wall, negatively affecting mainly the density and porosity measurements (Fig. F45). The FMS data from the second run were of excellent quality throughout the entire open-hole interval, with the exception of the above mentioned intervals of large hole diameter. Little evidence of sticking was detected in the data. In the third run, no FMS data could be recorded between 255.5 and 239.7 mbsf because the caliper arms had to be closed as a result of high tension from the small borehole diameter (<5 in). Because of good initial hole conditions, the FMS images show that after preliminary shipboard processing, most downhole changes are sensitive to resistivity, such as the degree of bioturbation, grain size, bedding character, and cementation. The velocity measurements from the third run are generally good, but some erroneous data were recorded when the FMS arms had problems passing narrow intervals and the tool string shifted in the hole.

The MGT and the Schlumberger hostile environment spectral gamma ray sonde (HNGS) were both run in Hole 1194B; overall, both data sets are of high quality and correlate well (Fig. F46). A slight offset of 4 gAPI of the MGT gamma ray can be observed that is due to the borehole size correction applied to HNGS data but not to MGT data. This comparison demonstrates the higher vertical resolution of the MGT vs. the HNGS, which according to the tool specification is ~10 cm vs. 45 cm (see "Downhole Measurements," p. 30, in the "Explanatory Notes" chapter). The comparison of the MGT total counts with the core-derived natural gamma ray MST total counts shows that these two data curves also correlate well and that the measurements have approximately the same vertical resolution (Fig. F47). The comparison, however, is hampered by the bad recovery.

Comparison of Core and Log Data

Compressional wave velocity, density, and natural gamma ray data obtained by borehole logging show good agreement with those data obtained from core samples, with the exception of the GRA bulk density, which was not corrected for core diameter (Fig. F48). Bulk density from MAD data are slightly higher than the log data. *P*-wave sensor (PWS) and log velocity data both record the downhole increase of velocity, but the discrete samples show higher values in thin beds (e.g., hardgrounds at 114.5 and 159.5 mbsf). In the lower part of the hole, PWS velocity values are generally lower than the log data. This shift is probably caused by the lack of overburden pressure in the core samples. Although the natural gamma ray pattern of the MGT log matches well with the HSGR (standard gamma ray) data taken on cores, absolute values of these two tools (MGT and MST) should not be compared because they are specific for each sensor (Fig. F47).

F45. Composite log for Hole 1194B, p. 76.

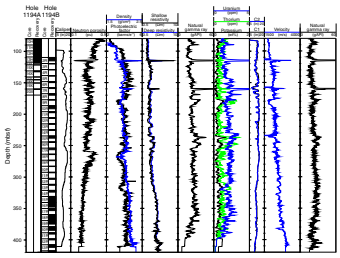

F46. Data produced by the HSGR tool and the MGT, p. 77.

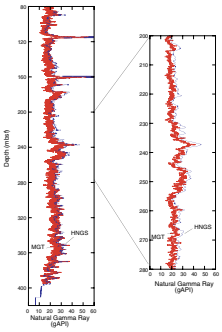

F47. Correlation between the gamma ray values measured downhole and the natural gamma ray values of the MST, p. 78.

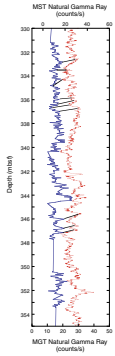

F48. Comparison of core and log physical properties, p. 79.

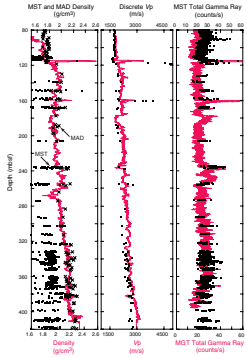

In general, core physical property data show a higher degree of variation with higher amplitudes. Reasons for these discrepancies include (1) a difference in resolution, centimeter scale on core vs. decimeter scale in logs; (2) variability in core physical properties due to sample disturbance and core diameter variations (see "Core Physical Properties," p. 19); and (3) laboratory vs. in situ conditions. Data from logs and core samples, however, provide similar physical values for the subsurface strata, despite certain limitations of both methods. This good correlation gives confidence for supplementing one data set with the other as it is done when calculating synthetic seismograms (e.g., at Site 1193) (see "Seismic Stratigraphy," p. 27, in the "Site 1193" chapter).

Results

Downhole measurements from Hole 1194B retrieved a continuous geophysical record from sediments at 84 mbsf to basement at 425 mbsf (Fig. F45). The dominant lithologies are carbonates with small admixtures of siliciclastics that show overall low NGR (see "Lithostratigraphy and Sedimentology," p. 3). Density and velocity display a general increasing downhole trend, whereas porosity values decrease as a result of compaction. However, large excursions and inversions interrupt these trends. These deviations are typical in carbonates in which early diagenesis can preserve high porosity intervals; alternatively, marine burial diagenesis can generate secondary porosity (Longman, 1981; Anselmetti and Eberli, 1993; Melim et al., 1995).

Three intervals (logging Units I–III) with characteristic log signature are observed within the logged section (Fig. F49). In addition, five horizons within these units also mar prominent changes in the log signature. These changes correlate well with the boundaries of the lithologic units, indicating that facies changes across unit boundaries produce a distinct petrophysical signal. The logs also provide information about the location of hardgrounds and facies that were not recovered. In particular, the FMS images help reconstruct a more complete succession of facies types calibrated with the incompletely recovered drilled section, as it is possible to distinguish highly bioturbated beds rich in skeletal material, bedding planes, and cemented zones. In addition, grain size differences are apparent in the coarser sediments. In the following, the character of the intervals and changes in log signature are described and correlated to the described lithology. All depths are from the log data, which differ from the curated depths used for the core.

F49. Comparison of lithologic units, log units, and position of changing log signatures, p. 80.

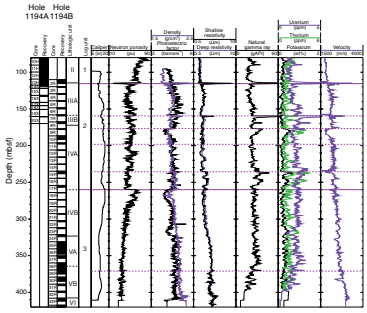

Logging Unit 1 (84–114.5 mbsf)

Logging Unit I is characterized by low values in density, velocity, resistivity, and natural gamma ray values, with corresponding high porosity values (Fig. F49). This log unit corresponds to the basal 30 m of lithologic Unit II and seismic Megasequence D. The sediments consist of unlithified mudstones/wackestones (see "Lithostratigraphy and Sedimentology," p. 3, and "Seismic Stratigraphy," p. 27).

Logging Unit 2 (114.5–260 mbsf)

Logging Unit 2 is characterized by sharp and large variations in all logs and has four internal log signature changes (Fig. F49). The most dramatic of these variations marks the upper unit boundary, where all logs show a distinct peak. For example, velocity increases from 1.7 to

3.7 km/s, and density changes from 1.8 to 2.55 g/cm³. HSGR, mostly derived from uranium, increases from 15 to over 60 gAPI. This thin peak corresponds to a 1-m-thick, tightly cemented hardground bed with a reddish brown crust marking the top of lithologic Subunit IIIA and the upper boundary of seismic Megasequence B (Figs. F49, F50A) (see "Lithostratigraphy and Sedimentology," p. 3, and "Seismic Stratigraphy," p. 27). At 159.5 mbsf, a similar peak in the logs occurs, indicating the presence of a second hardground bed that was not fully recovered in the core (Fig. F49). Pieces of limestone in Core 194-1194B-7R (~160 mbsf) that have high velocities of up to 4 km/s are probably from this hardground bed (Fig. F48). In the FMS images, both beds show high resistivity with a mottled structure that is indicative of intense cementation and partial dolomitization (Fig. F50). The second inferred hardground bed, however, is less resistive and seems to be slightly thicker, extending from 159.5 to 161.2 mbsf (Fig. F50B).

At 177 mbsf, a downhole decrease in velocity and density and an abrupt increase of HSGR values and increased porosity followed by large troughs with either increased or decreased values in all logs indicate another significant change in lithology. On the FMS log, this change is imaged by a cemented layer above thin-bedded layers separated by conductive intercalations with higher clay content (Fig. F51). This interpretation of increased clay content is supported by increased potassium and thorium and decreased velocity values. The top of these alternations might correlate with the recovered firmground in Core 194-1194B-9R-1 that marks the boundary between lithologic Subunits IIIB and IVA (Figs. F49, F51), where the lithology changes from coarse skeletal packstone to fine-grained carbonate richer in clay (see "Lithostratigraphy and Sedimentology," p. 3). Subunit IVA has low overall core recovery, but the logs provide evidence for changes in sedimentation. For example, at 197 mbsf the log values, in particular velocity and density, become nearly constant down to a depth of 235 mbsf. At this depth, density shifts to slightly higher values and porosity shifts to lower values downhole. A negative velocity peak and a high gamma ray peak accompany this change, indicating the influx of siliciclastic material. Another, but less pronounced, gamma ray peak and low velocity values from 247 to 254 mbsf also might be related to increased siliciclastic input at the bottom of logging Unit 2 (Fig. F49). The increased gamma ray values are in concert with the observed general increase in siliciclastic material in Subunit IVA, in particular at the bottom and the top of this subunit (see "Lithostratigraphy and Sedimentology," p. 3). The occurrence of well-cemented beds at the bottom of the subunit, as indicated by high-velocity peaks, might correspond to bryozoan-rich intervals, one of which was recovered at 230 mbsf (curated depth).

Logging Unit 3 (260–425.5 mbsf)

A major change in the log signature and trend occurs at 260 mbsf, where porosity shifts downhole back to higher values from 30% to 60% and density rapidly decreases from 2.18 g/cm³ across the boundary to a low of 1.7 g/cm³ at 267 mbsf. Resistivity shifts back to lower values and HSGR displays smaller fluctuations from this point on downhole (Fig. F49). This major shift in log signature corresponds to the lithologic Subunit IVA/IVB boundary and represents a change from dolomitized clay-rich packstone to partly dolomitized grainstone without clay (see "Lithostratigraphy and Sedimentology," p. 3). Below the initial large excursions at 260 mbsf, the log curves again show the expected trends

F50. Dynamic and static FMS images and NGR logs, p. 81.

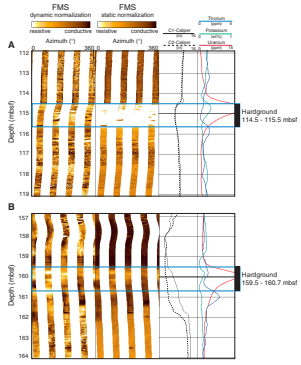

F51. Dynamic and static FMS image and NGR log across Unit III/IV boundary, p. 82.

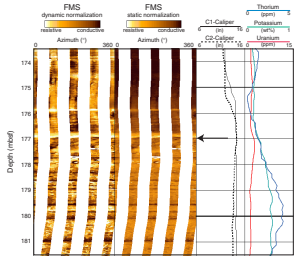

caused by increased overburden pressure; porosity decreases, whereas velocity and density increase. A small negative velocity peak at 325 mbsf and a small increase in HSGR are the log expressions of the boundary from lithologic Subunit IVB to Unit V (Fig. F49). Log changes of similar amplitude, however, occur in several places in Unit 3 between 260 and 371 mbsf.

At 371 mbsf, a major change in the HSGR and velocity logs occurs that corresponds to the boundary between lithologic Subunits VA and VB. From this point to the bottom of the hole, the HSGR log decreases and displays large and regularly spaced fluctuations, indicating a cyclic repetition of facies within the measured strata. The FMS images these cycles as 5- to 10-m-thick units, each consisting of thin alternating beds of high and low resistivity in the lower part and more homogeneous bioturbated beds in the upper part (Fig. F52A). As a result of low recovery, no distinct cycles were observed in the cored sediments. The FMS signature suggests that these cycles might contain a laminated basal portion with increased clay content and a more carbonate-rich, heavily bioturbated upper part.

Only the FMS tool, mounted at bottom of the logging string (see "Downhole Measurements," p. 30, in the "Explanatory Notes" chapter), penetrated 0.5 m into the basement. The top of the basement, indicated by a layer of high resistivity at 424.5 mbsf, has a steep dip of ~70° (Fig. F52B).

In summary, logs from Hole 1194B can be grouped into three logging units that correspond to the lithologic and seismic units adjacent to the NMP. Logging Unit 1 is an interval with low log values and corresponding high porosity values that correlates to the sediments of Megasequence D. Logging Unit 2 (114.5–260 mbsf) is characterized by large variations, which roughly coincide with the high-amplitude inclined reflections on the upper slope of the NMP. This variability is most likely the combined result of changes in sedimentation rates, siliciclastic content, and cementation, as is expected in pulsed, proximal-slope sedimentation. Logging Unit 3, from 260 mbsf to the bottom of the sedimentary strata, contains log signatures of low but regular variability typical of distal cyclic shelf sedimentation. Changes in log signatures in Hole 1194B correlate well with lithologic unit boundaries, indicating that facies changes across unit boundaries produce a distinct petrophysical signal. In low-recovery zones, such as in lithologic Subunit IVA, the logs document the existence of sedimentary subdivisions that were not easily discernible from the recovered sediments. For example, the lithologic Subunit IIIA/IIIB boundary was placed at 158 mbsf based on changes in the benthic foraminifer content. Log data indicate that lithologic Unit III consists of two sedimentary successions, each capped with a hardground top, equivalent to lithologic Subunits IIIA and IIIB. The base of Subunit IIIA, interpreted to be a platform facies, thus overlies the lower hardground surface.

Temperature Data

Temperature measurements were made from 423 mbsf to the seafloor (Fig. F53). The maximum temperature at the bottom of the hole is 29°C. This is probably not the true formation temperature, because pumping warm surface water downhole during drilling probably disturbed the in situ temperature regime. The measured temperature profile translates into a geothermal gradient of 22.5°C/km, if the borehole and the geological formation did indeed come into thermal equilib-

F52. Dynamic and static FMS images of basement and overlying sediments, p. 83.

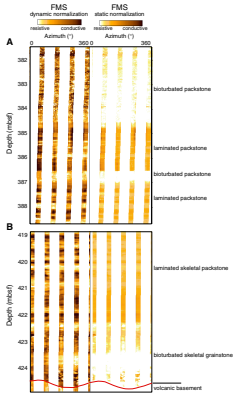

F53. Temperature vs. depth, p. 84.

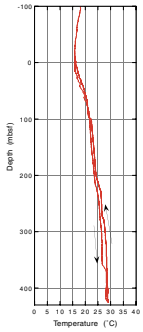

rium. This geothermal gradient is lower than the one estimated by the extrapolation of the temperature points measured with the APC temperature tool (see "Core Physical Properties," p. 19).

SEISMIC STRATIGRAPHY

Introduction

Site 1194 penetrated a 421-m-thick sedimentary section and 6 m of basement to a total depth of 427 mbsf. The drilled interval is comprised of hemipelagic drift sediments of seismic Megasequence D, proximal slope sediments of the NMP in Megasequence B, and the top of the acoustic basement (Fig. F54). The site is located on regional multichannel seismic line MAR13 at SP 3955 and at the intersection of local grid lines MAR24 (SP 355) and MAR27 (SP 1123). With Site 1193, Site 1194 forms a transect across the northern platform to the adjacent slope transition (Fig. F54; see also Fig. F7, p. 67, in the "Leg 194 Summary" chapter).

F54. Multichannel line MAR13, p. 85.

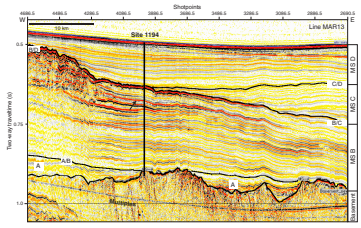

Time-Depth Conversion

No reliable check shot data were acquired at Site 1194 (see "Downhole Measurements," p. 22). As a result, the time-to-depth conversion for this site was calculated by integrating the sonic and density log data, and by completing the upper stratigraphic interval with shipboard velocity and density data collected from cores using the *P*-wave sensor, GRA, and MAD methods (see "Core Physical Properties," p. 19, and "Downhole Measurements," p. 22). To calibrate the integrated velocity curve, three tie points were defined that mark high-amplitude reflections, which can be correlated with confidence to significant horizons seen in cores and downhole logging data. These horizons are a hardground surface at 115 mbsf/633 ms two-way traveltime (TWT) (boundary between lithologic Units II and III; see "Lithostratigraphy and Sedimentology," p. 3), a second prominent hardground recognized only in downhole logging data at 160.0 mbsf/675 ms TWT, and the top of the acoustic basement at 423 mbsf/909 ms TWT.

A normal polarity, zero-phase wavelet of 80 ms in length was statistically extracted from the seismic data of line MAR13 and used for convolution of the downhole impedance curve and calculation of a synthetic seismogram (Fig. F55). The excellent match between synthetic and true seismic data in the upper 300 mbsf confirms the validity of the tie point assumptions made in the upper section, whereas a slight offset occurs toward acoustic basement.

F55. Synthetic seismogram plotted on MAR13 with core-to-seismic correlation, p. 86.

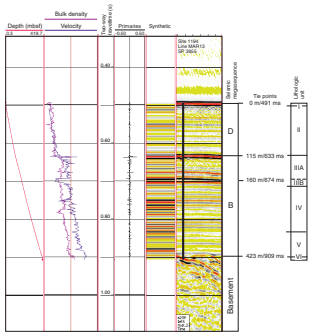

Megasequence D

Seismic Facies and Geometries

Megasequence D consists seismically of laterally continuous reflections that dip gently toward the southeast. Reflection amplitudes are generally low. This seismic facies, in conjunction with the large-scale geometry of the megasequence, is interpreted to be the record of a drift package. Several smaller-scale unconformities within Megasequence D indicate the occurrence of hiatuses within the drift package. At Site 1194, Megasequence D infills a preexisting shallow depression between

the elevated margin of the NMP to the northwest and a drift bulge of Megasequence C to the southeast (Fig. F7, p. 67, in the "Leg 194 Summary" chapter) so that, compared with Site 1193, Megasequence D is expanded. However, an unconformity shallow in the core (see "Age Model," p. 15) marks the base of a southeastward dipping and thickening wedge indicating that the uppermost part of Megasequence D is strongly condensed (Fig. F54).

The base of Megasequence D is defined to the northwest as an onlap surface onto Megasequence B along the NMP margin (seismic Megasequence B/D boundary). Approximately half of the thickness of Megasequence D at Site 1194 onlaps onto the NMP and is thus missing on top of the platform at Site 1193 (Fig. F54). This coincides well with the differences in age of the base of Megasequence D between the two sites (see below). The lower boundary of Megasequence D changes its signature from an onlap surface onto Megasequence B in the northwest to a conformable contact on top of Megasequence C to the southeast, where Megasequence C forms a wedge onlapping Megasequence B. At Site 1194, Megasequence C is absent, but it occurs immediately downdip of Site 1193 to the east underlying the Megasequence C/D boundary (Fig. F55).

Correlation with Cores

Megasequence D incorporates lithologic Unit I and part of Unit II, ranging in age from late Miocene to Pleistocene (see "Lithostratigraphy and Sedimentology," p. 3, and "Age Model," p. 15). The sediment mostly consists of 114 m of light olive to greenish gray mudstone/wackestone interbedded with minor packstone intervals. Using biostratigraphic datums, the base of Megasequence D at Site 1194 was dated ~7.7 Ma, whereas the basal section at Site 1193 was dated ~5.6 Ma (i.e., 2.5 m.y. younger).

Megasequence B

Seismic Facies and Geometries

The top of Megasequence B is defined by a prominent high-amplitude reflection at 633 ms TWT/115 mbsf that displays an irregular topography. This megasequence boundary retains its high amplitude and irregular geometry as it continues upslope (the Megasequence B/D boundary) forming an onlap surface onto the top of the NMP (Fig. F54; see Fig. F7, p. 67, in the "Leg 194 Summary" chapter). Downslope along seismic line MAR13, the B/C boundary maintains these characteristics for ~10 km, but slowly loses its high amplitude and changes gradually into a medium-amplitude, conformable reflection. The top of Megasequence B at Site 1194 marks a depositional hiatus between Megasequence B and Megasequence D from 7.7 to 11.8 Ma (see "Age Model," p. 15).

A second high-amplitude reflection can be mapped within Megasequence B at 674 ms TWT/160 mbsf (marked by arrow on Fig. F54). It shows very similar characteristics as the reflection at the top of Megasequence D. The seismic package, bracketed between these two high-amplitude reflections (633–674 ms TWT), is characterized by low internal reflection amplitudes and onlaps upslope onto the shallow-water sediments of the NMP, indicating a depositional age that postdates the end of NMP growth (Fig. F54).

A third high-amplitude reflection occurs at 695 ms TWT/180 mbsf but does not continue as far as the two reflections above. Below this package, the seismic facies of Megasequence B is mostly characterized by medium- to low-amplitude reflections that are laterally continuous and gently dip toward the southeast. No major seismic unconformities occur in this lower part of Megasequence B. Megasequence A is absent at this site; however, the A/B boundary, as it was determined at Site 1193 (see **"Seismic Stratigraphy,"** p. 27, in the "Site 1193" chapter), terminates on the top of the acoustic basement immediately northwest of the location of Site 1194 (Fig. **F54**).

Correlation with Cores

The strong reflection defining the top of Megasequence B can be clearly correlated with the cores and the logs to a well-indurated grainstone layer that is coated with a possibly phosphatic hardground, thus showing the effects of submarine diagenesis. This layer marks the top of lithologic Unit III. The log signature of this hardground with high density, resistivity, velocity, and very high uranium values is identical with a second horizon at 160 mbsf only seen in the logs and not recovered in the cores (see **"Downhole Measurements,"** p. 22). This second hardground coincides with the second reflection in Megasequence B. The third prominent reflection most likely coincides with the Unit III/IV boundary that is described as a firmground (see **"Lithostratigraphy and Sedimentology,"** p. 3). Units IIIA and IIIB are interpreted to be deposited in a neritic ramp and neritic upper-slope setting, respectively (see **"Biostratigraphy and Paleoenvironments,"** p. 9, and **"Lithostratigraphy and Sedimentology,"** p. 3). Such settings differ significantly from the over- and underlying hemipelagic units, which have a more regular and laterally continuous seismic facies. The onlapping seismic package, between the two high-amplitude reflections coinciding with lithologic Subunit IIIA, is dated as ~11.8–13.2 Ma (see **"Age Model,"** p. 15) and represents a succession that was deposited as a lowstand platform during part of the late middle to late Miocene sea level lowstand in front of the NMP margin. The strong amplitude and irregular surface of the top of Megasequence B indicate that this surface could even have been altered and eroded under subaerial conditions. The downslope decay of the high-amplitude signature at ~655–690 ms TWT/140–170 mbsf (Fig. **F54**) (line MAR13; SP 3800-3200) may mark the maximal extent of exposure. However, no lithologic or geochemical data obtained from the hardground at the boundary between Units II and III could prove the assumptions of subaerial exposure (see **"Lithostratigraphy and Sedimentology,"** p. 3).

The lower part of Megasequence B coincides with lithologic Units IV and V, consisting mostly of silt-sized packstone and grainstone that changes into a skeletal packstone at the base of the unit. The bulk of these sediments are interpreted to be slope sediments shed from the NMP mixed with a minor siliciclastic component. This composition can be expected from the seismic geometry that shows gently dipping slope reflections from a carbonate platform. An age of ~21.6 Ma was assigned to the sediments directly overlying basement (see **"Age Model,"** p. 15). Because this site is located on a basement high that apparently became an island during transgression (Fig. **F6,** p. 66, in the "Leg 194 Summary" chapter), the oldest sediments recovered are carbonates, which are distinctly different than the lowermost sediments at Site

1193, where a siliciclastic and partly conglomeratic sequence was recovered.

Acoustic Basement

Seismic Facies and Geometries

Acoustic basement is recognized as a highly irregular surface that generally dips to the southeast. Site 1194 is situated on a basement high at 909 ms, which is 30–40 m above the surrounding topography. The top of acoustic basement is marked by an unconformity surface with numerous diffractions and truncated reflections.

Correlation with Cores

Basement at this site was reached at 423 mbsf. It consists of a reddish black altered extrusive rock. Velocity values reach, on average, 5000 m/s, which contrasts sharply to the values from overlying sediments that have velocity values of less than 3000 m/s (see **"Core Physical Properties,"** p. 19).

REFERENCES

Anselmetti, F.S., and Eberli, G.P., 1993. Controls on sonic velocity in carbonates. *Pure Appl. Geophys.,* 141:287–323.

Athy, L.F., 1930. Density, porosity, and compaction of sedimentary rocks. *AAPG Bull.,* 14:1–24.

James, N.P., Collins, L.B., Bone, Y., and Hallock, P., 1999. Subtropical carbonates in a temperate realm: modern sediments on the southwest Australian shelf. *J. Sediment. Res.,* 69:1297–1321.

Keen, C., and Beaumont, C., 1990. Geodynamics of rifted continental margins. *In* Keen, M.J., and Williams, G.L. (Eds.), *Geology of the Continental Margin of Eastern Canada*. Geol. Soc. Am., 1:391–472.

Longman, M.W., 1981. Carbonate diagenesis as a control on stratigraphic traps. *AAPG Continuing Education Course Notes,* 21.

Maher, B.A., and Thompson, R., 1999. *Quaternary Climates, Environments and Magnetism:* Cambridge (Cambridge Univ. Press).

Melim, L.A., Swart, P.K., and Maliva, R.G., 1995. Meteoric-like fabrics forming in marine waters: implications for the use of petrography to identify diagenetic environments. *Geology,* 23:755–758.

Struckmeyer, H.I.M, and Symonds, P.A., 1997. Tectonostratigraphic evolution of the Townsville Basin, Townsville Trough, offshore northeastern Australia. *Aust. J. Earth Sci.,* 44:799–817.

Wyllie, M.R.J., Gregory, A.R., and Gardner, L.W., 1956. Elastic wave velocities in heterogeneous and porous media. *Geophysics,* 21:41–70.

Figure F1. Bathymetry map showing locations of Leg 194 sites.

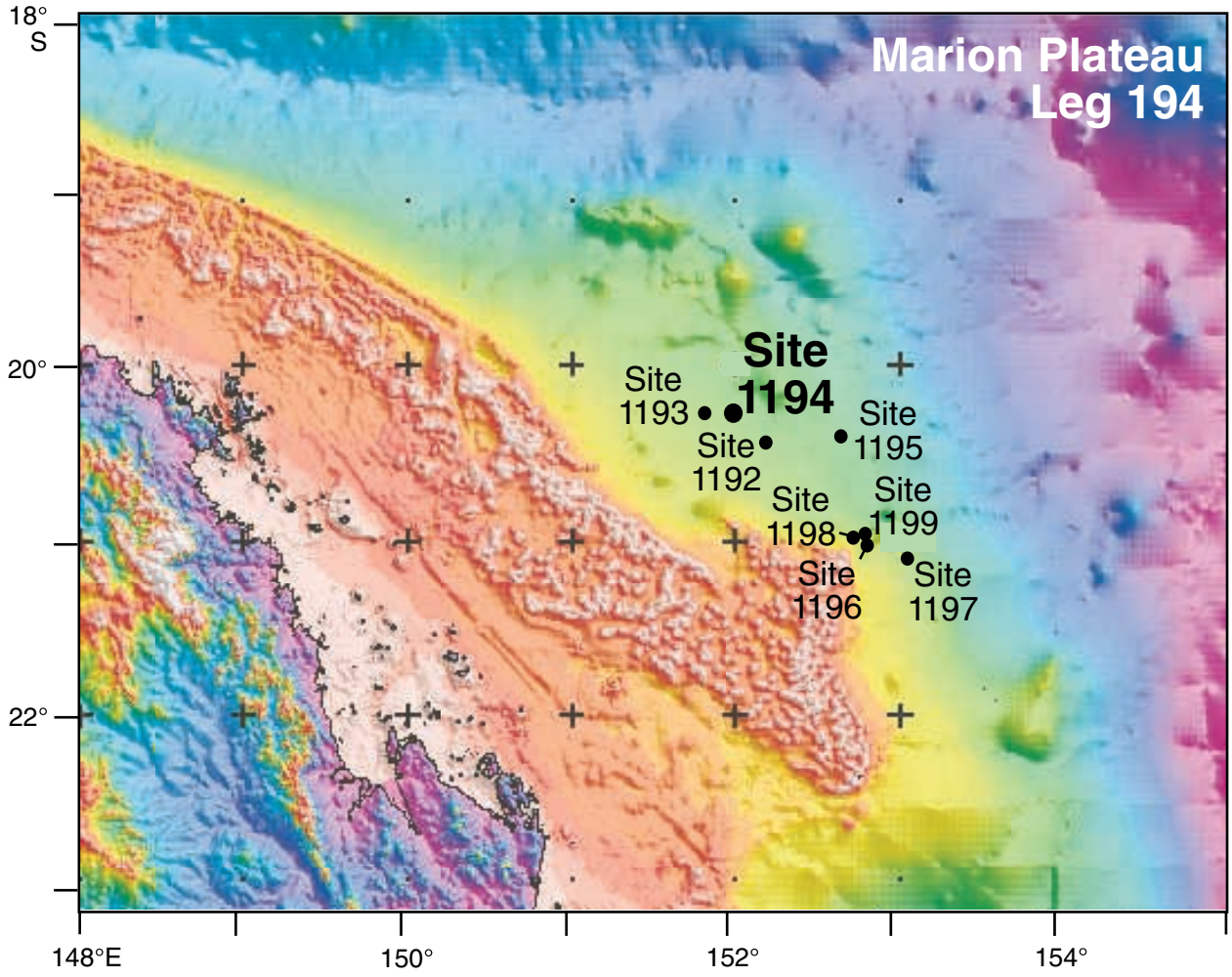

Figure F2. Seismic line MAR13 with locations of Sites 1193 and 1194. MS = Megasequence, NMP = Northern Marion Platform.

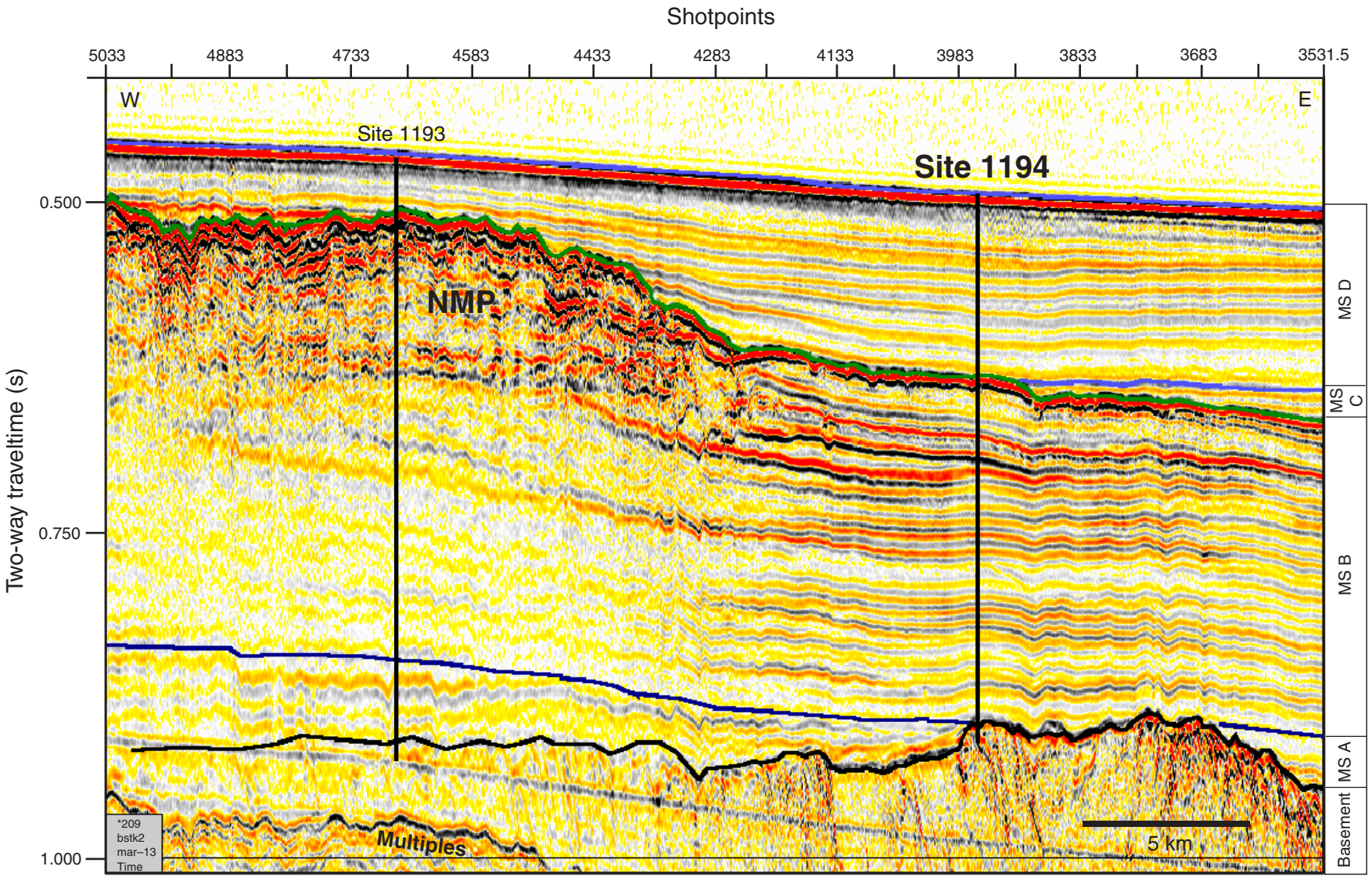

Figure F3. Lithologic summary for Site 1194. **A.** Core recovery. Black = recovered, white = gap (<100% recovery). **B.** Lithologic units as defined in this section. **C.** Lithology. **D.** Carbonates (wt%) vs. the noncarbonate fraction of the sediment estimated by X-ray diffraction (see **"Geochemistry,"** p. 16). **E.** Dunham texture. **F.** Lithification. **G.** Grain size. **H.** Interpretation of the recovered facies. **I.** Epochs for the site (see **"Biostratigraphy and Paleoenvironments,"** p. 9).

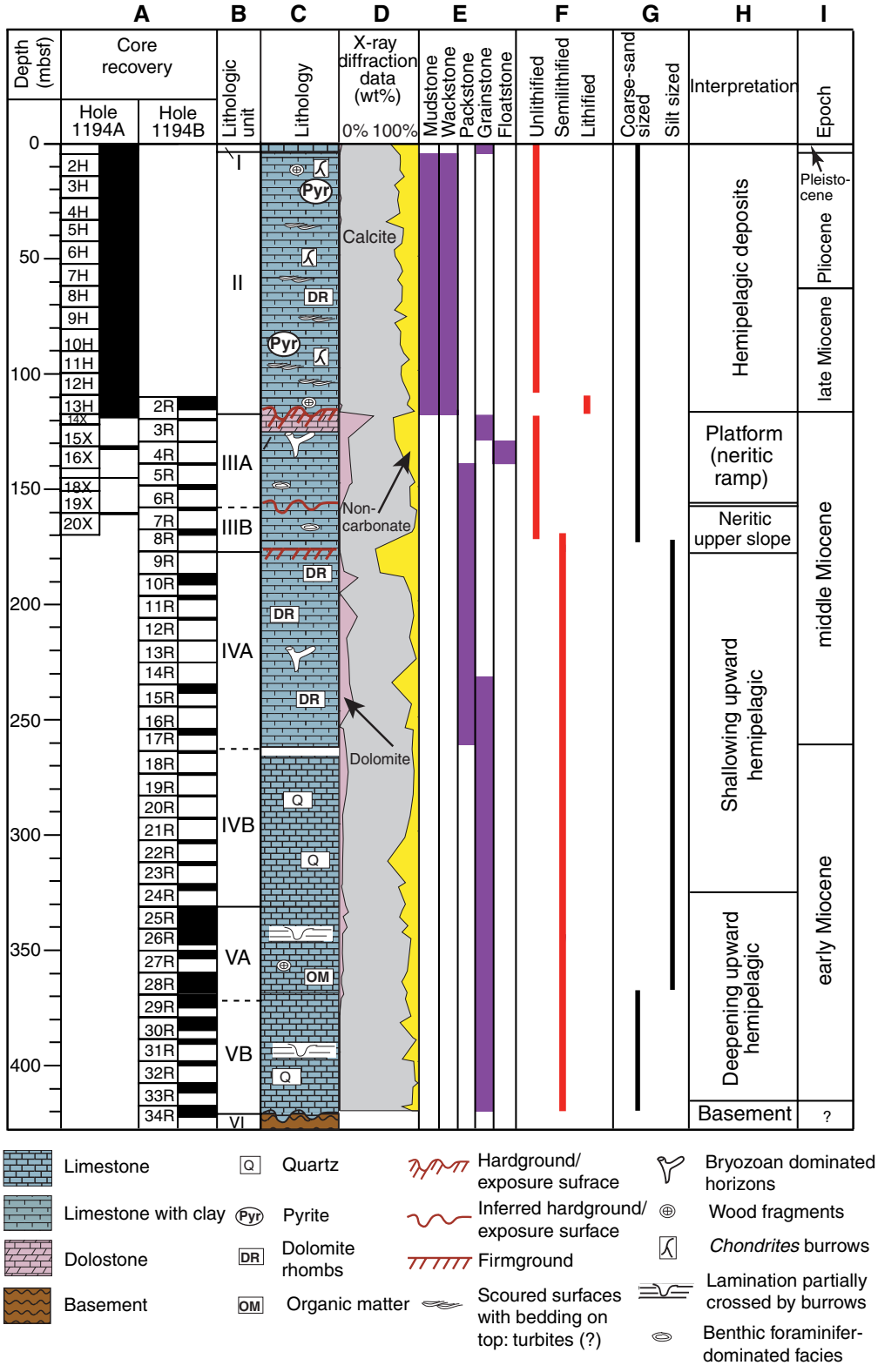

Figure F4. Skeletal grainstone characteristic of Unit I (interval 194-1194A-1H-1, 5–25 cm). Grains are dominated by planktonic foraminifers.

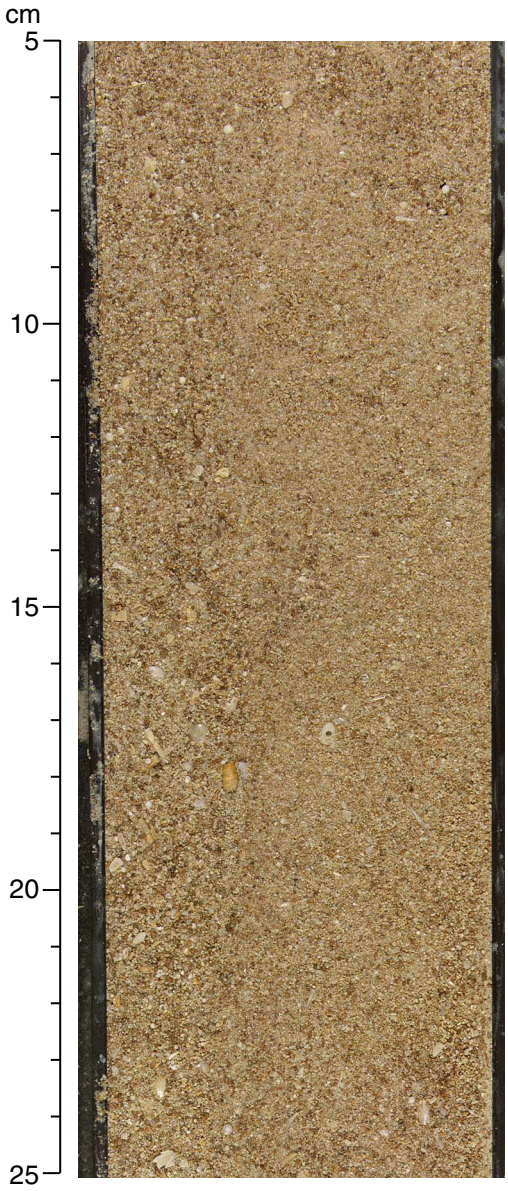

Figure F5. Close-up photograph of Unit II (interval 194-1194A-12H-4, 40–60 cm). The color, wackestone/mudstone texture, and scarce skeletal components are typical for the unit.

Figure F6. Close-up photograph of scoured surfaces in interval 194-1194A-9H-3, 30–50 cm.

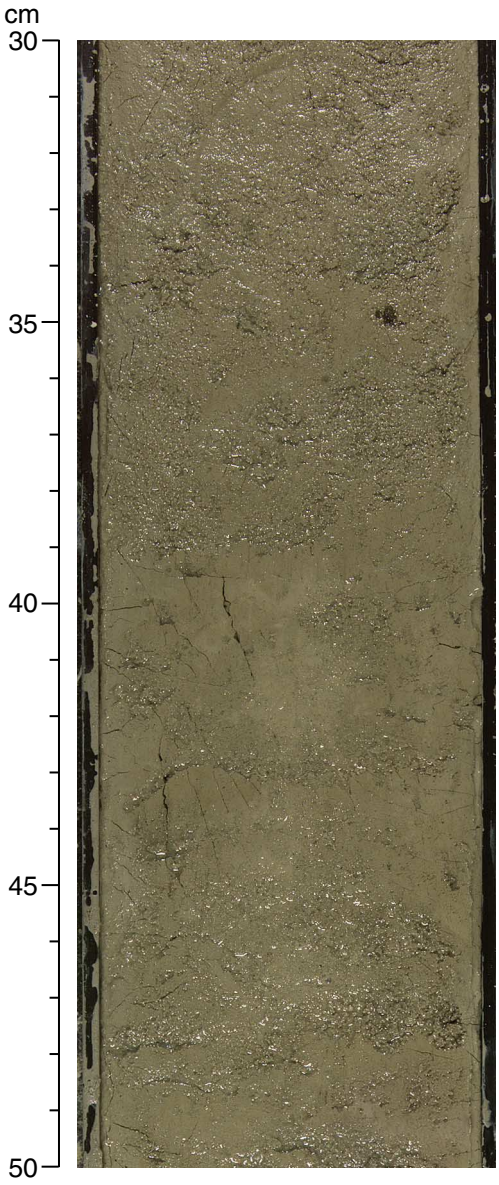

Figure F7. Close-up photograph of a hardground interval at the top of Unit III (interval 194-1194A-14X-1, 0–30 cm). The brown crust is likely to be phosphatized and to contain ferromanganese mineralizations.

Figure F8. Photomicrograph of the top of the recovered hardground in Core 194-1194A-14X. The wavy phosphatic and ferromanganese lamination, the alternation of lighter (a) and darker (b) laminae is similar to a stromatolithic buildup.

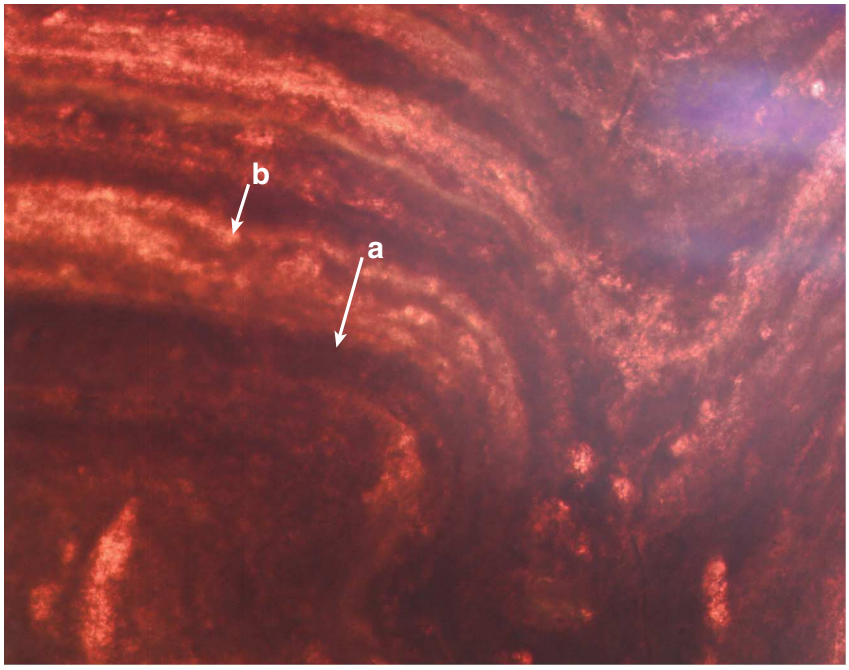

Figure F9. Close-up photograph of a dolomitized interval below the phosphatized crust of the top of Unit III (interval 194-1194A-14X-1, 25–45 cm).

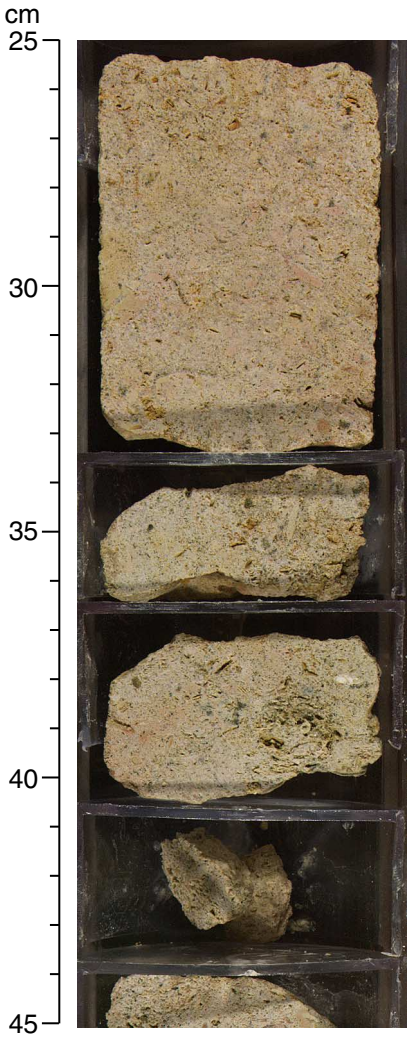

Figure F10. Photomicrograph of the recovered hardground in Core 194-1194A-14X. **A.** Syntaxial overgrowth of cement around a planktonic foraminifer (a). **B.** Syntaxial overgrowth of cement around a planktonic foraminifer (a). Syntaxial overgrowth of cement around a high-Mg calcite echinoid fragment (b). The high-Mg particle is preserved (c).

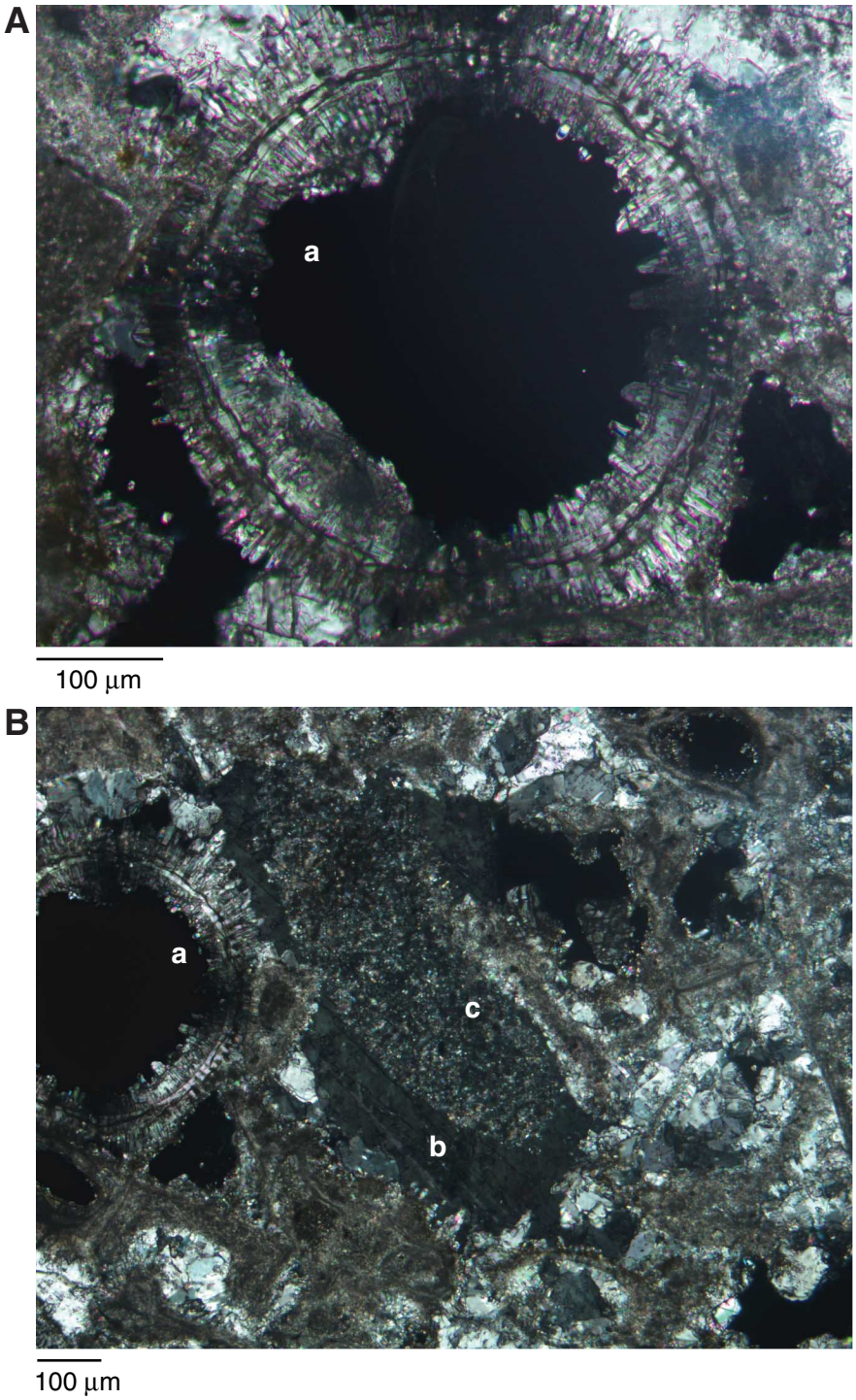

Figure F11. Close-up photograph of a skeletal floatstone characteristic of Subunit IIIA with well-preserved bryozoans, common bivalve fragments, and present benthic foraminifers (interval 194-1194A-16X-1, 65–85 cm).

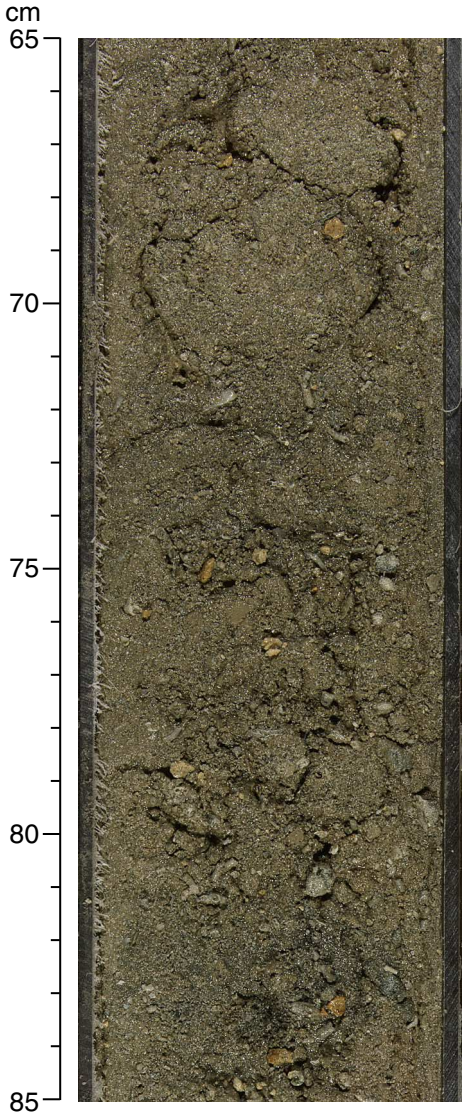

Figure F12. Photomicrograph of the lithology from Subunit IIIA (Sample **194-1194B-2R-4, 69 cm**). Well-preserved bryozoan fragments (a) are common throughout the unit.

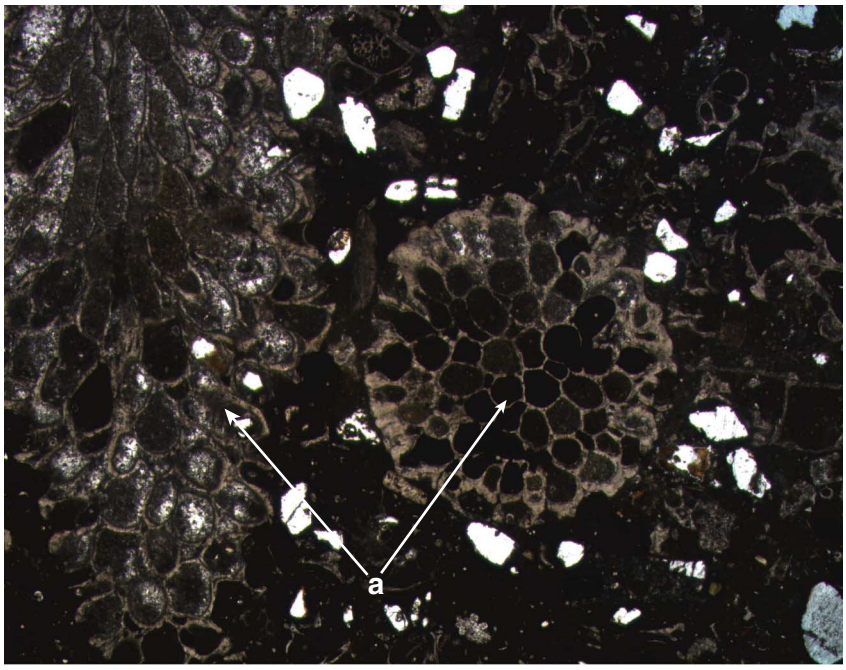

Figure F13. Close-up photograph of skeletal packstone dominated by larger benthic foraminifers in Subunit IIIB (interval 194-1194A-20X-CC, 19–40 cm).

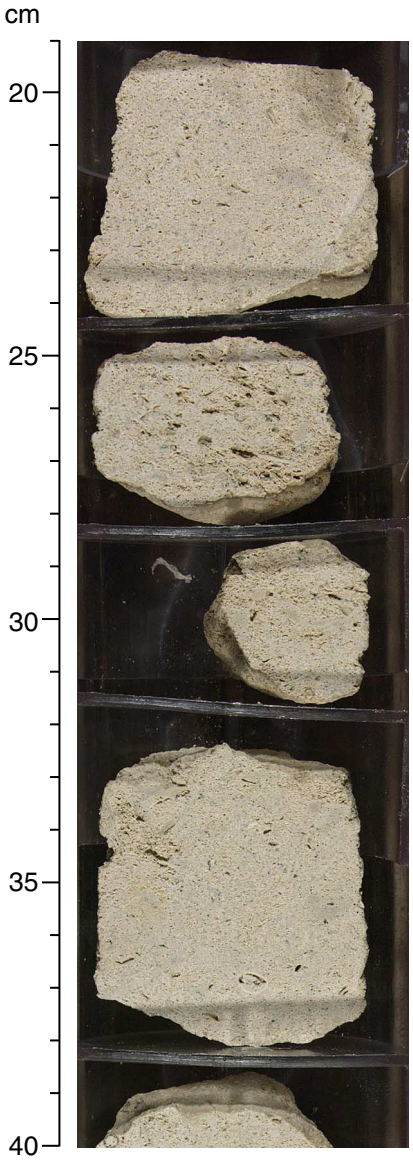

Figure F14. Close-up photograph of silt-sized packstone/grainstone of Subunit IVA (interval 194-1194B-10R-2, 5–25 cm). No or few skeletal fragments can be identified.

Figure F15. Photomicrograph of Subunit IVA (Sample 194-1194B-10R-3, 51 cm). **A.** Silt-sized carbonate matrix with one echinoid spine (a). **B.** General view of the section (b) and rare dolomite rhombs. No skeletal fragments can be identified because of their size.

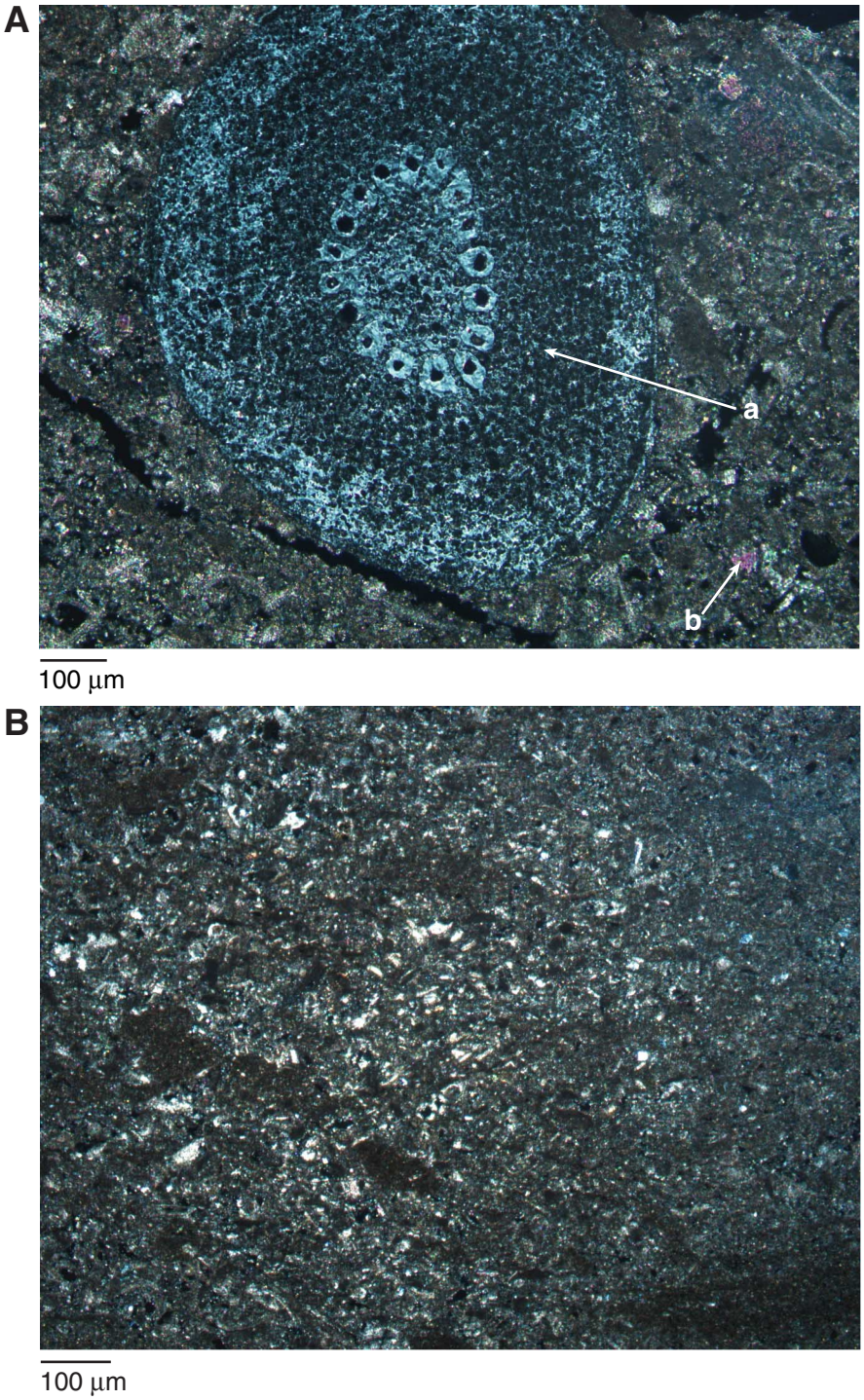

Figure F16. Close-up photograph of the sediment of Subunit IVB (interval 194-1194B-24R-1, 55–75 cm).

Figure F17. Photomicrograph of sediments from Subunit IVB (Sample **194-1194B-24R-1, 55 cm**). Quartz grains are abundant (a) with rare planktonic foraminifers (b). The rest of the matrix is dark, possibly organic-rich, and has no identifiable skeletal components.

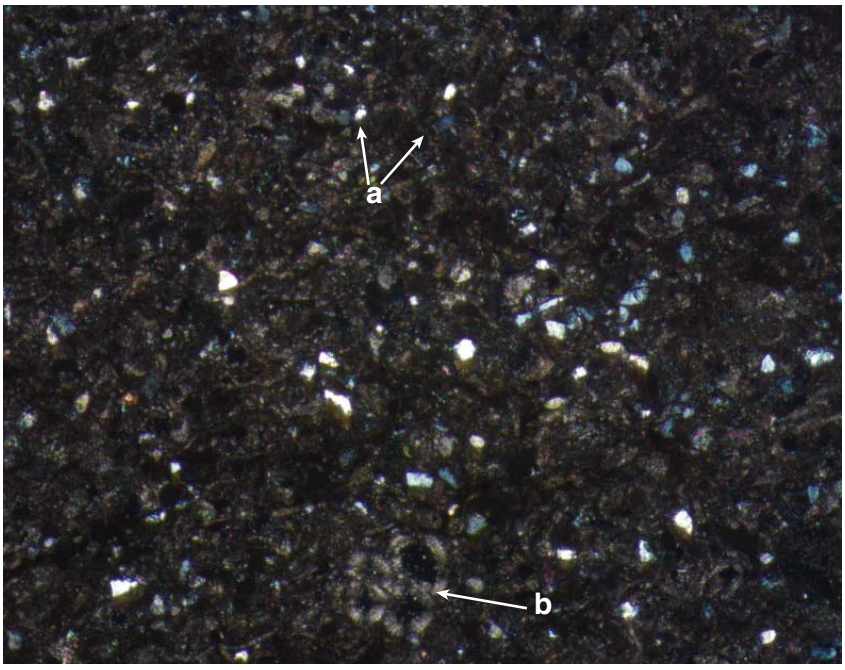

Figure F18. Close-up photograph of silt-sized packstone with bioturbation from Subunit VA (interval 194-1194B-25R-3, 20–40 cm).

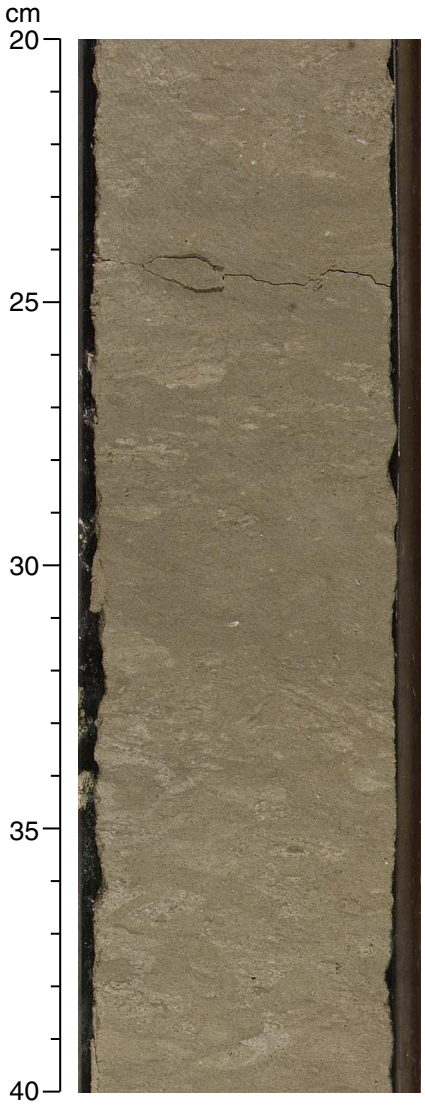

Figure F19. Photomicrograph of sediments from Subunit VA (Sample **194-1194B-25R-2, 46 cm**). Note the rare planktonic foraminifers (a), shell fragments (b), and the dominance of silt-sized particles (c) in a dark, wavy matrix.

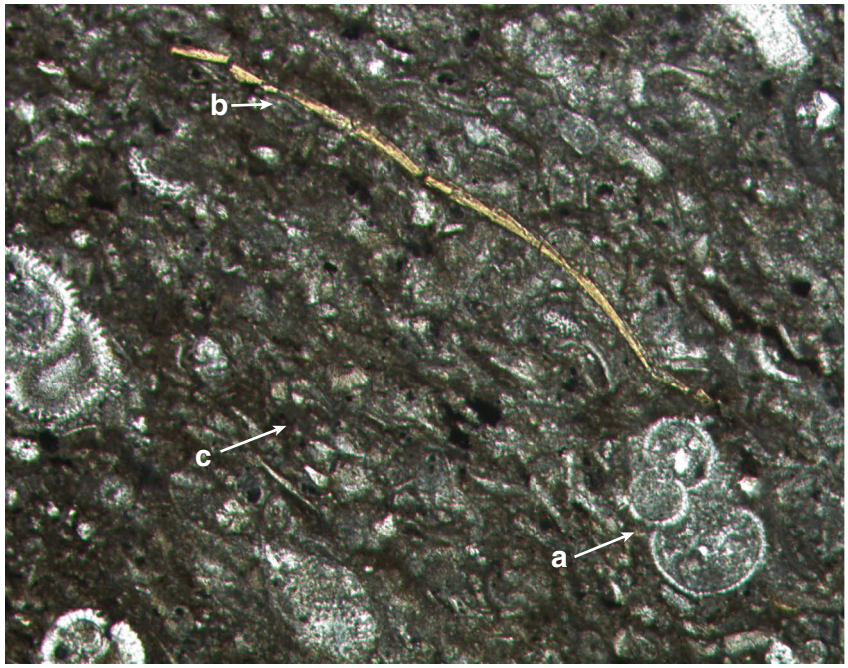

Figure F20. Close-up photograph of skeletal packstone characteristic of Subunit VB with layering crosscut by burrows (interval 194-1194B-30R-3, 15–35 cm).

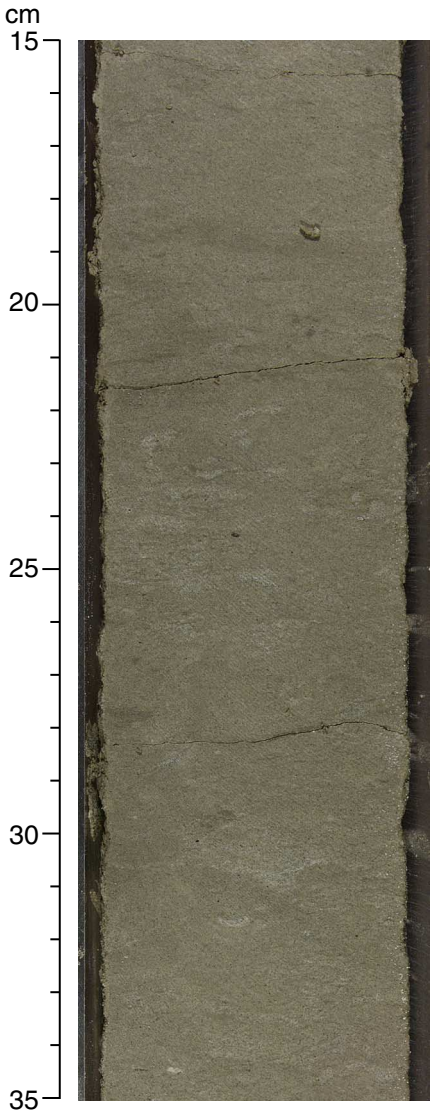

Figure F21. Photomicrograph of sediments characteristics of the upper portion of Subunit VB (Sample 194-1194B-31R-1, 104 cm). Skeletal components include benthic foraminifers (b), planktonic foraminifers (c), and echinoid spines. Glauconite is common (a).

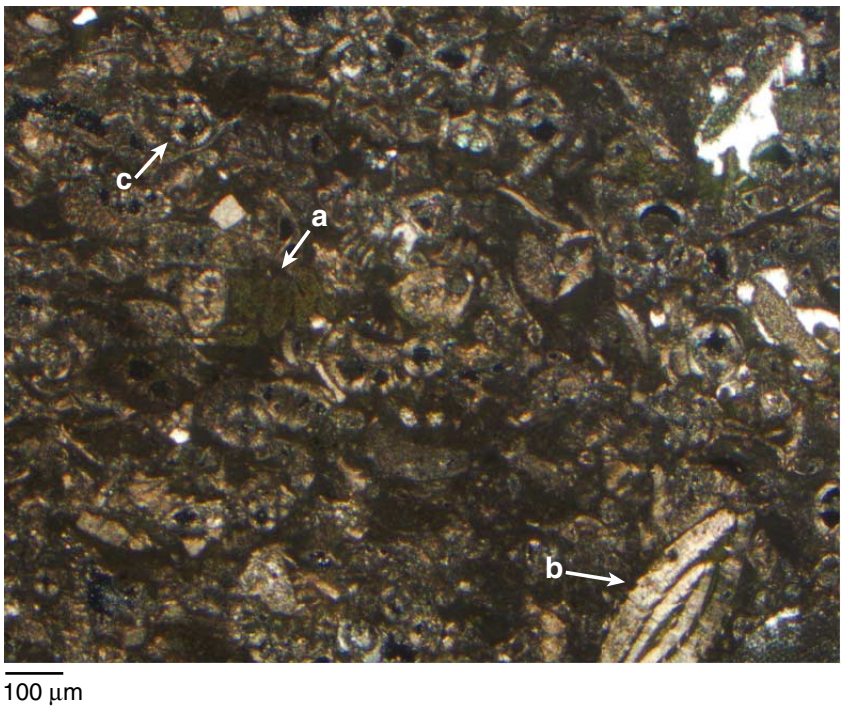

Figure F22. Photomicrograph of sediments characteristic of the lower portion of Subunit VA, immediately overlying basement (Sample **194-1194B-34R-3, 11 cm**). Note the larger benthic foraminifers (*Lepidocyclina*) (a) aligned parallel to the bedding plane.

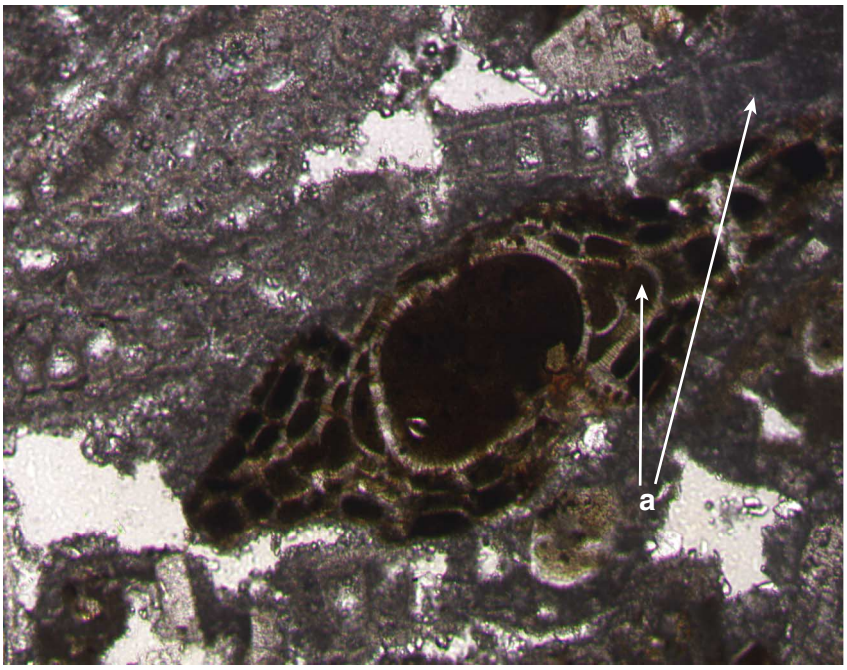

Figure F23. Close-up photograph of weathered olivine basalt composing Unit VI (interval 194-1194B-34R-5, 10–30 cm). This lithology represents the acoustic basement at Site 1194.

Figure F24. Photomicrograph of the olivine basalt characteristic of Unit VI (Sample **194-1194B-34R-4, 65 cm**). Olivine phenocrysts (a) are located in a plagioclase matrix (b).

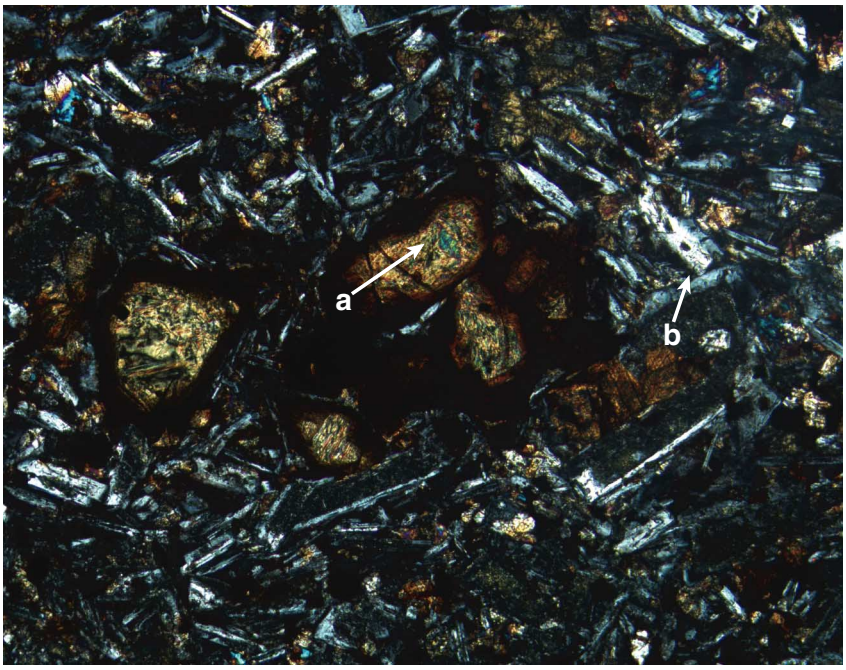

Figure F25. Long-core measurements of intensity and inclination of sediments from 0 to 100 mbsf in Hole 1194A. Note the strong core-top intensity anomalies, which corrupt the inclination record with positive values.

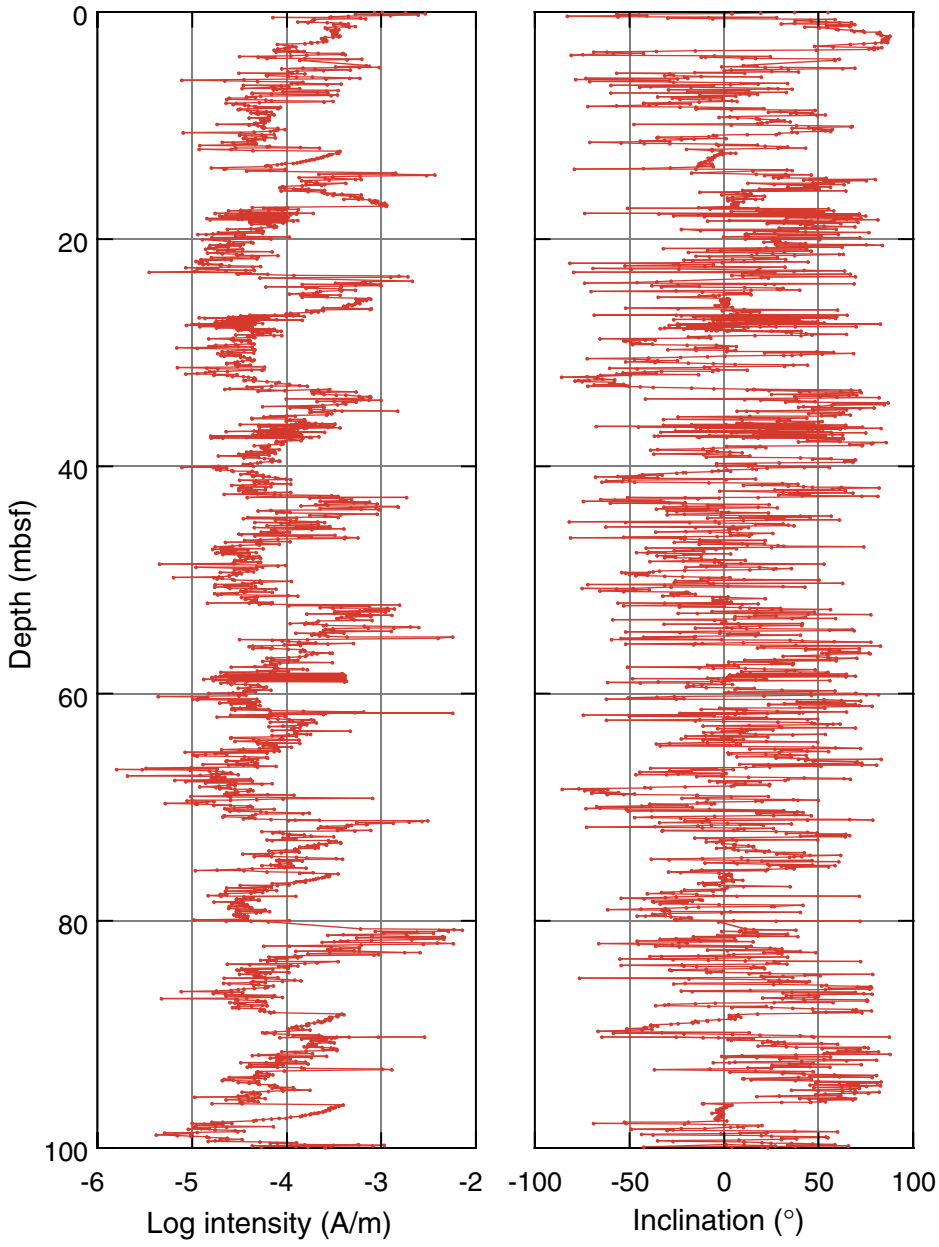

Figure F26. Long-core measurements of z-intensity and inclination of sediments from 0 to 100 mbsf filtered to remove core-top magnetic anomalies. The z-intensity values were balanced around a biased zero line. A provisionally interpreted magnetostratigraphy is shown at bottom right.

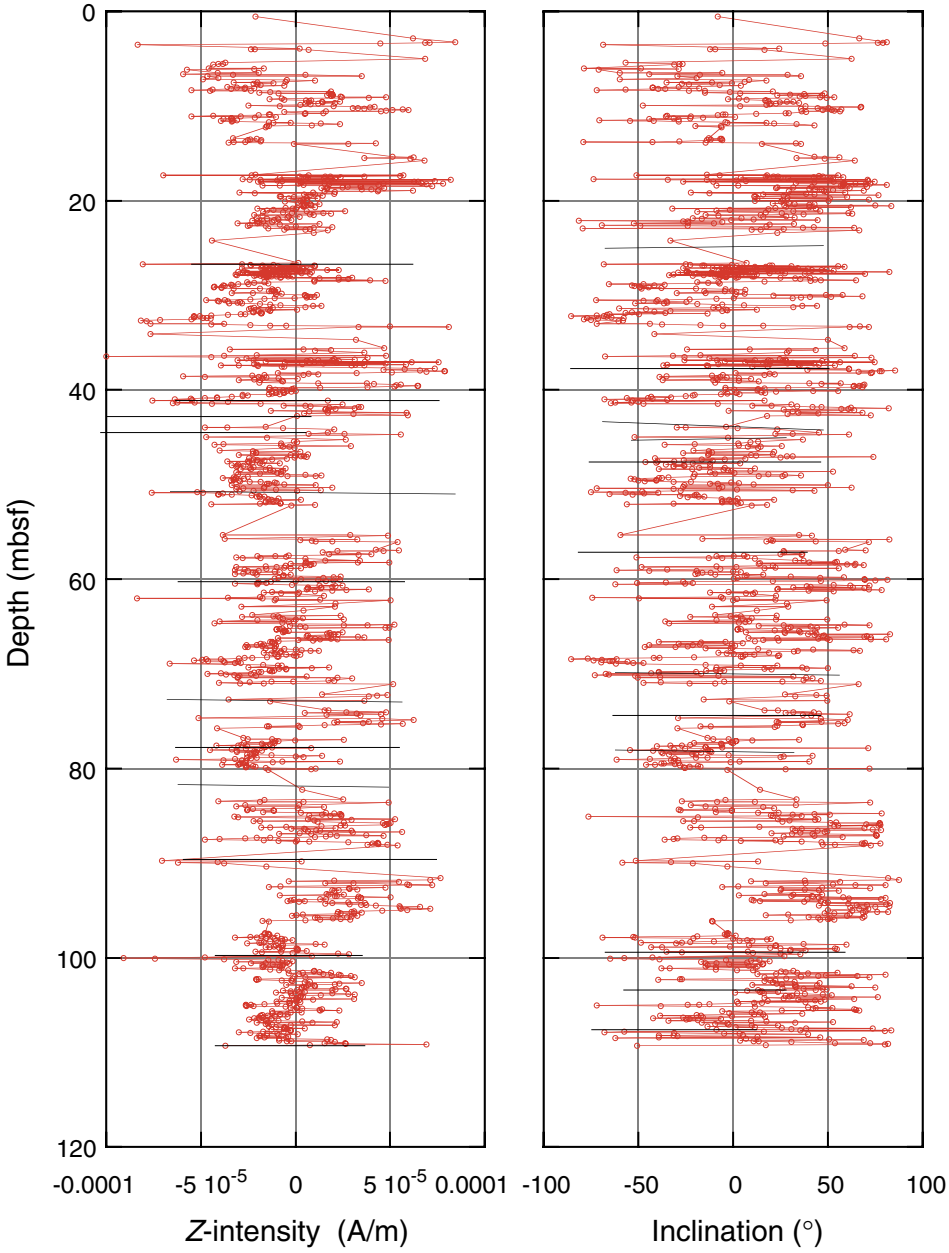

Figure F27. Long-core measurements of intensity and inclination of sediments from 300 to 400 mbsf in Hole 1194A. Black and white column on the right indicates possible normal (black) and reversed (white) polarity intervals.

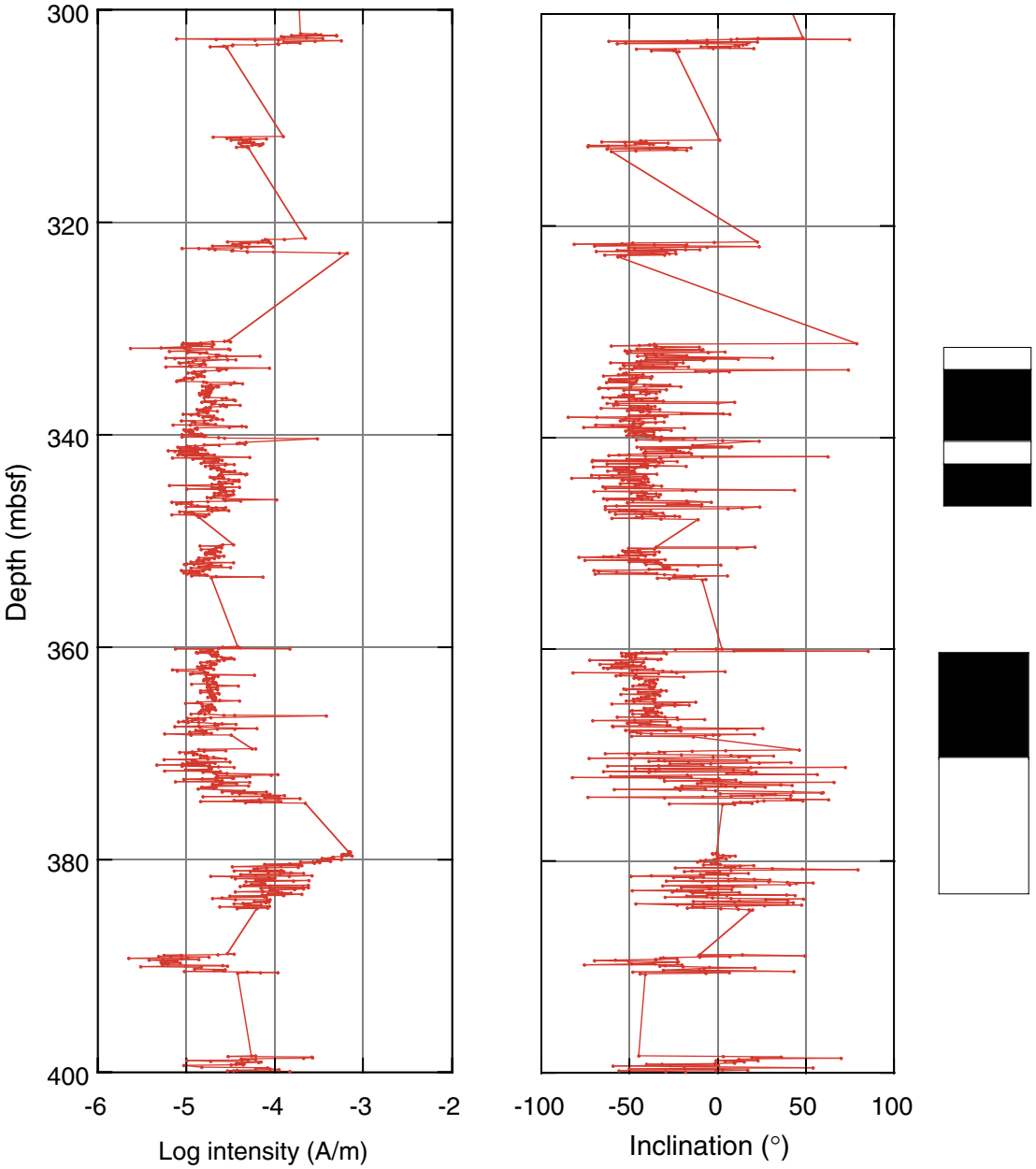

Figure F28. Analysis of natural remanent magnetization (NRM) by AF demagnetization. **A.** Sample 194-1194B-34R-2, 45–47 cm. **B.** Sample 194-1194B-34R-5, 12–14 cm. DEC = declination, INC = inclination, MAD = moisture and density.

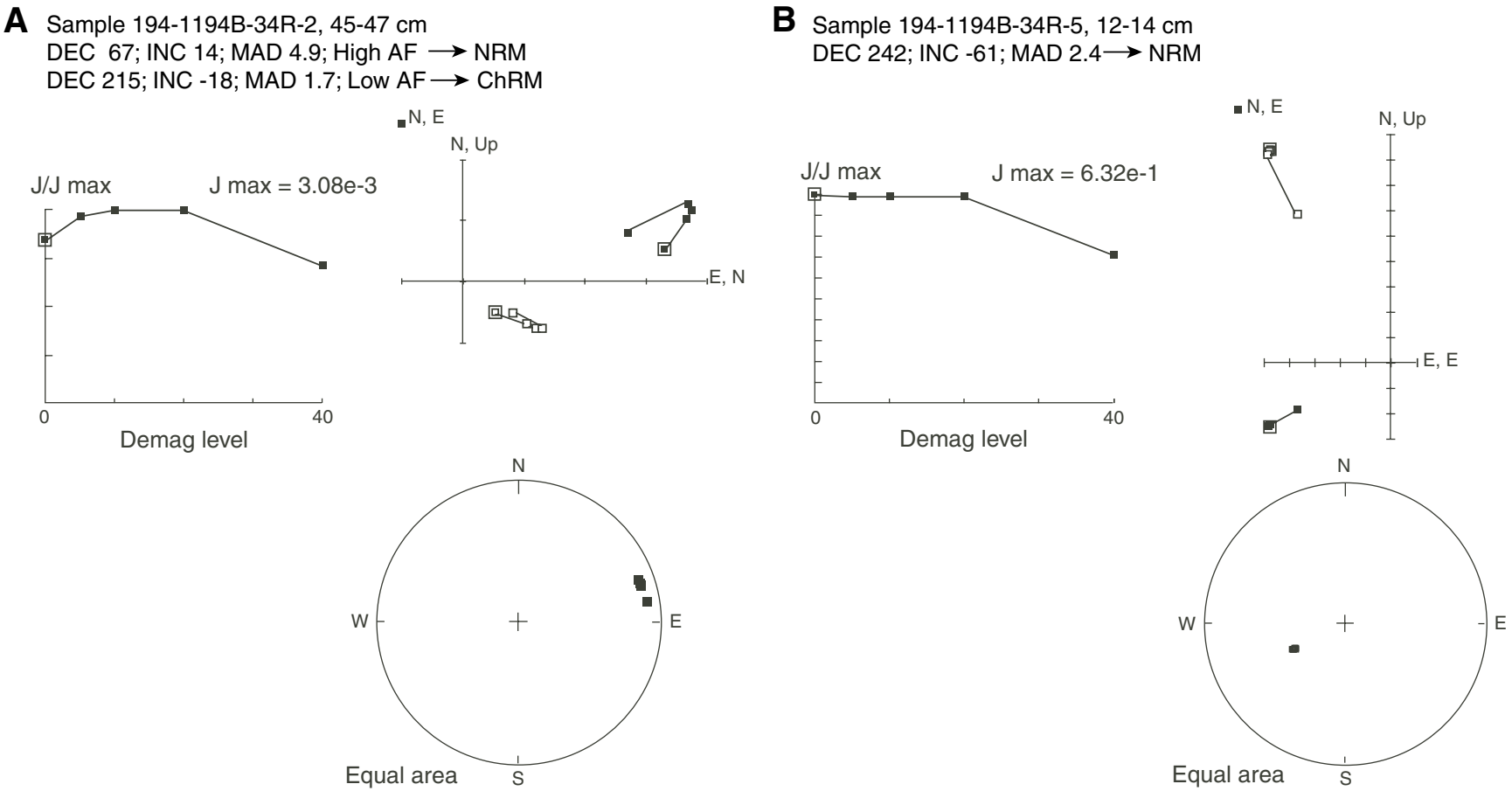

Figure F29. Remanent magnetism characteristics of Sample 194-1194B-4R-1, 22–24 cm. NRM = natural remanent magnetization, ARM = anhysteretic remanent magnetization, IRM = isothermal remanent magnetization, ACQ = acquisition.

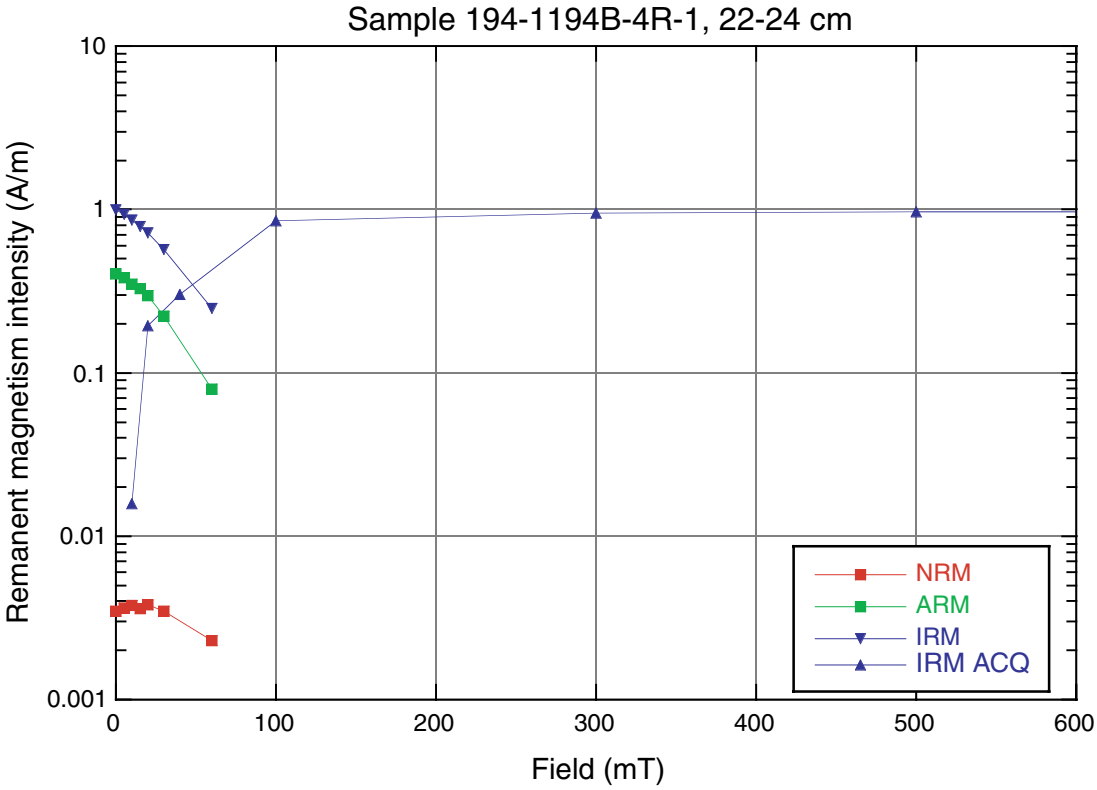

Figure F30. Variation of remanent magnetism (RM) characteristics downhole. Note the strong magnetic material in basement and immediately above. There is evidence for a hard phase, probably hematite, at a depth of ~120 mbsf, coinciding with a hardground surface. NRM = natural remanent magnetization, ARM = anhysteretic remanent magnetization, IRM = isothermal remanent magnetization.

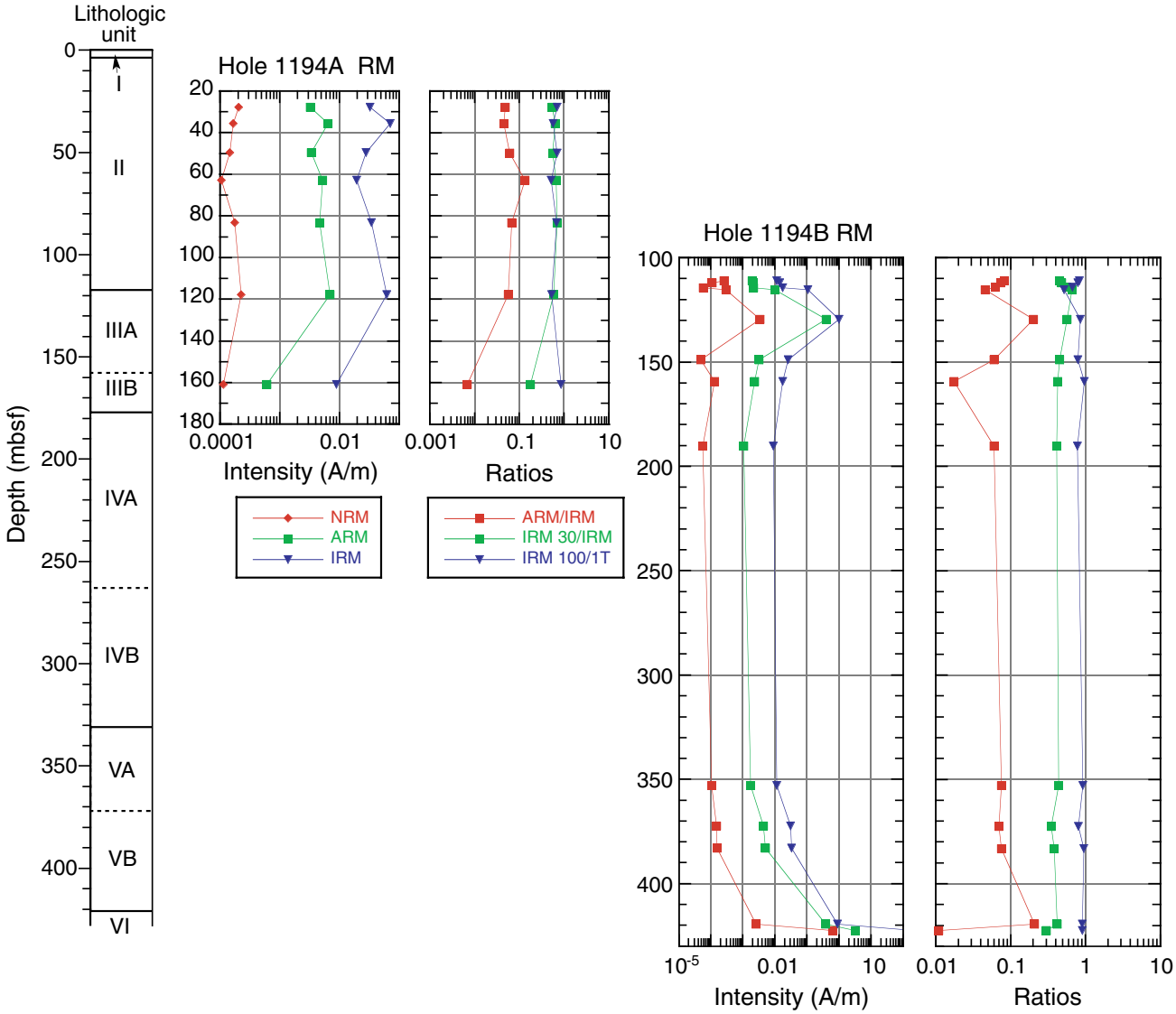

Figure F31. Age-depth model and sedimentation rates at Site 1194. Horizontal lines spanning from the left figure margin to the age-depth curve are lithologic unit (solid) and subunit (dashed) boundaries. Horizontal lines spanning from the right margin of the figure to the age-depth curve are seismic megasequence boundaries (solid) and major reflectors within megasequences (dashed). Vertical lines are epoch boundaries as labeled at the top of the diagram. BSMT = basement, MS = Megasequence.

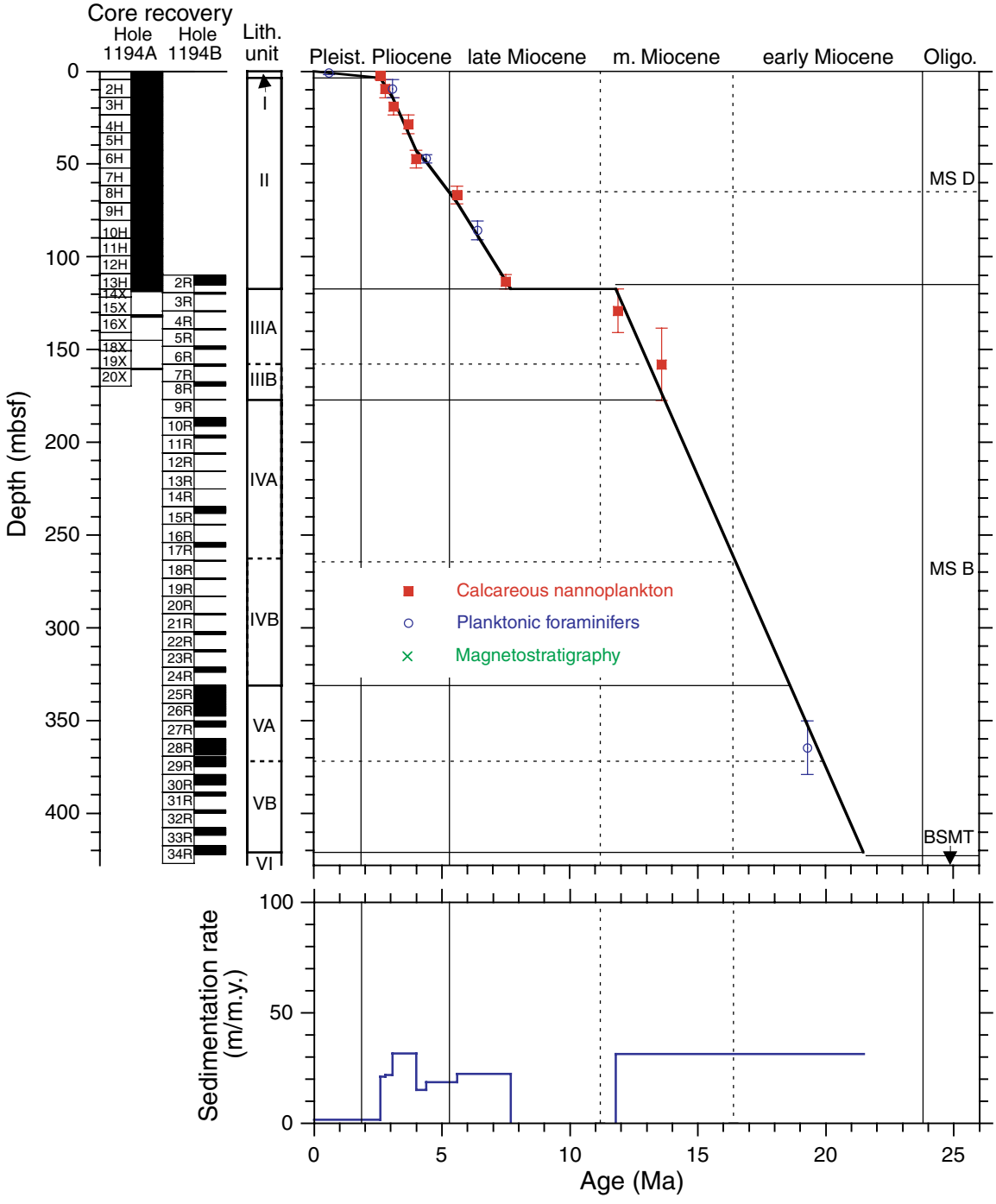

Figure F32. Concentrations of dissolved constituents vs. depth, Site 1194. **A.** Chloride. **B.** Alkalinity. **C.** Sulfate. **D.** Ammonium. **E.** Magnesium. **F.** Calcium. **G.** Strontium. **H.** Potassium.

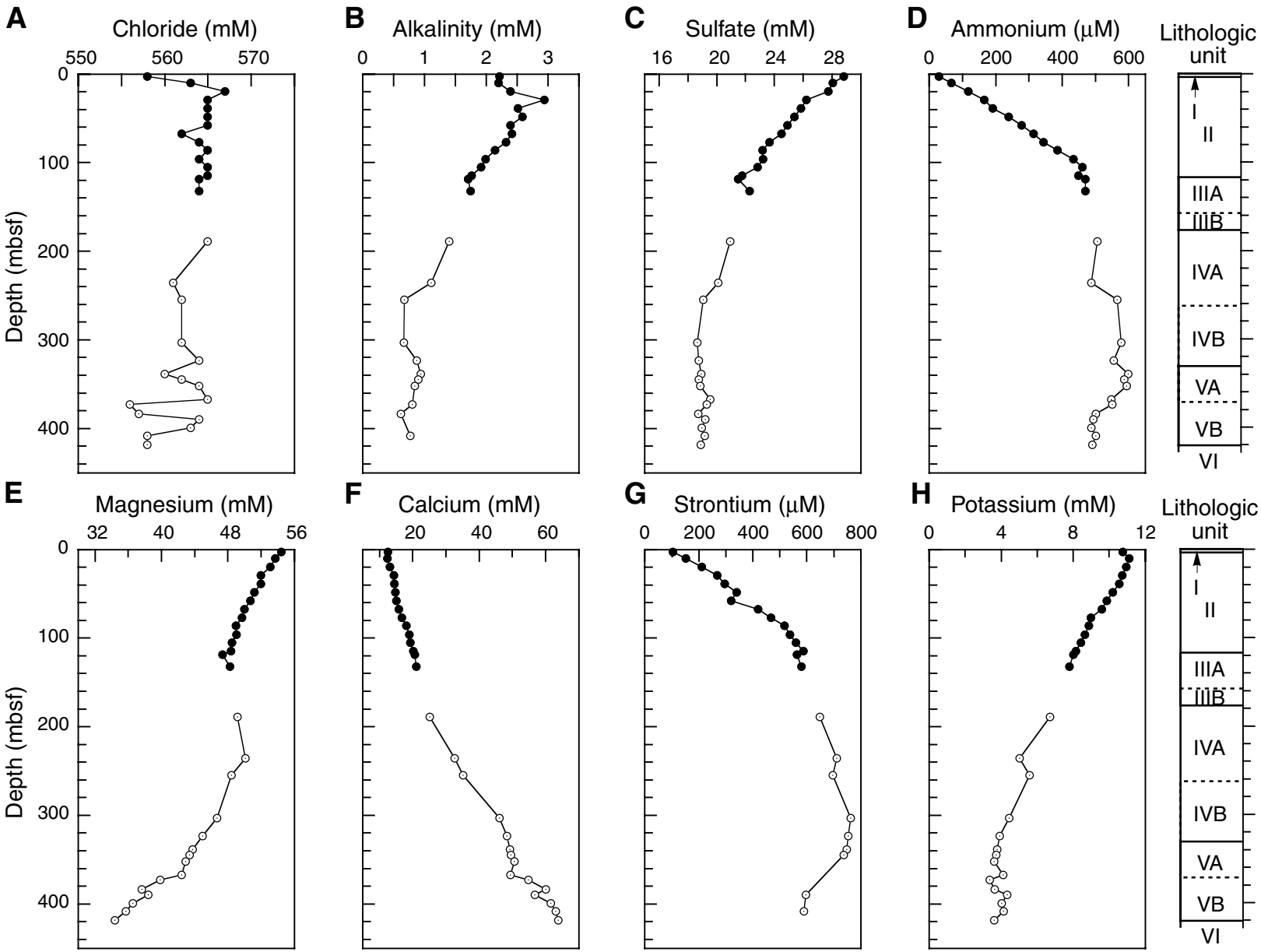

Figure F33. Dissolved magnesium vs. calcium for pore waters of Site 1194. Solid red circles = Hole 1194A, open blue circles = Hole 1194B.

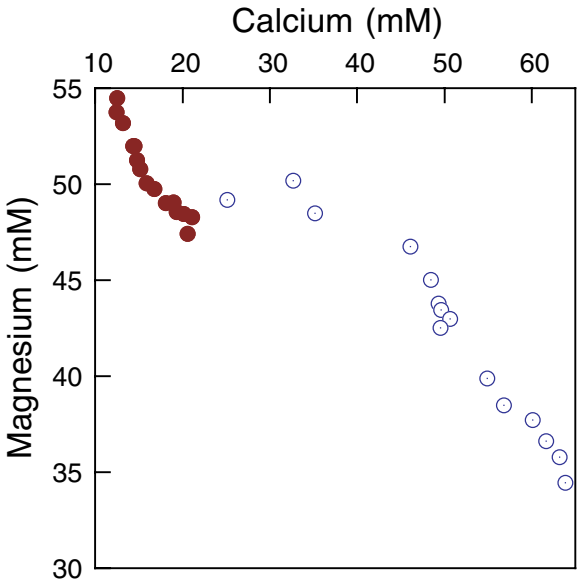

Figure F34. Dissolved magnesium vs. sulfate for pore waters of Hole 1194B. Also shown is the linear trend line with equation and correlation coefficient.

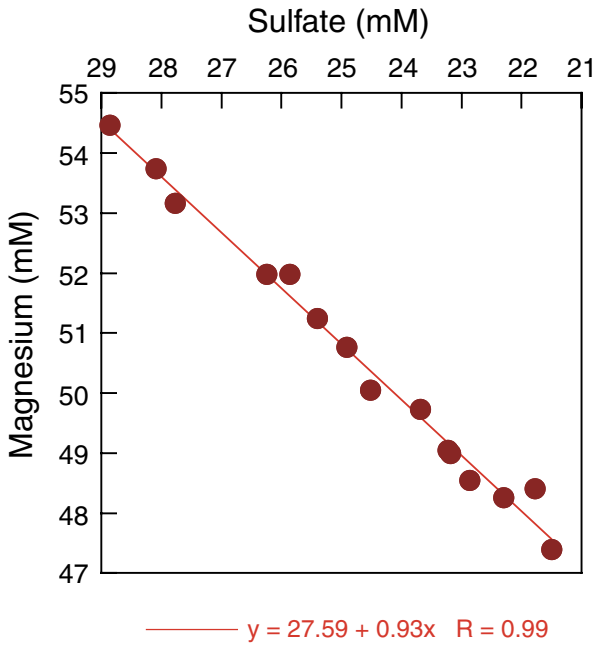

Figure F35. Percentages of dolomite, calcite, and noncarbonate minerals from Site 1194.

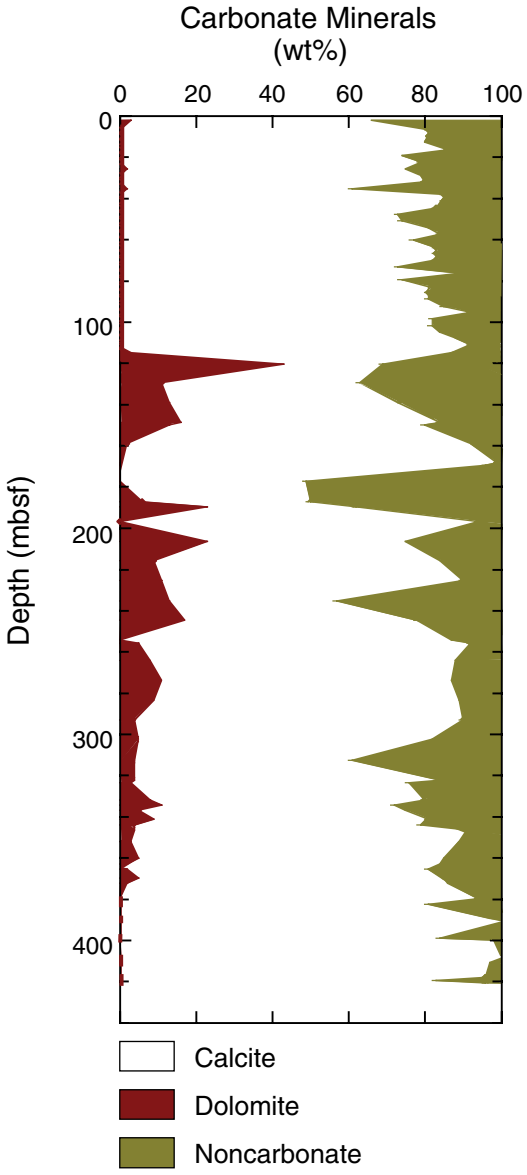

Figure F36. Calcium carbonate and total organic carbon content, hydrogen index, total sulfur content, and C/N and C/S ratios at Site 1194. The dashed vertical lines at hydrogen index = 150, C/N = 25, and C/S = 2 mark the approximate boundary between terrigenous (<150) and marine organic matter, the terrigenous organic matter field (~25–35), and the transition between marine and brackish environments of formation, respectively.

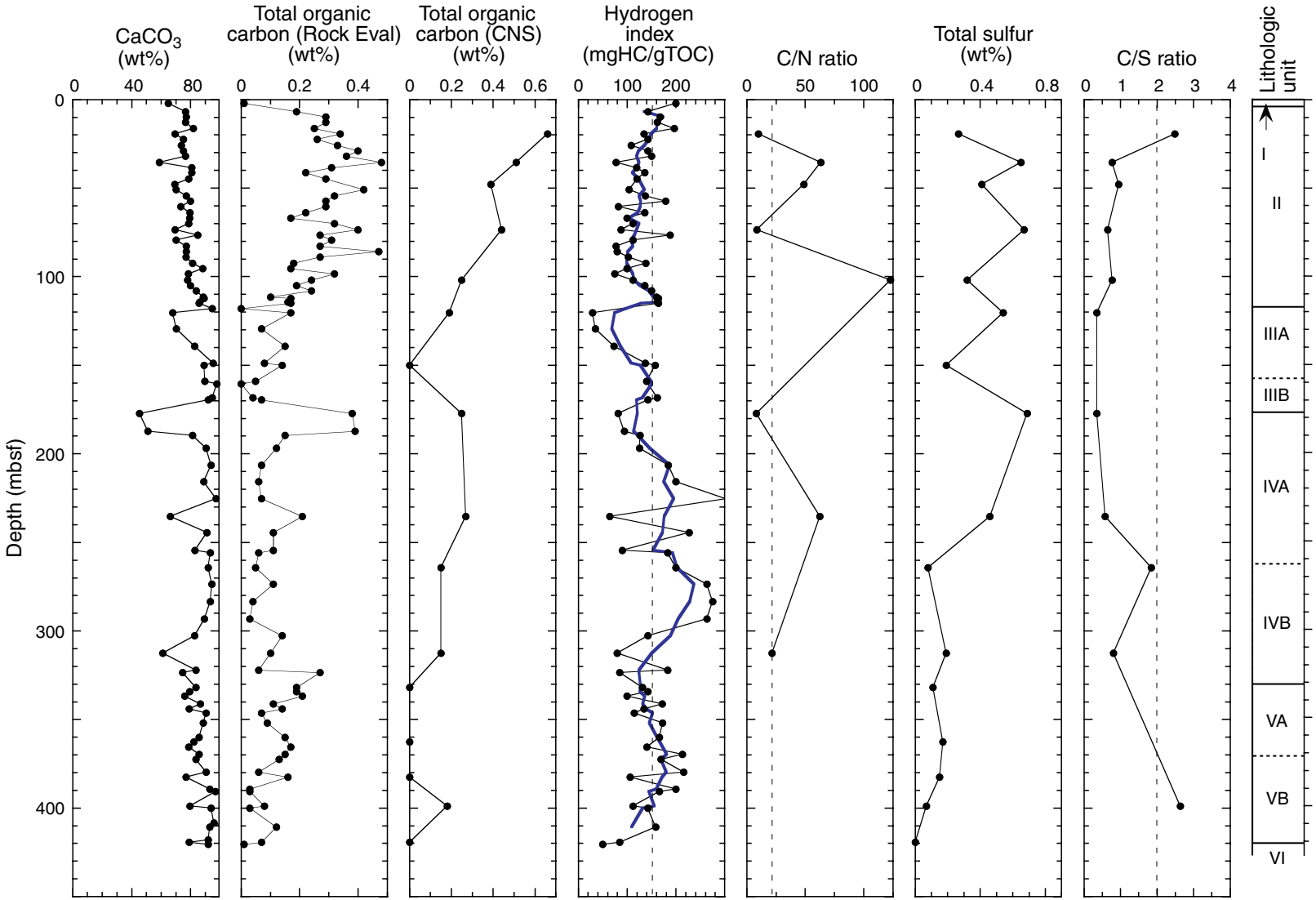

Figure F37. A. Bulk density. Solid circles = Hole 1194A GRA bulk density, squares = Hole 1194B GRA bulk density, open circles = Hole 1194A MAD bulk density, squares = Hole 1194B MAD bulk density. **B.** Grain density from MAD data. **C.** Porosity determined from MAD data (circles and squares) and modeled with an exponential porosity-depth model (line). Circles = data from Hole 1194A, squares = data from Hole 1194B.

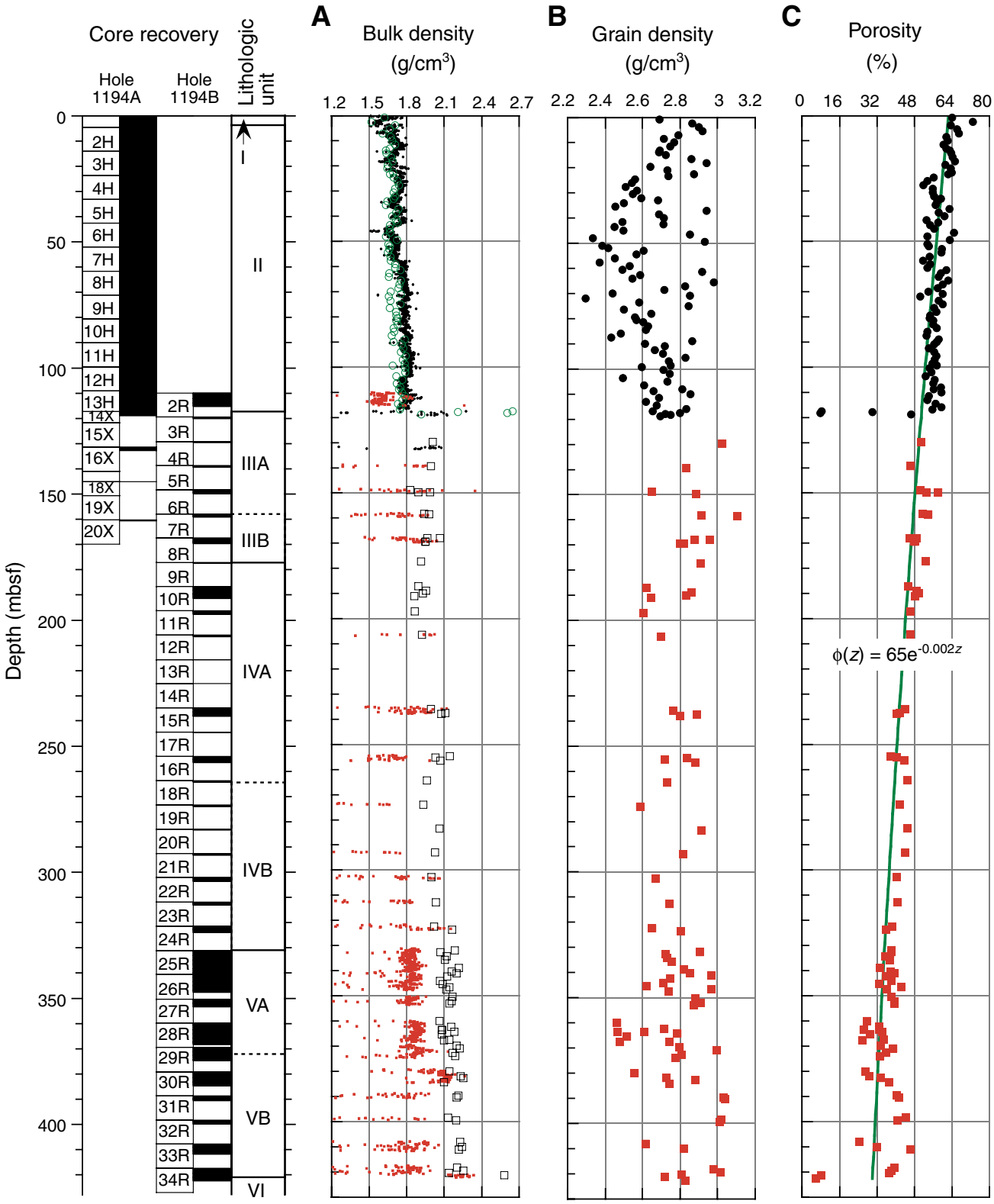

Figure F38. A. Compressional wave velocity as a function of depth. **B.** Adjusted velocity as a function of depth. Circles = x-direction, squares = y-direction, diamonds = z-direction. **C.** Anisotropy (average transverse velocity to longitudinal velocity) of compressional wave velocity.

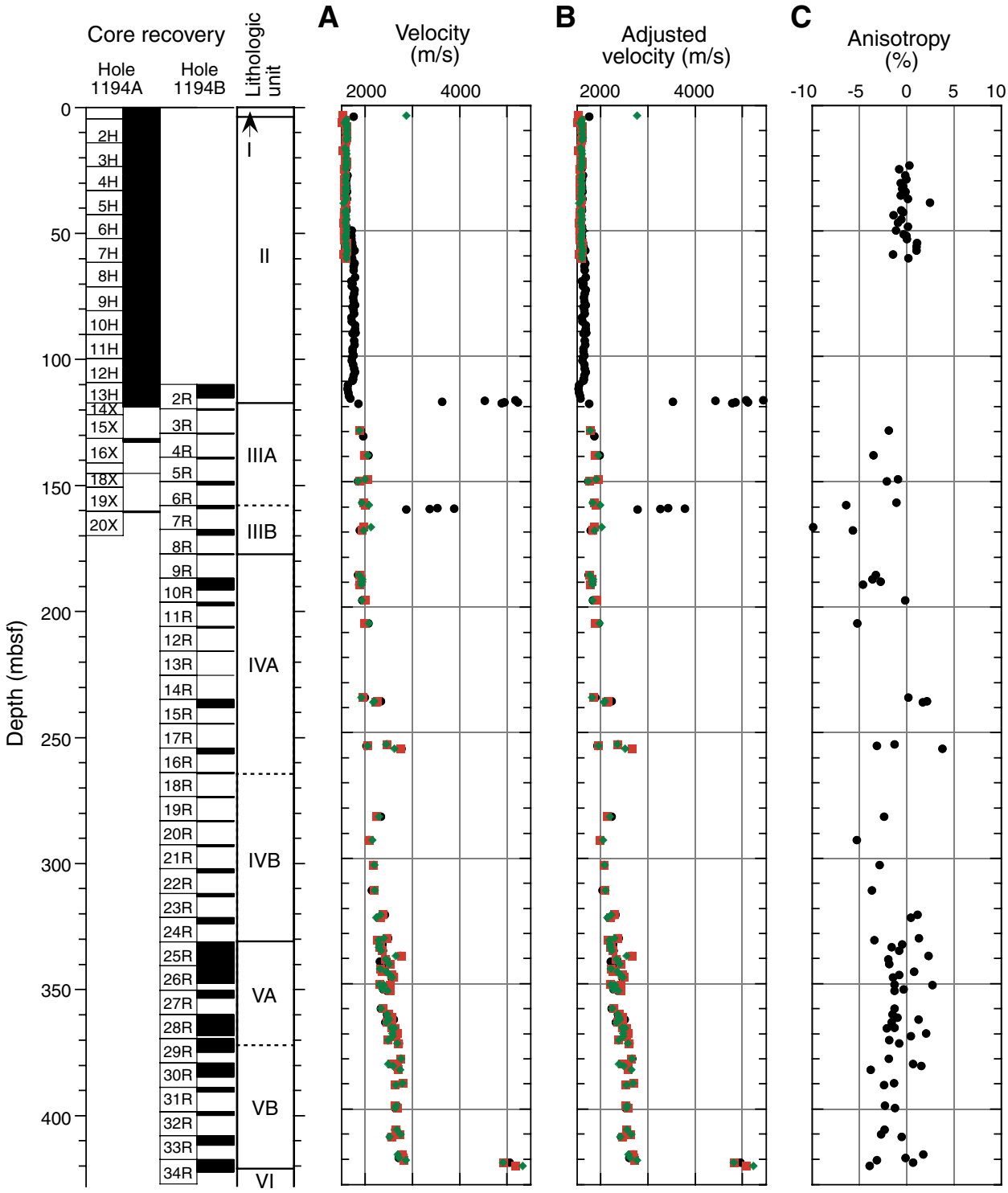

Figure F39. Velocity-porosity crossplot. Circles = observations. Solid line = power law porosity-velocity model. Dashed line = time-average equation for calcite.

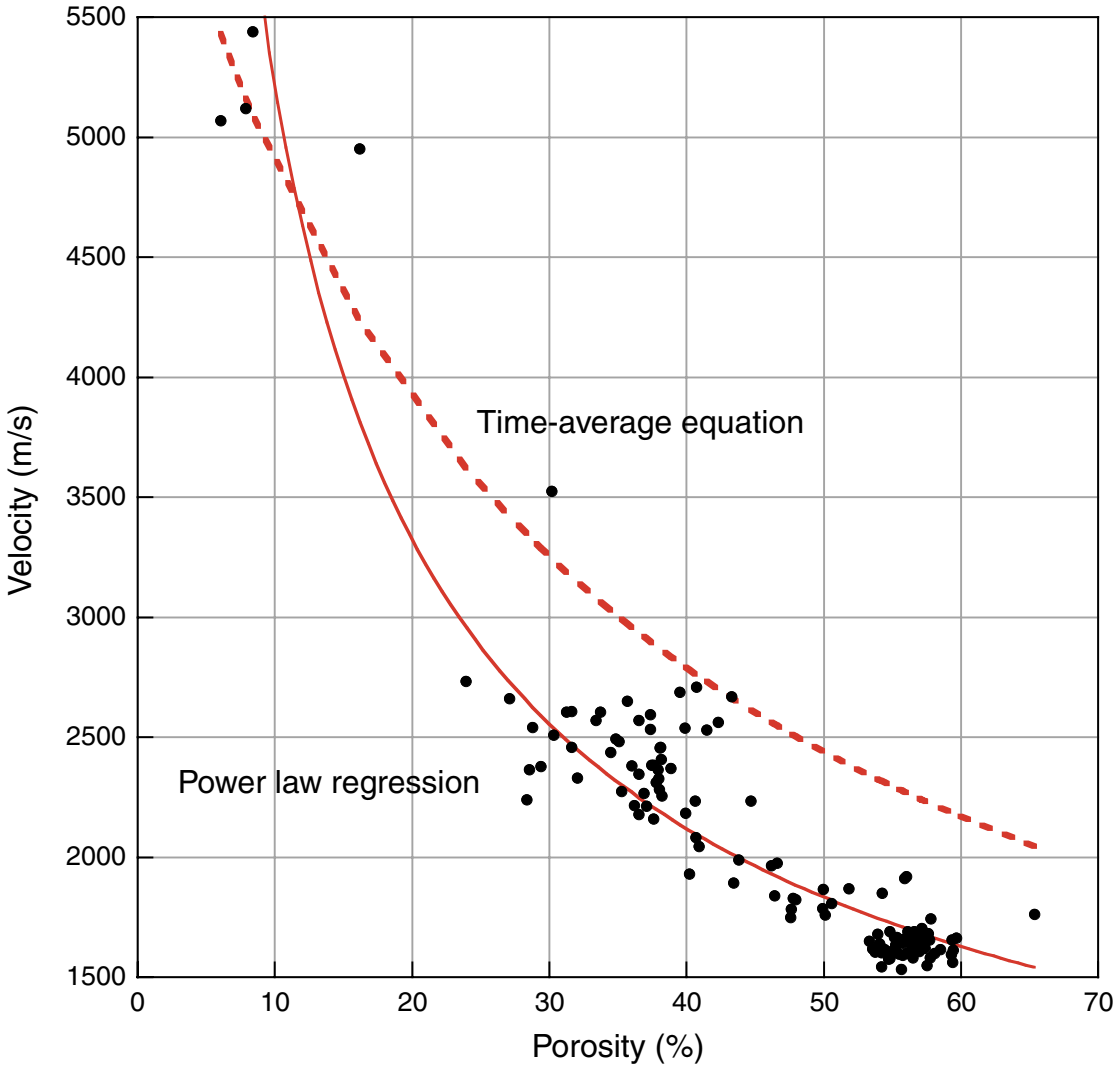

Figure F40. APCT observations (circles) and temperature decay models (curve-fit lines) for (**A**) Core 194-1194A-7H, (**B**) Core 194-1194A-10H, and (**C**) Core 194-1194A-13H. Solid horizontal lines = predicted equilibrium temperature, dashed horizontal lines = error of equilibrium temperature. Ten seconds separate each record number.

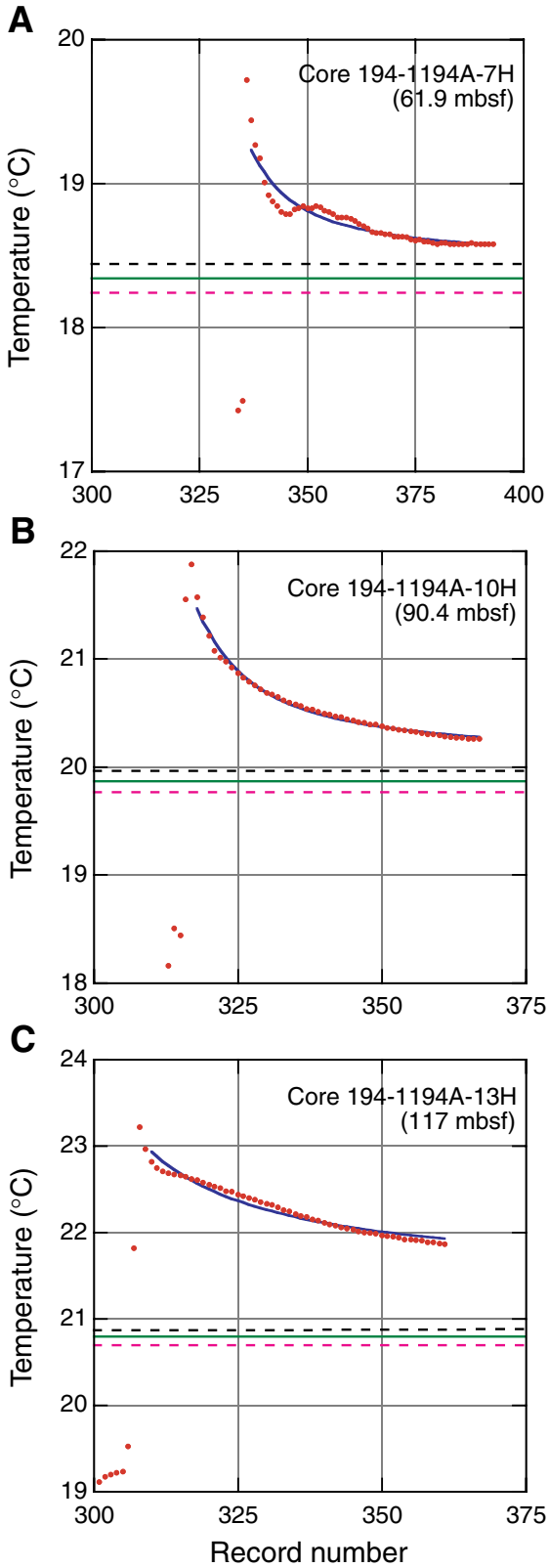

Figure F41. A. Thermal conductivity (W/[m·K]) at Site 1194. Circles = Hole 1194A, squares = Hole 1194B. Plotted values are averages of three needle-probe measurements or four half-space probe measurements. **B.** Downhole temperature observations and linear, least-squares fit of data (solid line).

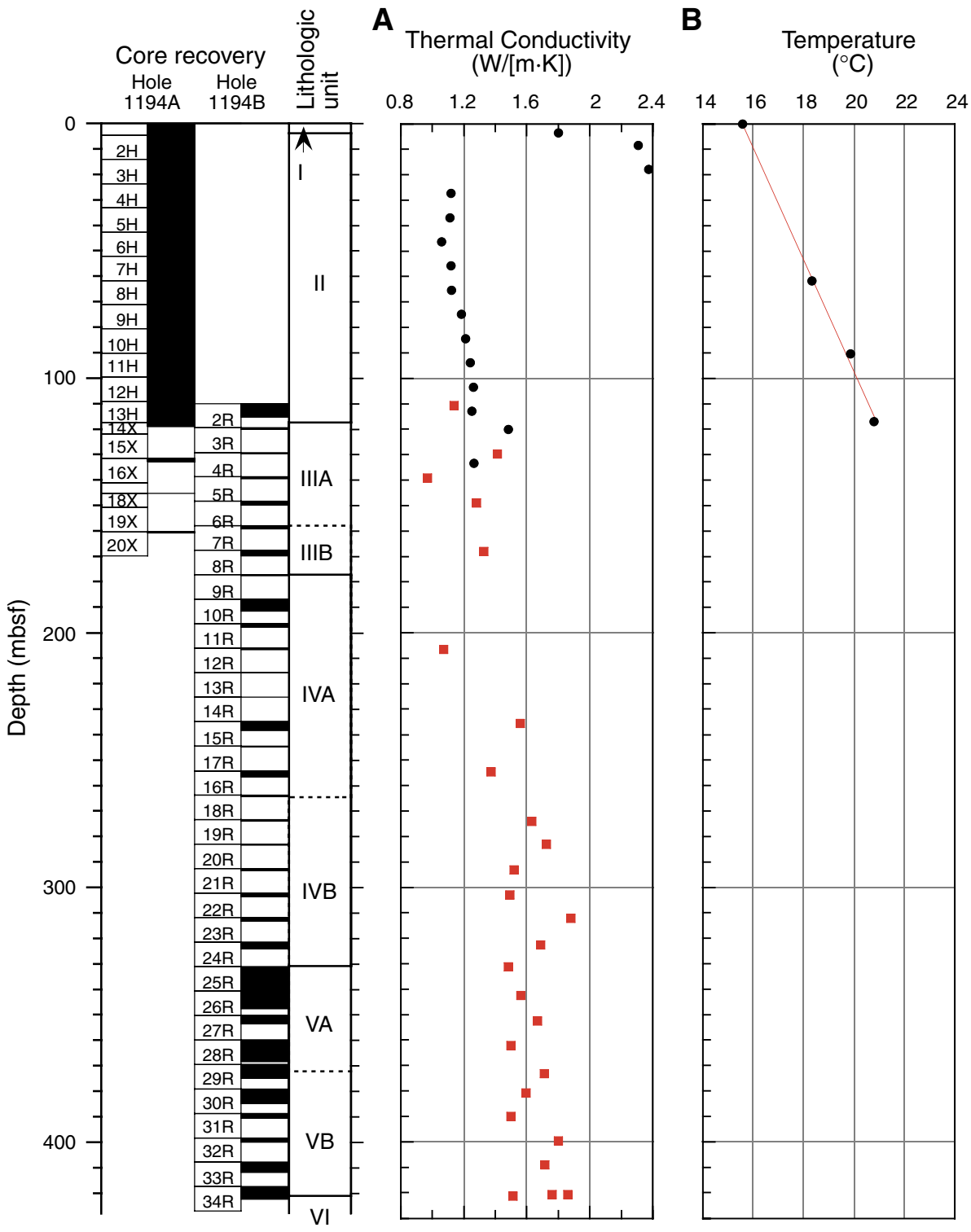

Figure F42. Thermal conductivity as a function of porosity (circles). Curves = theoretical values for pure, single-lithology systems (sandstone, limestone, and shale).

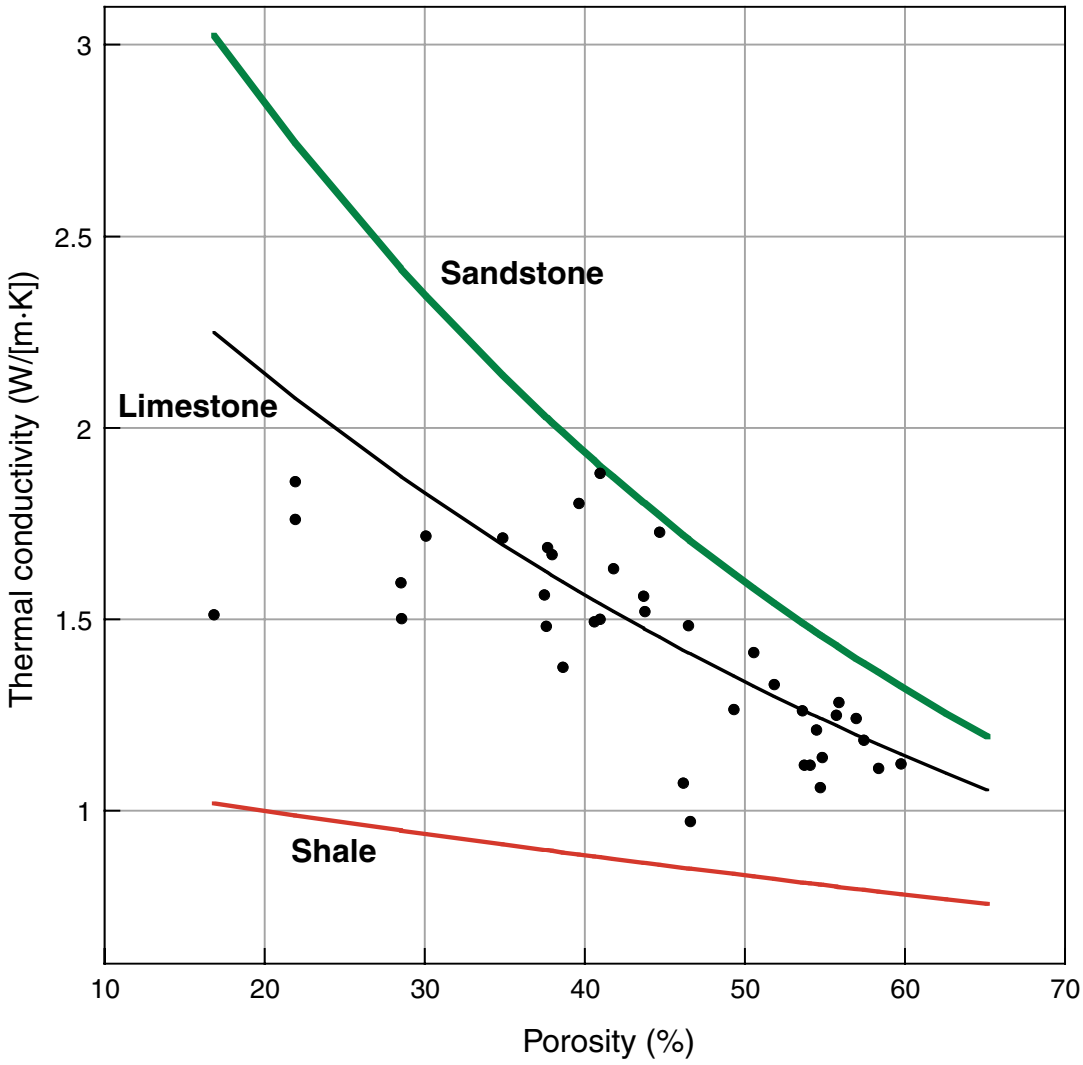

Figure F43. **A.** Magnetic susceptibility (MS). **B.** Natural gamma radiation (NGR). Circles = Hole 1194A, squares = Hole 1194B.

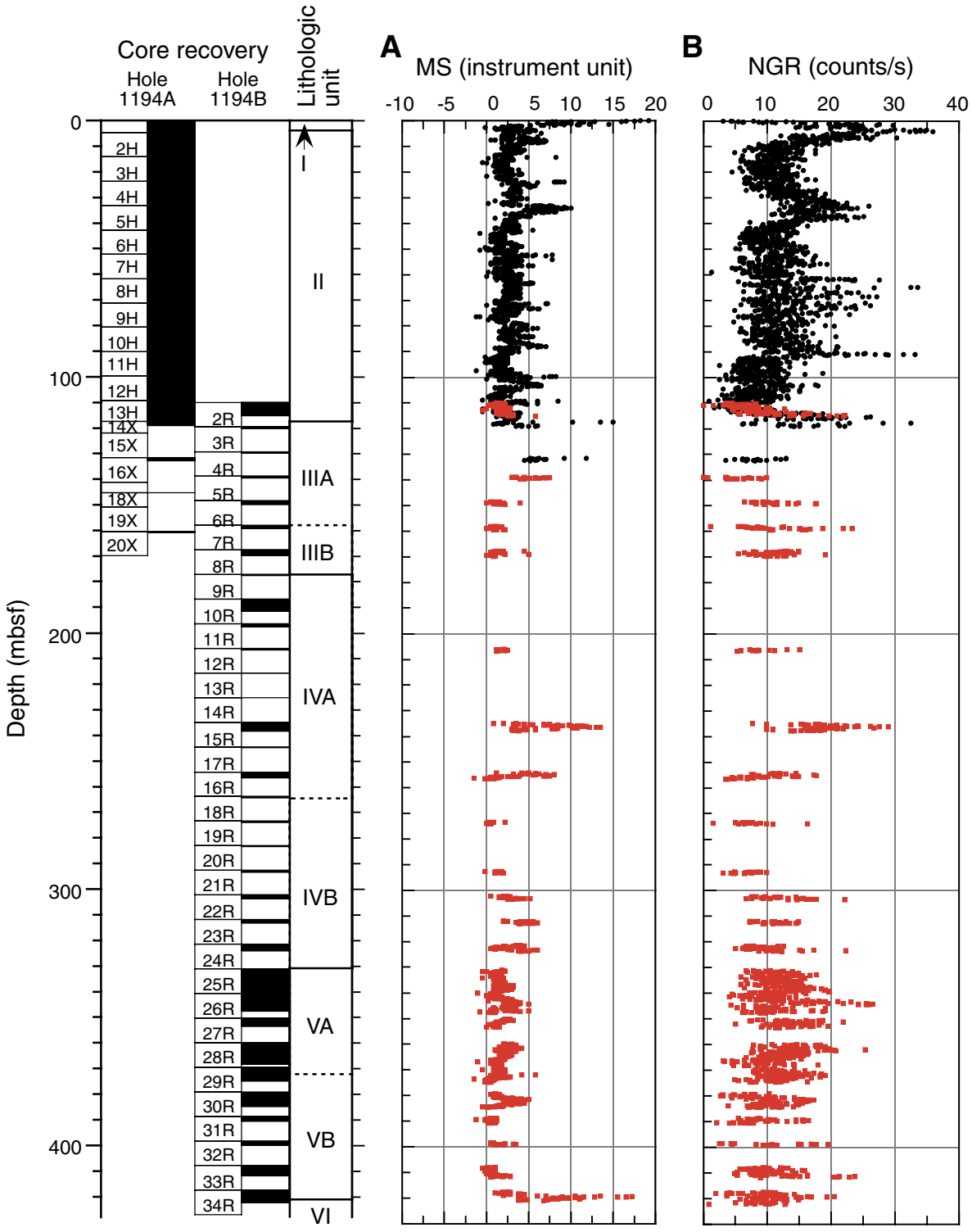

Figure F44. **A.** Smoothed (10-point moving average) magnetic susceptibility (MS) (solid line) and natural gamma radiation (NGR) (dashed line). **B.** Lightness from 0 to 120 mbsf.

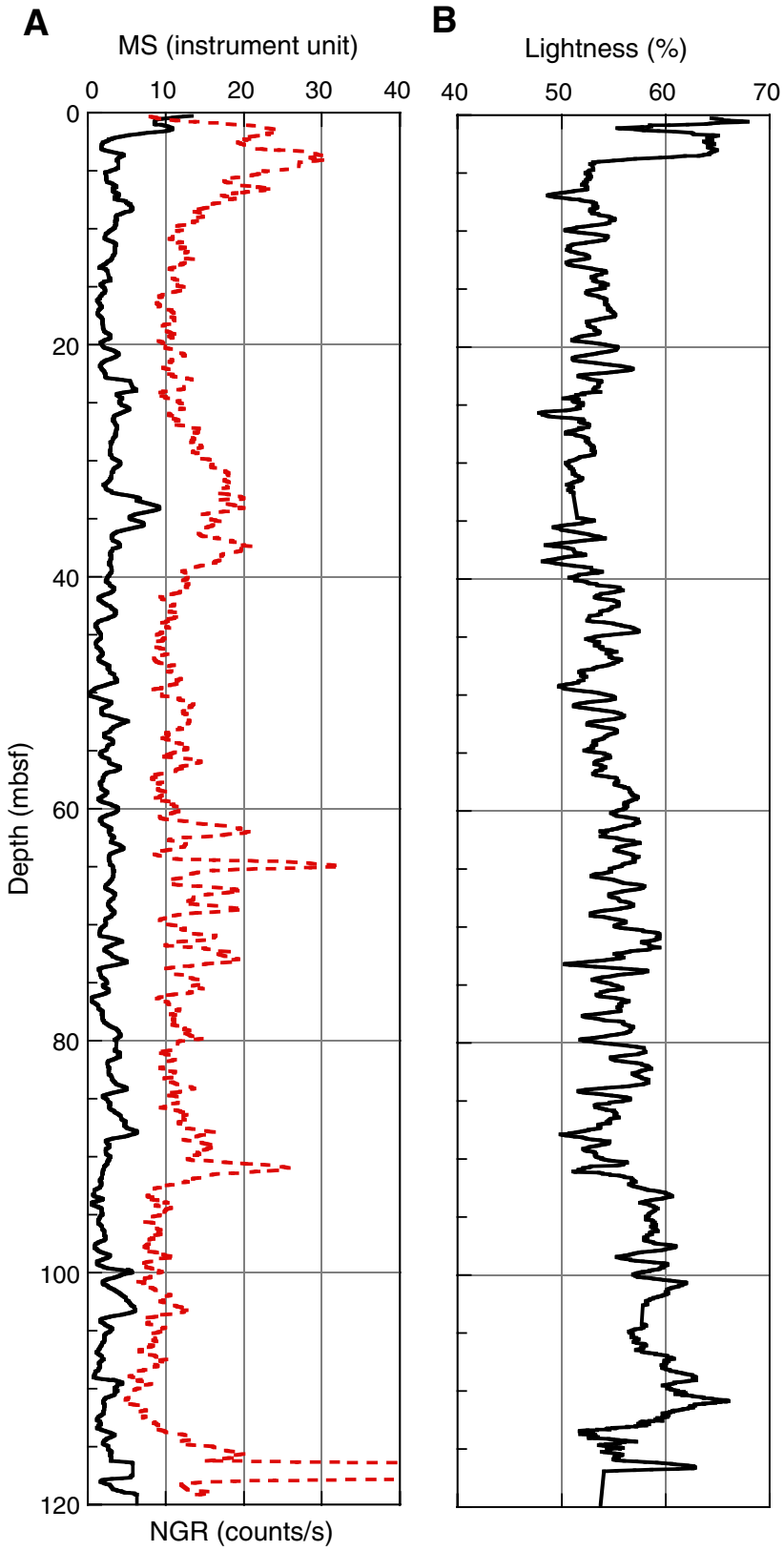

Figure F45. Composite log for Hole 1194B. Borehole width is measured with one arm during the first run (left column) and during the second and third run in two perpendicular directions, C1 and C2.

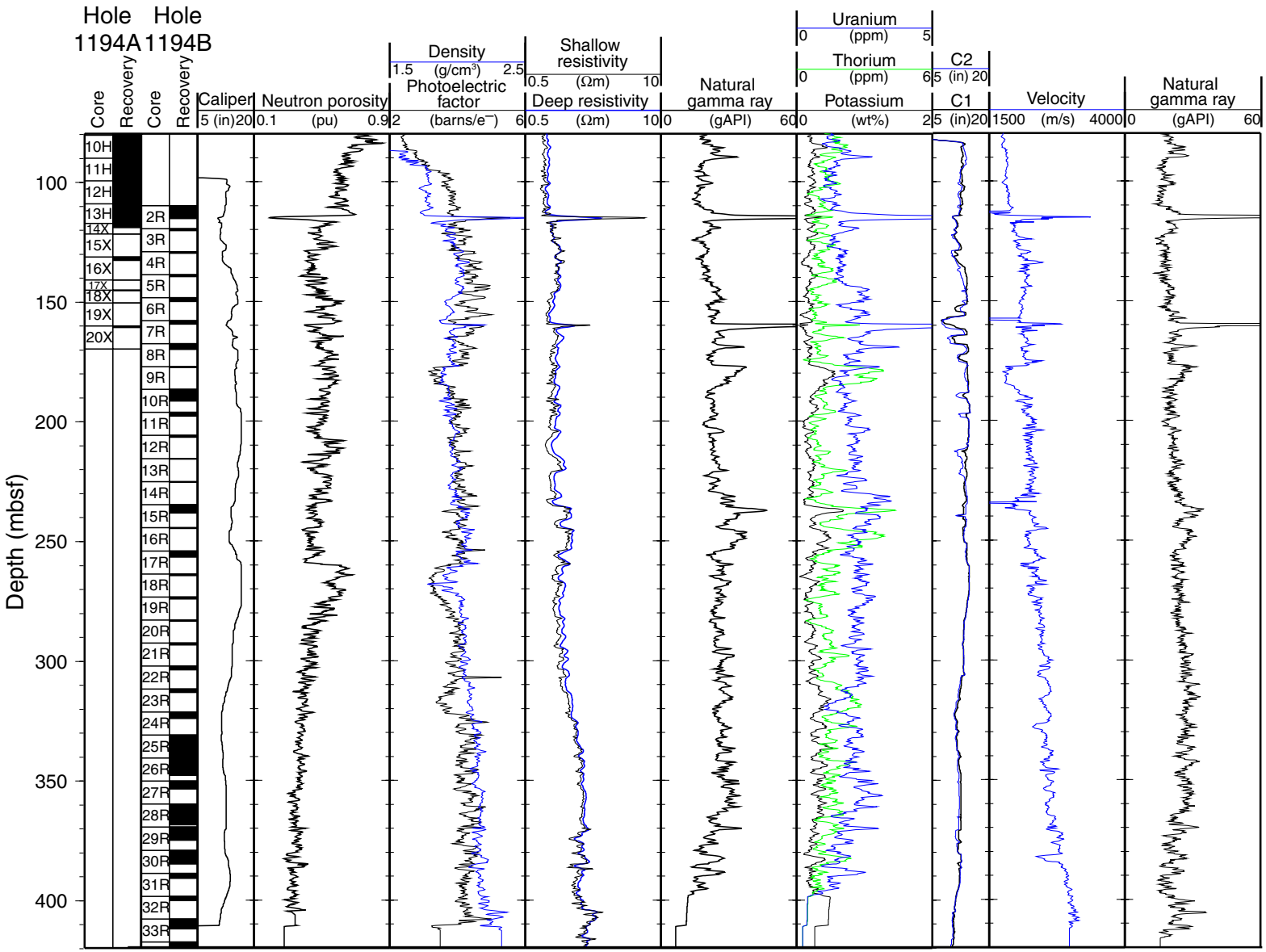

Figure F46. Data produced by the HSGR tool (heavy red line) and the multisensor gamma ray tool (MGT) (fine blue line) show a slight shift between the two curves but an excellent correlation in the trend. Note the high resolution of the MGT. HNGS = spectral gamma ray.

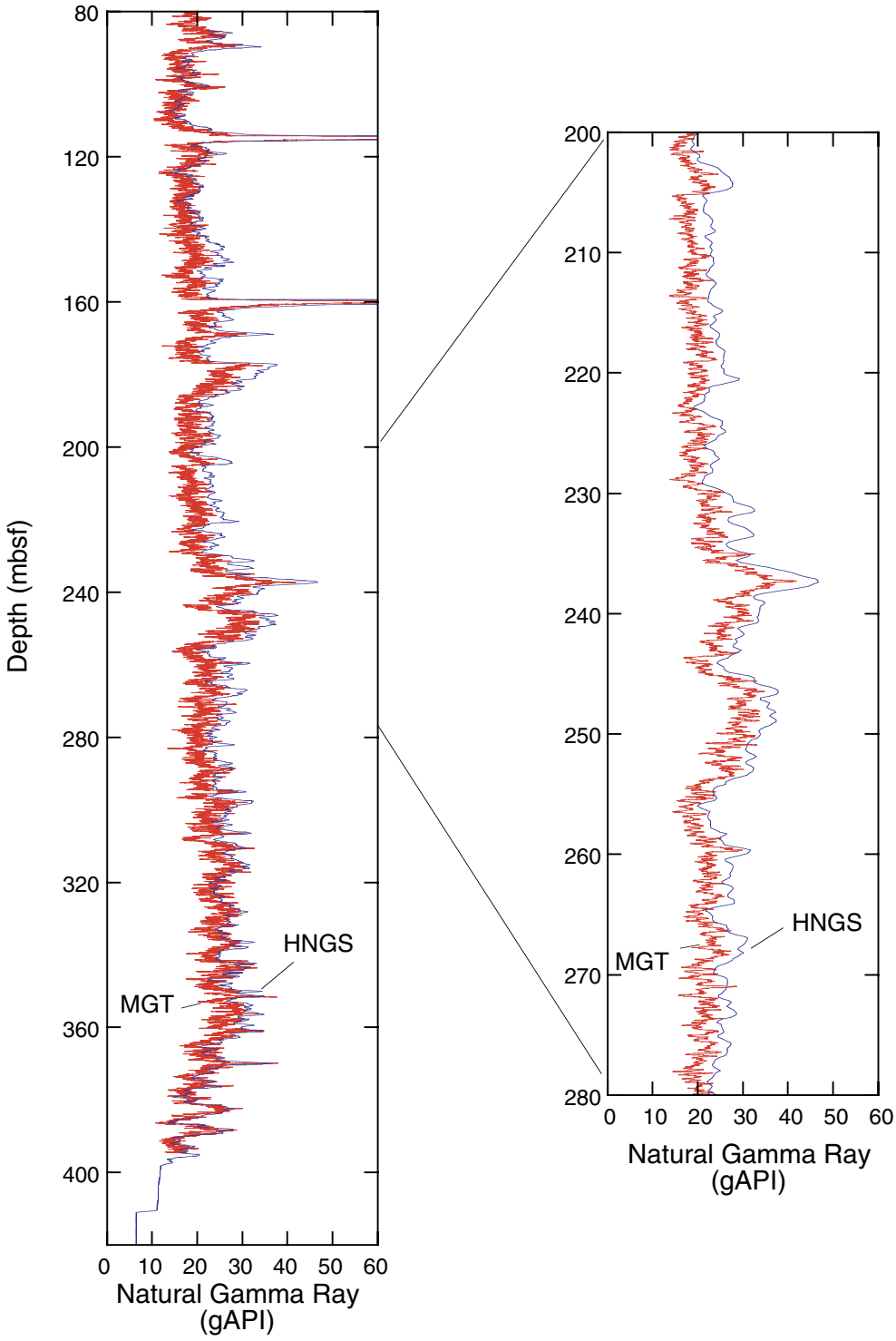

Figure F47. Correlation between the gamma ray values measured downhole (solid line) with the natural gamma ray values of the multisensor gamma ray tool (MST) (dashed line). Vertical lines in the MST values indicate missing core recovery. Although the cores were not shifted, several peaks and troughs can be correlated visually (thin black lines). MGT = multisensor gamma ray tool.

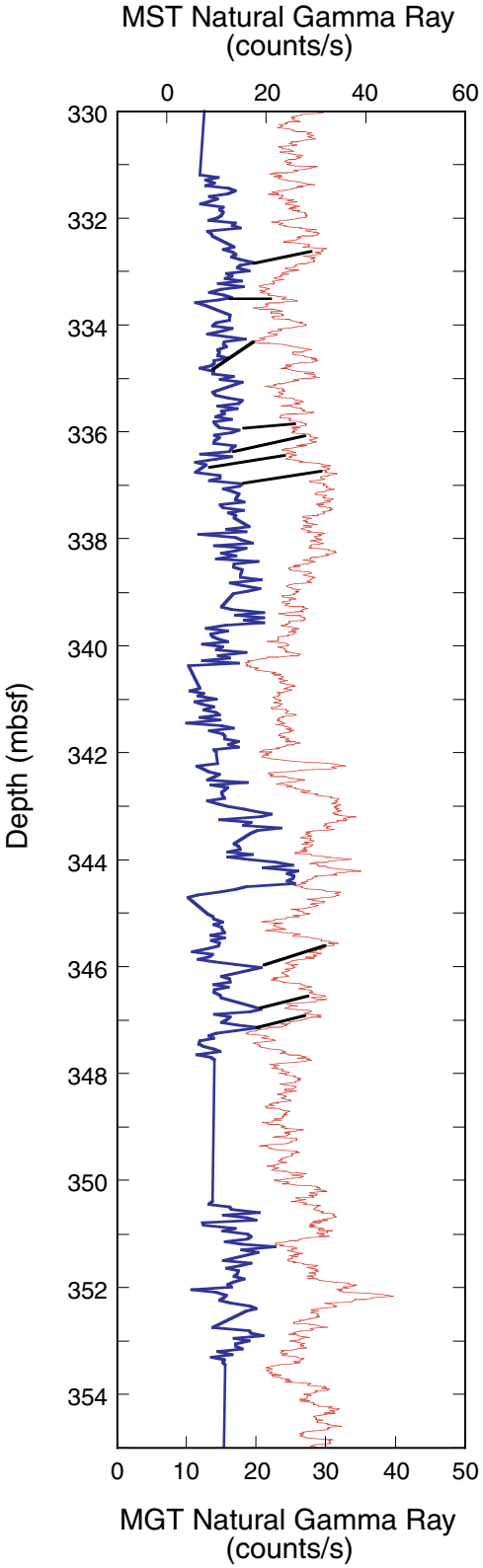

Figure F48. Comparison of core and log physical properties measured at Site 1194. With the exception of the density measured by the multisensor track (MST), there is an overall good correlation. Note the increased amplitude of some of the laboratory data. Solid lines = logs, solid squares = laboratory measurements. MGT = multisensor natural gamma ray tool, MAD = moisture and density.

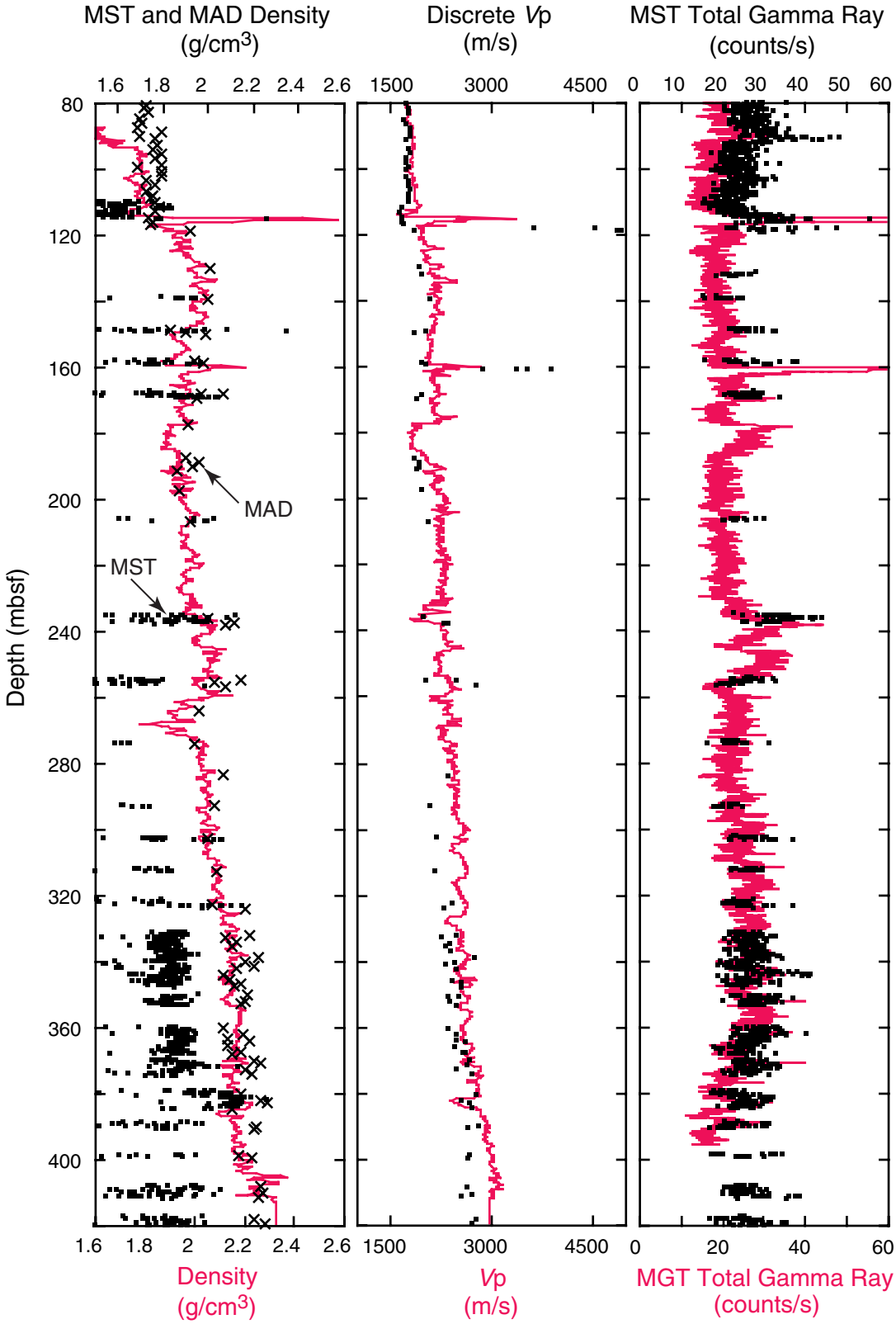

Figure F49. Comparison of lithologic units, log units, and position of changing log signatures in the natural gamma ray and velocity logs. Most lithologic unit boundaries coincide with log unit boundaries and changes in log signatures. In the low recovery interval of lithologic Subunit IVA, the logs indicate further subdivisions. Solid purple lines = positions of the three log unit boundaries, dashed purple lines = positions of log changes within the units.

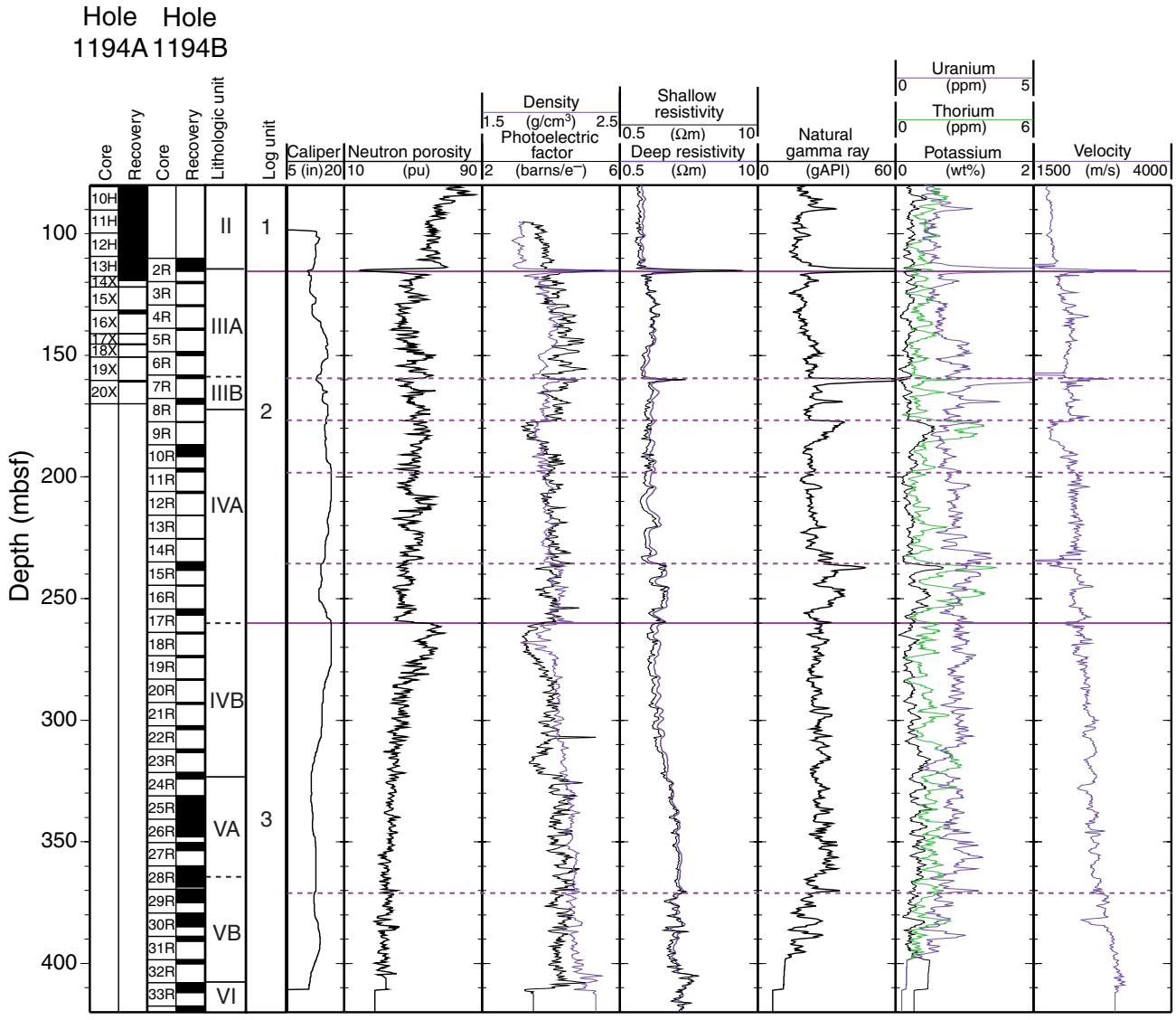

Figure F50. Dynamic and static Formation MicroScanner (FMS) images and NGR logs across a recovered and an inferred hardground in logging Unit 2. **A.** The recovered hardground bed at 114.5 mbsf is capped by a phosphatic crust that is probably responsible for the sharp peak in uranium. The thin densely cemented bed is highly resistive with a sharp upper boundary. **B.** The inferred hardground bed with a top at 159.5 mbsf also shows a peak in uranium and an increase in resistivity.

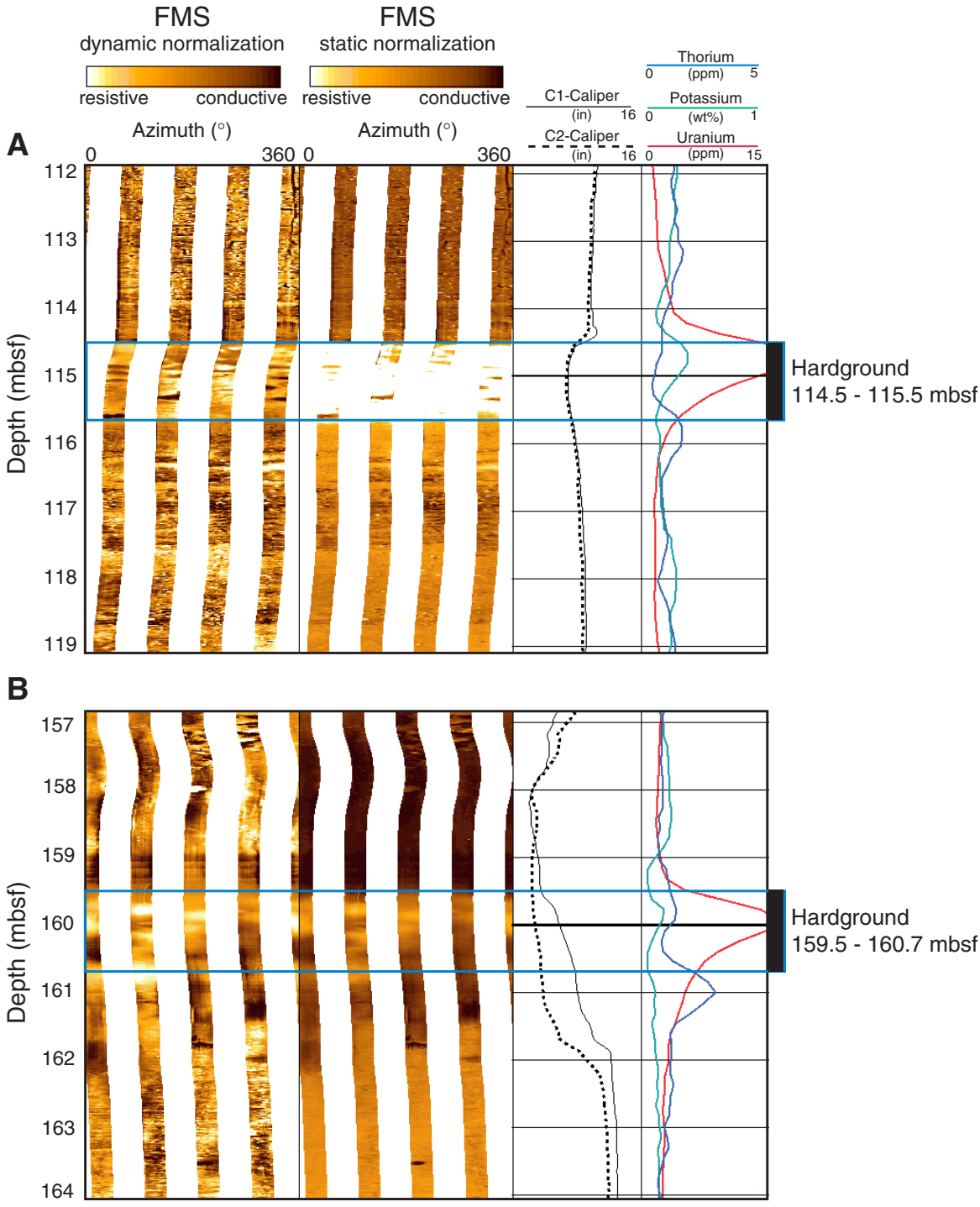

Figure F51. Dynamic and static Formation MicroScanner (FMS) image and NGR logs across the lithologic Unit III/IV boundary that was placed at a 1-cm-thick layer of grainstone with a sharp contact at 177 mbsf. This boundary coincides with a thin highly resistive layer capping a lower resistive bed on the FMS log. The layer also marks the change in bedding character from thin-bedded and highly resistive strata below to thick-bedded and more conductive strata above.

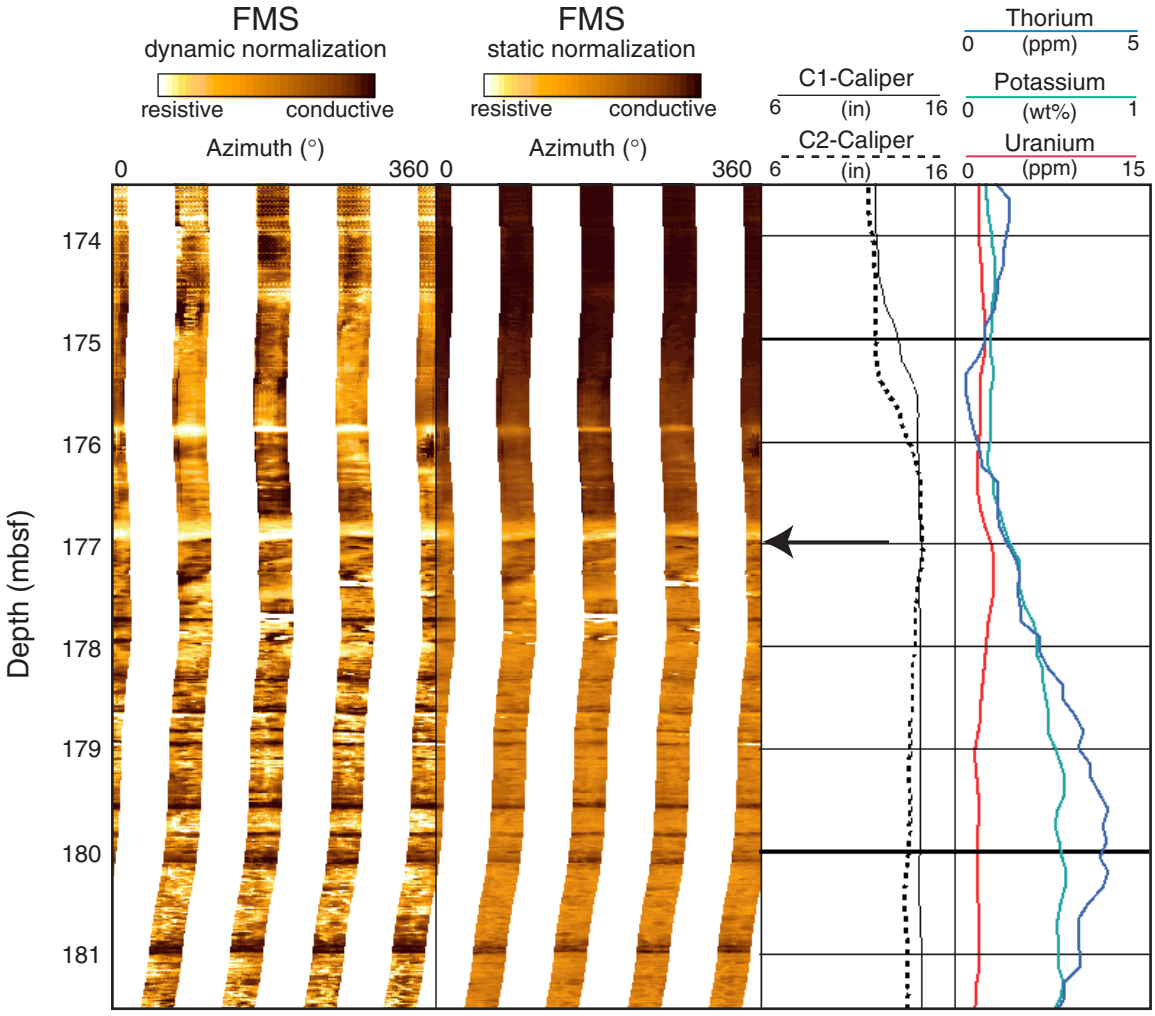

Figure F52. Dynamic and static Formation MicroScanner (FMS) images of the basement and the overlying sediments. **A.** The FMS image displays the resistivity cycles in the lower part of the hole that are interpreted as alternations of thin-bedded clayey limestones overlain by heavily bioturbated limestones. **B.** The highly resistive volcanic basement is dipping with a steep angle of ~70° and is overlain by strata that produce a mottled to layered FMS image.

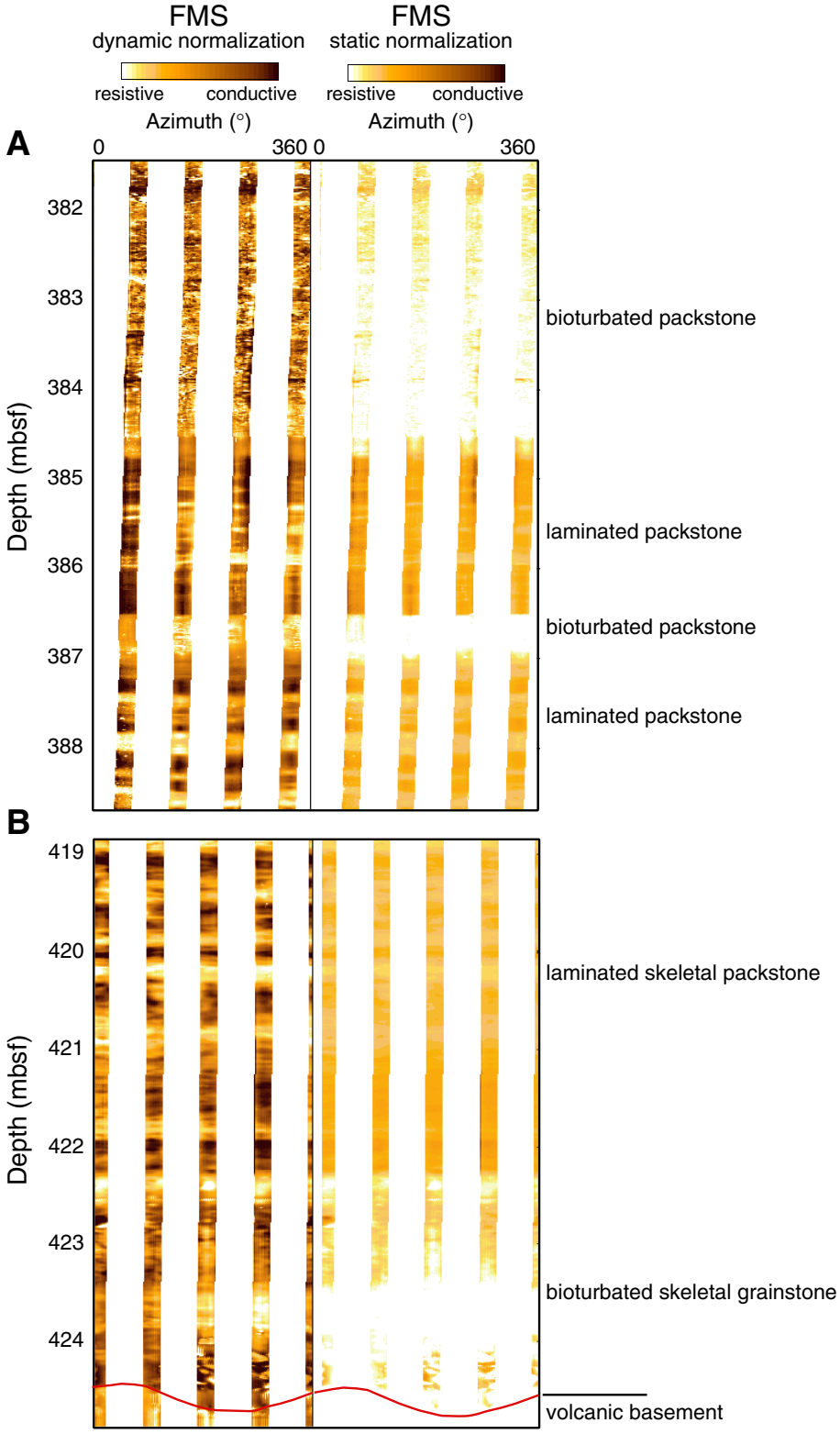

Figure F53. Temperature vs. depth. Arrows indicate the upgoing and downgoing measurements.

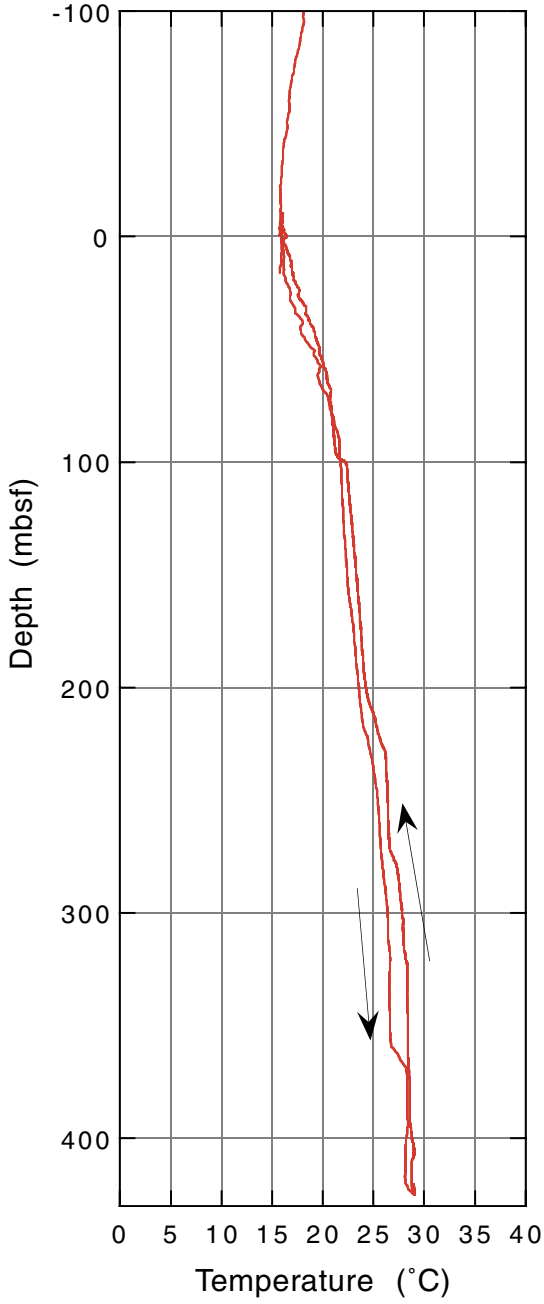

Figure F54. Multichannel line MAR13 with location and penetration depth of Site 1194 located at SP 3955. The seismic megasequences and the basement are marked and traced along the section. The arrow points toward a high-amplitude reflection that can be mapped within Megasequence B. MS = Megasequence.

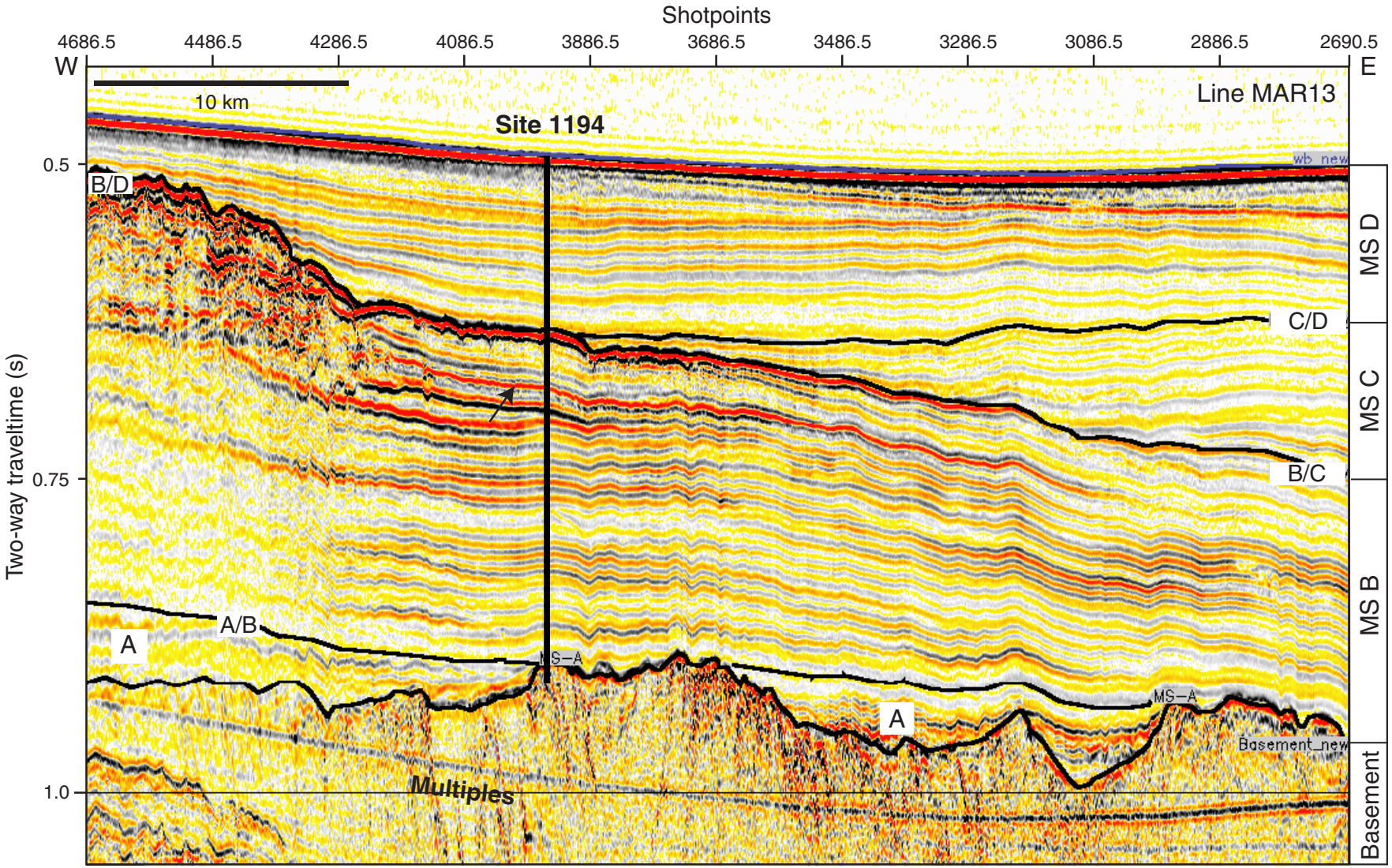

Figure F55. Synthetic seismogram plotted on line MAR13 with two-way traveltime-to-depth velocity data (m/s), *P*-wave velocity with superimposed GRA bulk density, synthetic seismogram, megasequence boundaries, and lithologic units. The traveltime-vs.-depth plot (left) was used to correlate seismic reflections to their depth in the sedimentary section.

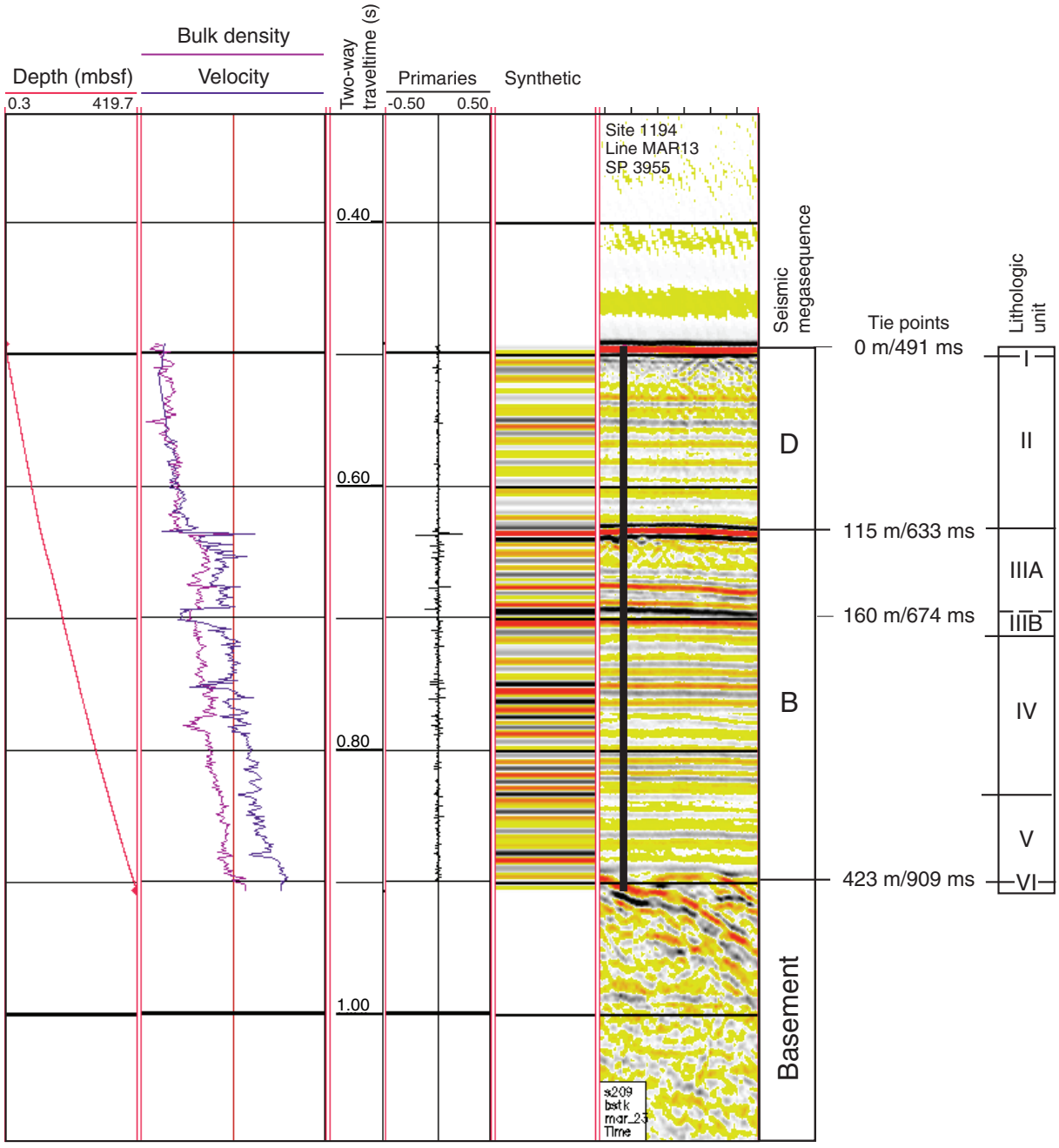

Table T1. Coring summary, Site 1194.

Core	Date (Jan 2001)	Time (local)	Depth (mbsf) Top	Depth (mbsf) Bottom	Length (m) Cored	Length (m) Recovered	Recovery (%)
194-1194A-							
1H	23	0355	0.0	4.7	4.7	4.67	99.4
2H	23	0435	4.7	14.2	9.5	9.72	102.3
3H	23	0500	14.2	23.7	9.5	9.61	101.2
4H	23	0550	23.7	33.2	9.5	10.13	106.6
5H	23	0620	33.2	42.7	9.5	9.95	104.7
6H	23	0645	42.7	52.2	9.5	9.92	104.4
7H	23	0740	52.2	61.7	9.5	10.00	105.3
8H	23	0815	61.7	71.2	9.5	9.96	104.8
9H	23	0845	71.2	80.7	9.5	9.66	101.7
10H	23	0935	80.7	90.2	9.5	10.17	107.1
11H	23	1005	90.2	99.7	9.5	10.05	105.8
12H	23	1035	99.7	109.2	9.5	10.13	106.6
13H	23	1135	109.2	117.4	8.2	8.20	100.0
14X	23	1315	117.4	121.9	4.5	1.78	39.6
15X	23	1355	121.9	131.5	9.6	0.00	0.0
16X	23	1425	131.5	141.1	9.6	1.43	14.9
17X	23	1610	141.1	145.3	4.2	0.00	0.0
18X	23	1730	145.3	150.7	5.4	0.19	3.5
19X	23	1815	150.7	160.3	9.6	0.00	0.0
20X	23	1935	160.3	169.9	9.6	0.61	6.4
				Cored total:	169.9	126.18	74.3
				Drilled total:	0.0		
				Total:	169.9		
194-1194B-							
1W	24	0445	0.0	110.0	110.0	0.00	0.0
2R	24	0525	110.0	119.6	9.6	5.44	56.7
3R	24	0550	119.6	129.3	9.7	0.79	8.1
4R	24	0615	129.3	138.8	9.5	0.59	6.2
5R	24	0635	138.8	148.4	9.6	0.86	9.0
6R	24	0655	148.4	158.0	9.6	1.69	17.6
7R	24	0720	158.0	167.6	9.6	1.44	15.0
8R	24	0740	167.6	177.2	9.6	2.36	24.6
9R	24	0815	177.2	186.8	9.6	0.41	4.3
10R	24	0845	186.8	196.4	9.6	4.80	50.0
11R	24	0910	196.4	206.0	9.6	1.54	16.0
12R	24	0940	206.0	215.7	9.7	0.76	7.8
13R	24	1000	215.7	225.3	9.6	0.21	2.2
14R	24	1025	225.3	234.9	9.6	0.18	1.9
15R	24	1100	234.9	244.5	9.6	3.50	36.5
16R	24	1130	244.5	254.2	9.7	0.36	3.7
17R	24	1210	254.2	263.8	9.6	2.57	26.8
18R	24	1235	263.8	273.4	9.6	0.73	7.6
19R	24	1300	273.4	283.0	9.6	0.79	8.2
20R	24	1325	283.0	292.6	9.6	0.59	6.1
21R	24	1355	292.6	302.2	9.6	0.81	8.4
22R	24	1425	302.2	311.9	9.7	1.69	17.4
23R	24	1455	311.9	321.5	9.6	1.41	14.7
24R	24	1535	321.5	331.1	9.6	2.65	27.6
25R	24	1615	331.1	340.7	9.6	9.52	99.2
26R	24	1700	340.7	350.3	9.6	7.19	74.9
27R	24	1745	350.3	359.9	9.6	3.34	34.8
28R	24	1845	359.9	369.5	9.6	8.61	89.7
29R	24	1935	369.5	379.2	9.7	5.56	57.3
30R	24	2025	379.2	388.8	9.6	5.73	59.7
31R	24	2125	388.8	398.4	9.6	2.05	21.4
32R	24	2215	398.4	407.9	9.5	1.78	18.7
33R	24	2320	407.9	417.5	9.6	4.14	43.1
34R	25	0030	417.5	427.1	9.6	5.13	53.4
				Cored total:	427.1	89.22	20.9
				Drilled total:	0.0		
				Total:	427.1		

Table T2. Expanded coring summary, Site 1194. (See table notes. Continued on next four pages.)

Core	Date (Jan 2001)	Time (local)	Core depth (mbsf) Top	Core depth (mbsf) Bottom	Length (m) Cored	Length (m) Recovered	Recovery (%)	Section	Length (m) Liner	Length (m) Curated	Section depth (mbsf) Top	Section depth (mbsf) Bottom	Catwalk samples	Comment
194-1194A-														
1H	23	0355	0.0	4.7	4.7	4.67	99.4							
								1	1.50	1.50	0.00	1.50		
								2	1.50	1.50	1.50	3.00	HS, IW	
								3	1.38	1.38	3.00	4.38		
								CC (w/CC)	0.29	0.29	4.38	4.67	PAL	
								Totals:	4.67	4.67				
2H	23	0435	4.7	14.2	9.5	9.72	102.3							
								1	1.50	1.50	4.70	6.20		
								2	1.50	1.50	6.20	7.70		
								3	1.50	1.50	7.70	9.20		
								4	1.50	1.50	9.20	10.70	IW	
								5	1.50	1.50	10.70	12.20	HS	
								6	1.50	1.50	12.20	13.70		
								7	0.44	0.44	13.70	14.14		
								CC (w/7)	0.28	0.28	14.14	14.42	PAL	
								Totals:	9.72	9.72				
3H	23	0500	14.2	23.7	9.5	9.61	101.2							
								1	1.50	1.50	14.20	15.70		
								2	1.50	1.50	15.70	17.20		
								3	1.50	1.50	17.20	18.70		
								4	1.50	1.50	18.70	20.20	IW	
								5	1.50	1.50	20.20	21.70	HS	
								6	1.50	1.50	21.70	23.20		
								7	0.33	0.33	23.20	23.53		
								CC (w/7)	0.28	0.28	23.53	23.81	PAL	
								Totals:	9.61	9.61				
4H	23	0550	23.7	33.2	9.5	10.13	106.6							
								1	1.50	1.50	23.70	25.20		
								2	1.50	1.50	25.20	26.70		
								3	1.50	1.50	26.70	28.20		
								4	1.50	1.50	28.20	29.70	IW	
								5	1.50	1.50	29.70	31.20	HS	
								6	1.50	1.50	31.20	32.70		
								7	0.79	0.79	32.70	33.49		
								CC (w/7)	0.34	0.34	33.49	33.83	PAL	
								Totals:	10.13	10.13				
5H	23	0620	33.2	42.7	9.5	9.95	104.7							
								1	1.50	1.50	33.20	34.70		
								2	1.50	1.50	34.70	36.20		
								3	1.50	1.50	36.20	37.70	DUGWR	
								4	1.50	1.50	37.70	39.20	IW	
								5	1.50	1.50	39.20	40.70	HS	
								6	1.50	1.50	40.70	42.20		
								7	0.62	0.62	42.20	42.82		
								CC (w/7)	0.33	0.33	42.82	43.15	PAL	
								Totals:	9.95	9.95				
6H	23	0645	42.7	52.2	9.5	9.92	104.4							
								1	1.50	1.50	42.70	44.20		
								2	1.50	1.50	44.20	45.70		
								3	1.50	1.50	45.70	47.20		
								4	1.50	1.50	47.20	48.70	IW	
								5	1.50	1.50	48.70	50.20	HS	
								6	1.50	1.50	50.20	51.70		
								7	0.59	0.59	51.70	52.29		
								CC (w/7)	0.33	0.33	52.29	52.62	PAL	
								Totals:	9.92	9.92				
7H	23	0740	52.2	61.7	9.5	10.00	105.3							
								1	1.50	1.50	52.20	53.70		
								2	1.50	1.50	53.70	55.20		
								3	1.50	1.50	55.20	56.70		
								4	1.50	1.50	56.70	58.20	IW	
								5	1.50	1.50	58.20	59.70		
								6	1.50	1.50	59.70	61.20		
								7	0.65	0.65	61.20	61.85		
								CC (w/7)	0.35	0.35	61.85	62.20	PAL	
								Totals:	10.00	10.00				

Table T2 (continued).

Core	Date (Jan 2001)	Time (local)	Core depth (mbsf) Top	Core depth (mbsf) Bottom	Length (m) Cored	Length (m) Recovered	Recovery (%)	Section	Length (m) Liner	Length (m) Curated	Section depth (mbsf) Top	Section depth (mbsf) Bottom	Catwalk samples	Comment
8H	23	0815	61.7	71.2	9.5	9.96	104.8							
								1	1.50	1.50	61.70	63.20		
								2	1.50	1.50	63.20	64.70		
								3	1.50	1.50	64.70	66.20	DUGWR	
								4	1.50	1.50	66.20	67.70	IW	
								5	1.50	1.50	67.70	69.20	HS	
								6	1.50	1.50	69.20	70.70		
								7	0.62	0.62	70.70	71.32		
								CC (w/7)	0.34	0.34	71.32	71.66	PAL	
								Totals:	9.96	9.96				
9H	23	0845	71.2	80.7	9.5	9.66	101.7							
								1	1.50	1.50	71.20	72.70		
								2	1.50	1.50	72.70	74.20		
								3	1.50	1.50	74.20	75.70		
								4	1.50	1.50	75.70	77.20	IW	
								5	1.50	1.50	77.20	78.70	HS	
								6	1.50	1.50	78.70	80.20		
								7	0.30	0.30	80.20	80.50		
								CC (w/7)	0.36	0.36	80.50	80.86	PAL	
								Totals:	9.66	9.66				
10H	23	0935	80.7	90.2	9.5	10.17	107.1							
								1	1.50	1.50	80.70	82.20		
								2	1.50	1.50	82.20	83.70		
								3	1.50	1.50	83.70	85.20		
								4	1.50	1.50	85.20	86.70	IW	
								5	1.50	1.50	86.70	88.20	HS	
								6	1.50	1.50	88.20	89.70		
								7	0.72	0.72	89.70	90.42		
								CC (w/7)	0.45	0.45	90.42	90.87	PAL	
								Totals:	10.17	10.17				
11H	23	1005	90.2	99.7	9.5	10.05	105.8							
								1	1.50	1.50	90.20	91.70		
								2	1.50	1.50	91.70	93.20		
								3	1.50	1.50	93.20	94.70	DUGWR	
								4	1.50	1.50	94.70	96.20	IW	
								5	1.50	1.50	96.20	97.70	HS	
								6	1.50	1.50	97.70	99.20		
								7	0.82	0.82	99.20	100.02		
								CC (w/7)	0.23	0.23	100.02	100.25	PAL	
								Totals:	10.05	10.05				
12H	23	1035	99.7	109.2	9.5	10.13	106.6							
								1	1.50	1.50	99.70	101.20		
								2	1.50	1.50	101.20	102.70		
								3	1.50	1.50	102.70	104.20		
								4	1.50	1.50	104.20	105.70	IW	
								5	1.50	1.50	105.70	107.20	HS	
								6	1.50	1.50	107.20	108.70		
								7	0.66	0.66	108.70	109.36		
								CC (w/7)	0.47	0.47	109.36	109.83	PAL	
								Totals:	10.13	10.13				
13H	23	1135	109.2	117.4	8.2	8.20	100.0							
								1	1.50	1.50	109.20	110.70		
								2	1.50	1.50	110.70	112.20		
								3	1.50	1.50	112.20	113.70	DUGWR	
								4	1.50	1.50	113.70	115.20	IW	
								5	1.35	1.35	115.20	116.55	HS	
								6	0.44	0.44	116.55	116.99		
								CC (w/6)	0.41	0.41	116.99	117.40	PAL	
								Totals:	8.20	8.20				
14X	23	1315	117.4	121.9	4.5	1.78	39.6							
								1	0.99	1.26	117.40	118.66		
								2	0.66	0.66	118.66	119.32	HS, IW	
								CC (w/2)	0.13	0.13	119.32	119.45	PAL	
								Totals:	1.78	2.05				
15X	23	1355	121.9	131.5	9.6	0.00	0.0							
16X	23	1425	131.5	141.1	9.6	1.43	14.9							
								1	1.22	1.22	131.50	132.72	HS, IW	

Table T2 (continued).

Core	Date (Jan 2001)	Time (local)	Core depth (mbsf) Top	Core depth (mbsf) Bottom	Length (m) Cored	Length (m) Recovered	Recovery (%)	Section	Length (m) Liner	Length (m) Curated	Section depth (mbsf) Top	Section depth (mbsf) Bottom	Catwalk samples	Comment
								CC (w/1)	0.21	0.21	132.72	132.93	PAL	
								Totals:	1.43	1.43				
17X	23	1610	141.1	145.3	4.2	0.00	0.0							
18X	23	1730	145.3	150.7	5.4	0.19	3.5							
								CC (w/CC)	0.19	0.19	145.30	145.49	PAL	
								Totals:	0.19	0.19				
19X	23	1815	150.7	160.3	9.6	0.00	0.0							
20X	23	1935	160.3	169.9	9.6	0.61	6.4							
								1	0.61	0.69	160.30	160.99	PAL	
								Totals:	0.61	0.69				
				Totals:	169.9	126.18	74.3							
194-1194B-														
1W	24	0445	0.0	110.0	110.0	0.00	0.0							
2R	24	0525	110.0	119.6	9.6	5.44	56.7							
								1	1.50	1.50	110.00	111.50		
								2	1.50	1.50	111.50	113.00		
								3	1.50	1.50	113.00	114.50		
								4	0.77	0.77	114.50	115.27		
								CC (w/4)	0.17	0.17	115.27	115.44	PAL	
								Totals:	5.44	5.44				
3R	24	0550	119.6	129.3	9.7	0.79	8.1							
								1	0.79	0.90	119.60	120.50	PAL	
								Totals:	0.79	0.90				
4R	24	0615	129.3	138.8	9.5	0.59	6.2							
								1	0.59	0.59	129.30	129.89		
								Totals:	0.59	0.59				
5R	24	0635	138.8	148.4	9.6	0.86	9.0							
								1	0.86	0.86	138.80	139.66		
								Totals:	0.86	0.86				
6R	24	0655	148.4	158.0	9.6	1.69	17.6							
								1	1.25	1.25	148.40	149.65		
								2	0.44	0.44	149.65	150.09	PAL	
								Totals:	1.69	1.69				
7R	24	0720	158.0	167.6	9.6	1.44	15.0							
								1	1.44	1.44	158.00	159.44	PAL	
								Totals:	1.44	1.44				
8R	24	0740	167.6	177.2	9.6	2.36	24.6							
								1	1.50	1.50	167.60	169.10		
								2	0.66	0.66	169.10	169.76		
								CC (w/2)	0.20	0.20	169.76	169.96	PAL	
								Totals:	2.36	2.36				
9R	24	0815	177.2	186.8	9.6	0.41	4.3							
								1	0.41	0.41	177.20	177.61	PAL	
								Totals:	0.41	0.41				
10R	24	0845	186.8	196.4	9.6	4.80	50.0							
								1	1.50	1.50	186.80	188.30		
								2	0.95	0.95	188.30	189.25	IW	
								3	1.26	1.26	189.25	190.51	HS	
								4	0.89	0.89	190.51	191.40		
								CC (w/4)	0.20	0.20	191.40	191.60	PAL	
								Totals:	4.80	4.80				
11R	24	0910	196.4	206.0	9.6	1.54	16.0							
								1	1.39	1.39	196.40	197.79		
								CC (w/CC)	0.15	0.15	197.79	197.94	PAL	
								Totals:	1.54	1.54				
12R	24	0940	206.0	215.7	9.7	0.76	7.8							
								1	0.76	0.76	206.00	206.76	PAL	
								Totals:	0.76	0.76				
13R	24	1000	215.7	225.3	9.6	0.21	2.2							
								1	0.21	0.21	215.70	215.91		
								Totals:	0.21	0.21				
14R	24	1025	225.3	234.9	9.6	0.18	1.9							
								CC (w/CC)	0.18	0.18	225.30	225.48	PAL	
								Totals:	0.18	0.18				

Table T2 (continued).

Core	Date (Jan 2001)	Time (local)	Core depth (mbsf) Top	Core depth (mbsf) Bottom	Length (m) Cored	Length (m) Recovered	Recovery (%)	Section	Length (m) Liner	Length (m) Curated	Section depth (mbsf) Top	Section depth (mbsf) Bottom	Catwalk samples	Comment
15R	24	1100	234.9	244.5	9.6	3.50	36.5							
								1	1.46	1.46	234.90	236.36	IW	
								2	1.50	1.50	236.36	237.86	HS	
								3	0.38	0.38	237.86	238.24		
								CC (w/3)	0.16	0.16	238.24	238.40	PAL	
								Totals:	3.50	3.50				
16R	24	1130	244.5	254.2	9.7	0.36	3.7							
								1	0.36	0.36	244.50	244.86		
								Totals:	0.36	0.36				
17R	24	1210	254.2	263.8	9.6	2.57	26.8							
								1	0.87	0.87	254.20	255.07	IW	
								2	1.50	1.50	255.07	256.57	HS	
								CC (w/CC)	0.20	0.20	256.57	256.77	PAL	
								Totals:	2.57	2.57				
18R	24	1235	263.8	273.4	9.6	0.73	7.6							
								CC (w/CC)	0.73	0.73	263.80	264.53	PAL	
								Totals:	0.73	0.73				
19R	24	1300	273.4	283.0	9.6	0.79	8.2							
								1	0.79	0.79	273.40	274.19	PAL	
								Totals:	0.79	0.79				
20R	24	1325	283.0	292.6	9.6	0.59	6.1							
								1	0.59	0.59	283.00	283.59	PAL	
								Totals:	0.59	0.59				
21R	24	1355	292.6	302.2	9.6	0.81	8.4							
								1	0.81	0.81	292.60	293.41	PAL	
								Totals:	0.81	0.81				
22R	24	1425	302.2	311.9	9.7	1.69	17.4							
								1	1.47	1.47	302.20	303.67	HS	
								CC (w/CC)	0.22	0.22	303.67	303.89	PAL, IW	Other
								Totals:	1.69	1.69				
23R	24	1455	311.9	321.5	9.6	1.41	14.7							
								1	1.17	1.17	311.90	313.07	HS	
								CC (w/1)	0.24	0.24	313.07	313.31	PAL	
								Totals:	1.41	1.41				
24R	24	1535	321.5	331.1	9.6	2.65	27.6							
								1	1.50	1.50	321.50	323.00		
								2	0.91	0.91	323.00	323.91	HS, IW	
								CC (w/2)	0.24	0.24	323.91	324.15	PAL	
								Totals:	2.65	2.65				
25R	24	1615	331.1	340.7	9.6	9.52	99.2							
								1	1.34	1.34	331.10	332.44		
								2	1.28	1.28	332.44	333.72		
								3	1.45	1.45	333.72	335.17		
								4	1.50	1.50	335.17	336.67		
								5	1.01	1.01	336.67	337.68	HS	
								6	1.50	1.50	337.68	339.18	IW	
								7	1.27	1.27	339.18	340.45		
								CC (w/7)	0.17	0.17	340.45	340.62	PAL	
								Totals:	9.52	9.52				
26R	24	1700	340.7	350.3	9.6	7.19	74.9							
								1	1.41	1.41	340.70	342.11		
								2	1.50	1.50	342.11	343.61		
								3	1.31	1.31	343.61	344.92	IW	
								4	1.17	1.17	344.92	346.09	HS	
								5	0.56	0.56	346.09	346.65		
								6	1.15	1.15	346.65	347.80		
								CC (w/6)	0.09	0.09	347.80	347.89	PAL	
								Totals:	7.19	7.19				
27R	24	1745	350.3	359.9	9.6	3.34	34.8							
								1	1.10	1.10	350.30	351.40		
								2	1.26	1.26	351.40	352.66	IW	
								3	0.86	0.86	352.66	353.52	HS	
								CC (w/CC)	0.12	0.12	353.52	353.64	PAL	
								Totals:	3.34	3.34				
28R	24	1845	359.9	369.5	9.6	8.61	89.7							
								1	1.21	1.21	359.90	361.11		
								2	1.46	1.46	361.11	362.57		
								3	1.07	1.07	362.57	363.64		

Table T2 (continued).

Core	Date (Jan 2001)	Time (local)	Core depth (mbsf) Top	Core depth (mbsf) Bottom	Length (m) Cored	Length (m) Recovered	Recovery (%)	Section	Length (m) Liner	Length (m) Curated	Section depth (mbsf) Top	Section depth (mbsf) Bottom	Catwalk samples	Comment
								4	1.50	1.50	363.64	365.14		
								5	1.44	1.44	365.14	366.58		
								6	1.02	1.02	366.58	367.60	IW	
								7	0.79	0.79	367.60	368.39	HS	
								CC (w/7)	0.12	0.12	368.39	368.51	PAL	
								Totals:	8.61	8.61				
29R	24	1935	369.5	379.2	9.7	5.56	57.3							
								1	0.96	0.96	369.50	370.46		
								2	1.50	1.50	370.46	371.96		
								3	1.50	1.50	371.96	373.46	IW	
								4	1.31	1.31	373.46	374.77	HS	
								CC (w/CC)	0.29	0.29	374.77	375.06	PAL	
								Totals:	5.56	5.56				
30R	24	2025	379.2	388.8	9.6	5.73	59.7							
								1	1.50	1.50	379.20	380.70		
								2	1.50	1.50	380.70	382.20		
								3	1.50	1.50	382.20	383.70	IW	
								4	1.00	1.00	383.70	384.70	HS	
								CC (w/4)	0.23	0.23	384.70	384.93	PAL	
								Totals:	5.73	5.73				
31R	24	2125	388.8	398.4	9.6	2.05	21.4							
								1	1.47	1.47	388.80	390.27	IW	
								2	0.53	0.53	390.27	390.80	HS	
								CC (w/2)	0.05	0.05	390.80	390.85	PAL	All to PAL
								Totals:	2.05	2.05				
32R	24	2215	398.4	407.9	9.5	1.78	18.7							
								1	1.11	1.11	398.40	399.51	IW	
								2	0.52	0.52	399.51	400.03	HS	
								CC (w/CC)	0.15	0.15	400.03	400.18	PAL	
								Totals:	1.78	1.78				
33R	24	2320	407.9	417.5	9.6	4.14	43.1							
								1	1.05	1.05	407.90	408.95	IW	
								2	1.45	1.45	408.95	410.40	HS	
								3	1.46	1.46	410.40	411.86		
								CC (w/CC)	0.18	0.18	411.86	412.04	PAL	
								Totals:	4.14	4.14				
34R	25	0030	417.5	427.1	9.6	5.13	53.4							
								1	1.48	1.48	417.50	418.98	IW	
								2	1.45	1.45	418.98	420.43		
								3	0.49	0.49	420.43	420.92		
								4	1.36	1.45	420.92	422.37		
								5	0.35	0.43	422.37	422.80		
								Totals:	5.13	5.30				
				Totals:	427.1	89.22	20.9							

Notes: CC = core catcher (number in parentheses indicates which section the core catcher is stored with). Catwalk samples: HS = headspace, IW = interstitial water, PAL = paleontology sample, DUGWR = sample request code.

Table T3. Lithologic units and subunits, Site 1194.

		Hole 1194A				Hole 1194B					
		Core, section, interval (cm)		Depth (mbsf)		Core, section, interval (cm)		Depth (mbsf)			
Unit	Subunit	Top	Base	Top	Base	Top	Base	Top	Base	Description	Interpretation
I		1H-1, 0	1H-3, 42	0.0	3.8					Skeletal packstone with planktonic foraminifers. Pale yellow.	Hemipelagic, current-swept seafloor
II		1H-3, 42	14X-1, 0	3.8	117.4					Mudstone/wackestone with planktonic foraminifers. Light olive to greenish gray.	Hemipelagic, input of distal turbidites
III	IIIA	14X-1, 0	18X-1, 19	117.4	160.3					Skeletal packstone/floatstone, dominated by bryozoans. Dark gray.	Neritic ramp
III	IIIB	20X-1, 0	?	160.3	?	7R-1, 0	9R-1, 14	158.0	177.3	Skeletal packstone, dominated by small benthic foraminifers. Dark gray.	Neritic upper slope
IV	IVA					9R-1, 14	18R-1, 73	177.3	264.5	Silt-sized packstone with clay and dolomite rhombs. Light olive-gray.	Hemipelagic
IV	IVB					18R-1, 73	25R-3, 0	264.5	331.1	Silt-sized grainstone with quartz. Light olive-gray.	Hemipelagic
V	VA					25R-3, 0	29R-3, 13	331.1	372.1	Silt-sized packstone with dark layers crossed by bioturbation. Greenish gray.	Hemipelagic
V	VB					29R-3, 13	34R-4, 12	372.1	421.1	Skeletal packstone with dark layers crossed by bioturbation. Light greenish gray to pale yellow.	Transgressive system/hemipelagic
VI						34R-4, 12	?	421.1	?	Basaltic basement with olivine, epidote, feldspar, and calcite-filled veins. Reddish black.	Basement

Note: ? = Not defined.

Table T4. Biostratigraphic datums, Site 1194.

Datum	Core, section, interval (cm)	Depth (mbsf)		Mean depth (mbsf)	Age (Ma)
		First absence or presence	Last presence or absence		
	194-1194A-				
LO *Pseudoemiliania lacunosa*	1H-1, 0, to 1H-2, 45	0.00	1.95	0.98	0.46
LO *Globorotalia tosaensis*	1H-1, 0, to 1H-2, 45	0.00	1.95	0.98	0.65
LO *Discoaster surculus*	1H-1, 0, to 1H-CC	0.00	4.65	2.33	2.60
LO *Discoaster tamalis*	1H-CC to 2H-CC	4.65	14.40	9.53	2.80
LO *Dentoglobigerina altispira*	1H-CC to 2H-CC	4.65	14.40	9.53	3.09
LO *Sphaeroidinellopsis seminulina*	2H-CC to 3H-CC	14.40	23.79	19.10	3.12
LO *Reticulofenestra pseudoumbilica*	3H-CC to 4H-CC	23.79	33.80	28.80	3.70
LO *Amaurolithus* spp.	5H-CC to 6H-CC	42.82	52.29	47.56	4.00
FO *Globorotalia puncticulata*	6H-2, 80, to 6H-5, 80	45.00	49.50	47.25	4.40
LO *Discoaster quinqueramus*	7H-CC to 8H-CC	62.18	71.63	66.91	5.60
FO *Globorotalia margaritae*	9H-CC to 10H-CC	80.84	90.85	85.85	6.40
FO *Discoaster surculus*	12H-CC to 13H-CC	109.80	117.38	113.59	7.50
LO *Cyclicargolithus floridanus*	13X-CC to 14X-1, 48	117.38	117.88	117.63	11.90
	194-1194B-				
LO *Sphenolithus heteromorphus*	5R-1 to 9R-1, 38	138.80	177.58	158.19	13.60
FO *Sphenolithus heteromorphus*	Below 27R-CC				18.20
LO *Globigerina ciperoensis*	27R-CC to 29R-CC	350.30	369.50	359.90	19.30

Note: FO = first occurrence, LO = last occurrence.

Table T5. Summary of biostratigraphic and paleoenvironmental interpretations, Site 1194. (See table notes. Continued on next page.)

Hole, core, section (cm)	Depth (mbsf)	Foraminiferal assemblages					Comments on washed fraction, >63 µm	Paleowater depth (m)					Depositional setting	Lithologic unit
		PF	ONBF	ESBF	LBF	Pres		<30	<60	<100	>100	>200		
194-														
1194A-1H-CC	4.65	Dom	R			G	Siliciclastic grains, PF, including fine sands					X	Hemipelagic	I
1194A-2H-CC	14.40	Dom	R			G	PF, PF debris, fine sands predominate					X	Hemipelagic	II
1194A-3H-CC	23.79	Dom	R			G	PF, PF debris, medium sands predominate					X	Hemipelagic	
1194A-4H-CC	33.80	Dom	R			G	PF, PF debris, medium sands predominate					X	Hemipelagic	
1194A-5H-CC	43.12	Dom	R			G	PF, PF debris, fine sands predominate					X	Hemipelagic	
1194A-6H-CC	52.59	Dom	R			G	PF, PF debris, fine sands predominate					X	Hemipelagic	
1194A-7H-CC	62.18	Dom	C			G	Nearly half blackened grains, limited fine sands					X	Hemipelagic	
1194A-8H-CC	71.63	Dom	R			G	PF and PF debris, some blackened					X	Hemipelagic	
1194A-9H-CC	80.84	Dom	R			G	PF and PF debris, blackened common					X	Hemipelagic	
1194A-10H-CC	90.85	Dom	R			G	Nearly half blackened grains, limited fine sands					X	Hemipelagic	
1194A-11H-CC	100.23	Dom	C			G	Nearly half blackened grains, limited fine sands					X	Hemipelagic	
1194A-12H-CC	109.80	Dom	R			G	Nearly half blackened grains, limited fine sands					X	Hemipelagic	
1194A-13H-CC	117.38	Dom	C			G	Solitary coral, siliciclastic, reworked grains, sorted PF					X	Hemipelagic	
1194B-2R-CC	115.44				P	P	Lithified limestone: bryozoans abundant		?	X			Platform	III
1194A-14X-CC	119.45	R	C	C	C	G	Bryozoan dominant, quartz grains		X				Platform	
1194B-3R-CC	120.48	R	R?	Div	C	P	Bryozoan dominant, quartz, black grains, glauconite		X				Platform	
1194A-16X-CC	132.93			Div	A	G	Bryozoan fragments, *A. hauerina, A. radiata*		X				Platform	
1194B-4R-CC	138.80			C	C	M	Bryozoan fragments, *A. hauerina, A. radiata*		X				Platform	
1194A-18X-CC	145.49			R	A	P	Fine, recrystallized, bryozoan debris; sorted *A. hauerina*		X				Platform	
1194B-5R-CC	148.40			Div	A	P	*Amphistegina* dominant recognizable constituent		X				Platform	
1194B-6R-CC	158.00			C	A	P	Heavily recrystallized, relatively flat *Amphistegina*		X				Platform	
1194A-20X-CC	160.97	R	R	C	R	P	Bioclastic fragments med to fine, poorly preserved				?		Proximal periplatform	
1194B-7R-CC	159.42			Div		P	Heavily recrystallized bryozoan fragments				?		Proximal periplatform	
1194B-8R-CC	169.96		R	Div	R?	M	Predominantly fine sand; benthic foraminifers diverse, ostracods				?		Proximal periplatform	
1194B-9R-CC	177.58	R	R			G	Very fine muds with a few ostracods						Unknown	IVA
1194B-10R-CC	191.60	R	R			G	Very fine muds with a few ostracods						Unknown	
1194B-11R-CC	197.94	C	C	R		M	Fine sand–sized fragments of bryozoans, MBF				X		Proximal periplatform	
1194B-12R-CC	206.74	C	?	R		P	Medium/ fine sand–sized fragments of bryozoans, MBF				X		Proximal periplatform	
1194B-13R-CC	215.91			Div	C/T	M	Medium/fine sand–sized fragments of bryozoans, rounded LBF				?		Proximal periplatform	
1194B-14R-CC	225.48			C		P	Medium/ fine sand–sized fragments of bryozoans, MBF				?		Proximal periplatform	
1194B-15R-CC	238.40	A	A	R		P	Medium/ fine sand–sized fragments of bryozoans, MBF				X		Proximal periplatform	
1194B-16R-CC	244.86	A	C	C	R/T	P	PF, bryozoan debris, quartz, reworked grains, glauconite				X		Proximal periplatform	
1194B-17R-CC	256.77	C	C		R/T	P	PF, bryozoan debris, quartz, reworked grains, glauconite				X		Proximal periplatform	
1194B-18R-CC	264.53	A	R			VP	Fine/very fine bryozoan debris, PF, recrystallized					X	Distal periplatform	IVB
1194B-19R-CC	274.17	A	R?			VP	Fine/very fine bryozoan debris, PF, recrystallized					X	Distal periplatform	
1194B-20R-CC	283.54	A	C			M	Fine/very fine bryozoan debris, PF					X	Distal periplatform	
1194B-21R-CC	293.39	A	C	C		P	Fine/very fine bryozoan debris, PF, glauconite, black grains					X	Distal periplatform	
1194B-22R-CC	303.89	A	A	?		M–VP	Fine/very fine bryozoan debris, PF, glauconite, black grains					X	Distal periplatform	
1194B-23R-CC	313.31	C	?			VP	Glauconite and black grains common, little identifiable						Distal periplatform	
1194B-24R-CC	324.15	C	C			M–VP	Very fine neritic/PF bioclastics; pyrite and glauconite					X	Distal periplatform	
1194B-25R-CC	340.62					VP	Very fine bioclastics, recrystallized, little identifiable						Distal periplatform	VA
1194B-26R-CC	347.89	C	C			M–VP	Very fine recrystallized bioclastics, PF, ONBF					?	Distal periplatform	
1194B-27R-CC	353.64	C	C			P–VP	Very fine recrystallized bioclastics, PF, ONBF					?	Distal periplatform	
1194B-28R-CC	368.51						No washable fraction, too lithified					?		

Table T5 (continued).

Hole, core, section (cm)	Depth (mbsf)	Foraminiferal assemblages					Comments on washed fraction, >63 µm	Paleowater depth (m)					Depositional setting	Lithologic unit
		PF	ONBF	ESBF	LBF	Pres		<30	<60	<100	>100	>200		
1194B-29R-CC	375.06	A	C			P–VP	Very fine recrystallized bioclastics, PF, ONBF					?	Distal periplatform	VB
1194B-30R-CC	384.93	C	?		R/T	VP	Very fine bioclastics, minor quartz, reworked material				?		Proximal periplatform	
1194B-31R-CC	390.85	C	C		R/T	VP	Very fine bioclastics, minor quartz, reworked material				?		Proximal periplatform	
1194B-32R-CC	400.18	A	A		R/T	P–VP	Very fine bioclastics, minor quartz, reworked material				?		Proximal periplatform	
1194B-33R-CC	412.04	R	R			VP	Very fine calcitic bioclastics, heavily recrystallized						Unknown	
1194B-34R-4	421.03			?	A	G	LBF grainstone immediately above basement			X			Platform	

Notes: Based on microscopic analysis of biogenic sediment constituents >63 µm, particularly benthic foraminifers, from core catcher samples. Foraminifer assemblages: PF = planktonic foraminifers, ONBF = outer neritic to upper bathyal benthic foraminifers, ESBF = middle to inner neritic smaller benthic foraminifers, LBF = larger benthic foraminifers, Pres = preservation. Div = common and diverse, Dom = dominant; A = abundant, C = common, G = good, M = moderate, P = poor, R = rare, T = transported, VP = very poor, ? = uncertain. MBF = mixed benthic foraminiferal assemblages including inner/middle neritic with outer neritic/upper bathyal representatives.

Table T6. Age-depth control points, Site 1194.

Source	Datum	Age (Ma)	Top: FO presence or LO absence		Bottom: LO presence or FO absence		Average depth (mbsf)	Uncertainty (m)	
			Core, section, interval (cm)	Depth (mbsf)	Core, section, interval (cm)	Depth (mbsf)		Up-section	Down-section
			194-1194A-		194-1194A-				
PF	LO *Globorotalia tosaensis*	0.6	1H-1, 0	0.00	1H-2, 45	1.95	0.98	0.98	0.98
CN	LO *Discoaster surculus*	2.6	1H-1, 0	0.00	1H-BCI	4.70	2.35	2.35	2.35
CN	LO *Discoaster tamalis*	2.8	1H-CC	4.65	2H-CC	14.40	9.53	4.88	4.88
PF	LO *Dentoglobigerina altispira*	3.09	1H-CC	4.65	2H-CC	14.40	9.53	4.88	4.88
CN	LO *Sphaeroidinellopsis seminulina*	3.12	2H-CC	14.40	3H-CC	23.79	19.10	4.70	4.70
CN	LO *Reticulofenestra pseudoumbilica*	3.7	3H-CC	23.79	4H-CC	33.80	28.80	5.01	5.01
CN	LO *Amaurolithus* spp.	4.0	5H-CC	42.82	6H-CC	52.29	47.56	4.74	4.74
PF	FO *Globoconella puncticulata*	4.4	6H-2, 80	45.00	6H-5, 80	49.50	47.25	2.25	2.25
CN	LO *Discoaster quinqueramus*	5.6	7H-CC	62.18	8H-CC	71.63	66.91	4.73	4.72
PF	FO *Globorotalia margaritae*	6.4	9H-CC	80.84	10H-CC	90.85	85.85	5.01	5.01
CN	FO *Discoaster surculus*	7.5	12H-CC	109.80	13H-CC	117.38	113.59	3.79	3.79
CN	LO *Cyclicargolithus floridanus*	11.9	14X-1, 16	117.56	16X-BCI	141.10	129.33	11.77	11.77
			194-1194B-		194-1194B-				
CN	LO *Sphenolithus heteromorphus*	13.6	5R-1, 0	138.80	9R-1, 38	177.58	158.19	19.39	19.39
PF	LO *Globigerina ciperoensis*	19.3	27R-CC	350.30	29R-BCI	379.20	364.75	14.45	14.45

Notes: Source: PF = planktonic foraminifers, CN = calcareous nannoplankton. Datum: LO = last occurrence, FO = first occurrence. Core, section, interval: BCI = bottom of cored interval.

Table T7. Interpolated ages of lithologic unit boundaries and seismic reflectors, Site 1194.

	Top of unit		
	Depth (mbsf)	Age (Ma)	Comments
Lithologic unit:			
I	0	Not defined	
II	3.8	? to 2.6	Hiatus?
IIIA	117.4	7.7 to 11.8	Hiatus?
IIIB	148.0	12.9	
IVA	177.3	13.6	
IVB	264.5	16.4	
VA	331.1	18.6	
VB	372.1	19.9	
VI	421.1	21.5	
Seismic sequences and reflectors:			
Megasequence D	0	Not defined	
D-black	Not present		
D-turquoise	65	5.3	
Megasequence C	Not present		
Megasequence B	115	7.7 to 11.8	Hiatus
Megasequence A	Not present		
Basement	423	21.6	

Table T8. Headspace gas composition, Site 1194.

Core, section	Depth (mbsf)	C_1 (ppmv)
194-1194A-		
1H-2	1.50	1.9
2H-5	10.70	1.6
3H-5	20.20	1.9
4H-5	29.70	2.3
5H-5	39.20	1.8
6H-5	48.70	1.9
9H-5	77.20	2.0
10H-5	86.70	1.9
11H-5	96.20	1.7
12H-5	105.70	1.8
13H-5	115.20	1.7
14X-2	118.66	2.2
16X-1	131.50	1.7
194-1194B-		
10R-3	189.25	1.8
15R-2	236.36	1.8
17R-2	255.07	2.2
22R-1	302.20	2.3
23R-1	311.90	2.0
24R-2	323.76	2.3
25R-5	336.67	2.4
26R-4	344.92	2.5
27R-3	352.66	2.0
28R-7	367.60	2.2
29R-4	373.46	1.9
30R-4	383.70	2.2
31R-2	390.27	1.9
32R-2	399.51	2.1
33R-2	408.95	1.7

Note: C_1 = methane.

Table T9. Interstitial water chemistry, Site 1194.

Core, section, interval (cm)	Depth (mbsf)	pH	Alk (mM)	Salinity	Cl^- (mM)	SO_4^{2-} (mM)	Na^+ (mM)	Mg^{2+} (mM)	Ca^{2+} (mM)	K^+ (mM)	NH_4^+ (μM)	Sr^{2+} (μM)	Li^+ (μM)	Mn^{2+} (μM)	Fe^{2+} (μM)
194-1194A-															
1H-2, 140–150	2.90	7.57	2.22	36.0	558	28.85	471	54.46	12.58	10.77	29	105	29.18	0.44	26.75
2H-4, 140–150	10.60	7.36	2.20	35.5	563	28.08	476	53.74	12.49	11.13	67	154	31.89	0.15	1.74
3H-4, 140–150	20.10	7.37	2.40	35.5	567	27.77	479	53.16	13.24	10.97	118	212	34.46	0.27	15.00
4H-4, 140–150	29.60	7.48	2.94	35.5	565	26.24	474	51.98	14.39	10.75	166	268	38.47	0.30	1.61
5H-4, 140–150	39.10	7.52	2.52	35.5	565	25.85	473	51.98	14.52	10.56	192	297	39.89	0.36	0.98
6H-4, 140–150	48.60	7.62	2.59	35.5	565	25.40	473	51.24	14.86	10.21	240	341	43.60	0.45	6.82
7H-4, 140–150	58.10	7.32	2.40	35.5	565	24.91	473	50.76	15.22	9.88	279	321	38.87	0.37	3.65
8H-4, 140–150	67.60	7.29	2.42	35.5	562	24.51	469	50.05	15.96	9.60	314	422	48.82	0.50	5.67
9H-4, 140–150	77.10	7.42	2.32	35.5	564	23.68	469	49.72	16.79	9.00	345	469	51.11	0.47	13.00
10H-4, 140–150	86.60	7.35	2.14	35.5	565	23.18	468	48.99	18.12	8.87	387	518	54.85	0.31	7.75
11H-4, 140–150	96.10	7.46	1.99	35.5	564	23.22	466	49.04	19.03	8.67	434	539	56.02	0.30	14.55
12H-4, 140–150	105.60	7.30	1.93	35.5	565	22.86	466	48.54	19.40	8.43	461	561	59.86	0.30	10.35
13H-4, 140–150	115.10	7.37	1.76	35.5	565	21.77	463	48.41	20.20	8.15	450	588	63.85	0.30	29.42
14X-2, 140–150	119.14	7.72	1.71	35.0	564	21.49	463	47.39	20.65	8.01	470	565	64.20	0.22	0.89
16X-1, 140–150	132.62	7.68	1.75	35.5	564	22.29	462	48.26	21.13	7.79	470	581	61.99	0.23	0.87
194-1194B-															
10R-2, 83–95	189.13	7.64	1.40	35.0	565	20.93	451	49.17	25.21	6.73	507	649	59.41	0.18	2.98
15R-1, 133–146	236.23	7.88	1.11	35.0	561	20.10	430	50.16	32.74	5.03	489	713	58.95	0.28	1.73
17R-1, 70–87	254.90	8.17	0.68	35.0	562	19.07	427	48.45	35.27	5.60	566	698	52.99	0.16	1.18
22R-CC, 1–17	303.68	8.18	0.67	35.0	562	18.65	409	46.74	46.15	4.45	578	763	44.44	0.20	2.78
24R-2, 81–91	323.81	8.04	0.88	35.5	564	18.77	411	45.00	48.51	3.93	556	754	43.77	0.32	1.24
25R-6, 140–150	339.18	7.91	0.94	35.5	560	18.95	408	43.76	49.41	3.80	600	750	45.51	0.20	9.74
26R-3, 116–131	344.77	7.94	0.91	35.5	562	18.75	409	43.44	49.72	3.73	588	738	48.95	0.16	8.75
27R-2, 112–126	352.52	7.98	0.85	35.5	564	18.86	411	42.95	50.74	3.63	595				
28R-6, 91–102	367.49			36.0	565	19.56	416	42.48	49.58	4.12	549				
29R-3, 140–150	373.36	7.85	0.81	35.0	556	19.32	402	39.87	54.97	3.37	552				
30R-3, 140–150	383.60	8.38	0.62	35.0	557	18.74	395	37.69	60.13	3.65	502				
31R-1, 135–147	390.15			35.5	564	19.21	407	38.45	56.85	4.33	495	597	72.70	0.60	10.33
32R-1, 99–111	399.39			35.5	563	18.98	400	36.60	61.68	4.04	488				
33R-1, 95–105	408.85	7.87	0.78	35.5	558	19.19	394	35.75	63.23	4.15	502	590	78.67	3.79	1.31
34R-1, 135–148	418.85			35.5	558	18.91	395	34.41	63.93	3.62	492				

Note: Alk = alkalinity.

Table T10. Percentages of aragonite, calcite, dolomite, and noncarbonate minerals, Site 1194.

Core, section, interval (cm)	Depth (mbsf)	Aragonite (wt%)	Calcite (wt%)	Dolomite (wt%)	Non-carbonate (wt%)
194-1194A-					
1H-2, 70–71	2.20	0	62	3	35
2H-2, 70–71	6.90	0	77	0	23
2H-4, 70–71	9.90	0	77	0	23
2H-6, 70–71	12.90	0	76	0	24
3H-2, 70–71	16.40	0	82	0	18
3H-4, 70–71	19.40	0	70	0	30
3H-6, 70–71	22.40	0	75	0	25
4H-2, 70–71	25.90	0	71	2	26
4H-4, 70–71	28.90	0	75	0	25
4H-6, 70–71	31.90	0	76	0	24
5H-2, 70–71	35.40	0	57	2	41
5H-4, 70–71	38.40	0	81	0	19
5H-6, 70–71	41.40	0	81	0	19
6H-2, 70–71	44.90	0	79	0	21
6H-4, 70–71	47.90	0	69	0	31
6H-6, 70–71	50.90	0	70	0	30
7H-2, 70–71	54.40	0	77	0	23
7H-4, 70–71	57.40	0	80	0	20
7H-6, 70–71	60.40	0	73	0	27
8H-2, 70–71	63.90	0	79	0	21
8H-4, 70–71	66.90	0	79	0	21
8H-6, 70–71	69.90	0	79	0	21
9H-2, 70–71	73.40	0	69	0	31
9H-4, 70–71	76.40	0	85	0	15
9H-6, 70–71	79.40	0	70	0	30
10H-2, 70–71	82.90	0	77	0	23
10H-4, 70–71	85.90	0	77	0	23
10H-6, 70–71	88.90	0	77	0	23
11H-2, 70–71	92.40	0	81	0	19
11H-4, 70–71	95.40	0	88	0	12
11H-6, 70–71	98.40	0	78	0	22
12H-2, 70–71	101.90	0	78	0	22
12H-4, 70–71	104.90	0	80	0	20
12H-6, 70–71	107.90	0	84	0	16
13H-2, 70–71	111.40	0	88	0	12
13H-4, 70–71	114.40	0	86	0	14
14X-1, 75–78	118.15	0	95	0	5
20X-1, 31–32	160.61	0	98	0	2
194-1194B-					
2R-2, 70–71	112.20	0	89	0	11
2R-4, 50–51	115.00	0	83	3	14
3R-1, 77–78	120.37	0	25	43	32
4R-1, 34–35	129.64	0	59	11	30
5R-1, 44–45	139.24	0	69	13	17
6R-1, 50–51	148.90	0	80	16	5
6R-2, 33–34	149.98	0	76	13	11
7R-1, 107–108	159.07	0	88	2	10
8R-1, 81–82	168.40	0	95	0	5
8R-2, 46–47	169.56	0	92	0	8
9R-1, 23–24	177.43	0	45	0	55
10R-1, 50–51	187.30	0	46	6	49
10R-3, 50–51	189.75	0	58	23	19
11R–1, 52–53	196.92	0	90	0	10
12R-1, 50–51	206.50	0	71	23	6
13R-1, 10–11	215.80	0	80	9	11
14R-CC, 10–11	225.40	0	86	11	3
15R-1, 50–51	235.40	0	53	13	34
16R-1, 10–12	244.60	0	74	17	9
17R-1, 34–35	254.54	0	83	0	17
17R-2, 90–92	255.87	0	88	5	7
18R-CC, 39–40	264.19	0	84	8	8
19R-1, 35–37	273.75	0	83	11	6
20R-1, 51–52	283.51	0	93	0	7
21R-1, 65–67	293.25	0	89	0	11
22R-1, 49–51	302.69	0	83	0	17
23R-1, 86–87	312.76	0	61	0	39
24R-1, 75–78	322.25	0	83	0	17
24R-2, 62–63	323.62	0	75	0	25
25R-1, 74–75	331.84	0	83	0	17
25R-3, 65–66	334.37	0	79	0	21
25R-5, 27–28	336.94	0	76	0	24
26R-1, 62–66	341.32	0	87	0	13
26R-3, 47–50	344.08	0	79	0	21
26R-5, 49–50	346.58	0	90	0	10
27R-2, 65–66	352.05	0	89	0	11
28R-1, 27–28	360.17	0	86	0	14
28R-3, 34–35	362.91	0	82	0	18
28R-5, 31–32	365.45	0	79	0	21
29R-1, 39–40	369.89	0	86	0	14
29R-3, 52–53	372.48	0	84	0	16
30R-1, 57–58	379.77	0	90	0	10
30R-3, 51–51	382.71	0	77	0	23
31R-1, 50–51	389.30	0	93	0	7
31R-2, 47–48	390.74	0	97	0	3
32R-1, 47–48	398.87	0	80	0	20
32R-2, 44–45	399.95	0	94	0	6
33R-1, 51–52	408.41	0	96	0	4
33R-2, 50–51	409.45	0	99	0	1
33R-3, 50–51	410.90	0	93	0	7
34R-1, 50–51	418.00	0	92	0	8
34R-2, 50–51	419.48	0	79	0	21
34R-3, 20–21	420.63	0	92	0	8

Table T11. Carbon, nitrogen, sulfur, and hydrogen values and C/N and C/S ratios in sediments, Site 1194. (See table notes. Continued on next page.)

Core, section	Depth (mbsf)	IC (wt%)	$CaCO_3$ (wt%)	TC (wt%)	TOC (wt%)	Total N (wt%)	Total S (wt%)	Total H (wt%)	C/N ratio	C/S ratio
194-1194A-										
1H-2	2.20	10.69	89.1	10.73	0.04	0.05	0.09	0.18	0.75	0.43
2H-2	6.90	9.19	76.6	—	—	—	—	—	—	—
2H-4	9.90	9.25	77.0	—	—	—	—	—	—	—
2H-6	12.90	9.18	76.5	—	—	—	—	—	—	—
3H-2	16.40	9.82	81.8	—	—	—	—	—	—	—
3H-4	19.40	8.36	69.6	9.02	0.66	0.07	0.27	0.31	10.02	2.49
3H-6	22.40	9.01	75.1	—	—	—	—	—	—	—
4H-2	25.90	8.83	73.6	9.16	0.33	0.08	0.73	0.28	4.40	0.46
4H-4	28.90	9.01	75.0	—	—	—	—	—	—	—
4H-6	31.90	9.17	76.4	—	—	—	—	—	—	—
5H-2	35.40	7.07	58.9	7.58	0.51	0.01	0.65	0.44	63.31	0.78
5H-4	38.40	9.69	80.7	—	—	—	—	—	—	—
5H-6	41.40	9.68	80.6	—	—	—	—	—	—	—
6H-2	44.90	9.45	78.7	—	—	—	—	—	—	—
6H-4	47.90	8.31	69.2	8.70	0.39	0.01	0.41	0.34	48.75	0.95
6H-6	50.90	8.43	70.2	—	—	—	—	—	—	—
7H-2	54.40	9.25	77.1	—	—	—	—	—	—	—
7H-4	57.40	9.59	79.9	—	—	—	—	—	—	—
7H-6	60.40	8.82	73.4	9.13	0.31	0.12	0.50	0.37	2.70	0.62
8H-2	63.90	9.54	79.5	—	—	—	—	—	—	—
8H-4	66.90	9.51	79.2	—	—	—	—	—	—	—
8H-6	69.90	9.46	78.8	—	—	—	—	—	—	—
9H-2	73.40	8.34	69.5	8.78	0.44	0.05	0.67	0.33	8.42	0.65
9H-4	76.40	10.18	84.8	—	—	—	—	—	—	—
9H-6	79.40	8.40	70.0	8.69	0.29	0.07	0.17	0.33	4.39	1.76
10H-2	82.90	9.27	77.2	—	—	—	—	—	—	—
10H-4	85.90	9.23	76.9	—	—	—	—	—	—	—
10H-6	88.90	9.22	76.8	—	—	—	—	—	—	—
11H-2	92.40	9.73	81.1	—	—	—	—	—	—	—
11H-4	95.40	10.59	88.2	—	—	—	—	—	—	—
11H-6	98.40	9.42	78.4	—	—	—	—	—	—	—
12H-2	101.90	9.33	77.8	9.58	0.25	0.00	0.32	0.28	123.10	0.77
12H-4	104.90	9.57	79.7	—	—	—	—	—	—	—
12H-6	107.90	10.04	83.7	—	—	—	—	—	—	—
13H-2	111.40	10.62	88.5	—	—	—	—	—	—	—
13H-4	114.40	10.35	86.2	—	—	—	—	—	—	—
14X-1	118.15	11.38	94.8	—	—	—	—	—	—	—
194-1194B-										
2R-2	112.20	10.69	89.1	—	—	—	—	—	—	—
2R-4	115.00	10.29	85.7	—	—	—	—	—	—	—
3R-1	120.37	8.15	67.9	8.34	0.19	0.00	0.54	0.01	—	0.35
4R-1	129.64	8.44	70.3	—	—	—	—	—	—	—
5R-1	139.24	9.93	82.8	—	—	—	—	—	—	—
6R-1	148.90	11.44	95.3	—	—	—	—	—	—	—
6R-2	149.98	10.68	89.0	10.66	0.00	0.00	0.19	0.11	—	—
7R-1	159.07	10.77	89.7	—	—	—	—	—	—	—
20X-1	160.61	11.74	97.8	—	—	—	—	—	—	—
8R-1	168.41	11.35	94.5	—	—	—	—	—	—	—
8R-2	169.56	11.03	91.9	—	—	—	—	—	—	—
9R-1	177.43	5.44	45.4	5.69	0.25	0.03	0.69	0.44	8.19	0.36
10R-1	187.30	6.13	51.1	—	—	—	—	—	—	—
10R-3	189.75	9.77	81.4	—	—	—	—	—	—	—
11R-1	196.92	10.85	90.4	—	—	—	—	—	—	—
12R-1	206.50	11.26	93.8	—	—	—	—	—	—	—
13R-1	215.80	10.65	88.7	—	—	—	—	—	—	—
14R-CC	225.40	11.65	97.1	—	—	—	—	—	—	—
15R-1	235.40	7.93	66.1	8.20	0.27	0.00	0.46	0.28	62.70	0.59
16R-1	244.60	10.94	91.2	—	—	—	—	—	—	—
17R-1	254.54	9.95	82.9	—	—	—	—	—	—	—
17R-2	255.97	11.21	93.4	—	—	—	—	—	—	—
18R-CC	264.19	11.03	91.9	11.18	0.15	0.00	0.08	0.03	—	1.85
19R-1	273.77	11.32	94.3	—	—	—	—	—	—	—
20R-1	283.46	11.18	93.1	—	—	—	—	—	—	—
21R-1	293.25	10.73	89.4	—	—	—	—	—	—	—
22R-1	302.69	9.92	82.6	—	—	—	—	—	—	—

Table T11 (continued).

Core, section	Depth (mbsf)	IC (wt%)	$CaCO_3$ (wt%)	TC (wt%)	TOC (wt%)	Total N (wt%)	Total S (wt%)	Total H (wt%)	C/N ratio	C/S ratio
23R-1	312.76	7.32	61.0	7.47	0.15	0.01	0.19	0.14	21.76	0.80
24R-1	322.28	10.02	83.5	—	—	—	—	—	—	—
24R-2	323.63	8.95	74.5	9.00	0.06	0.05	0.30	0.27	1.04	0.19
25R-1	331.84	10.00	83.3	9.73	0.00	0.00	0.11	0.11	—	—
25R-3	334.37	9.50	79.1	—	—	—	—	—	—	—
25R-5	336.94	9.11	75.9	—	—	—	—	—	—	—
26R-1	341.32	10.38	86.5	—	—	—	—	—	—	—
26R-3	344.08	9.39	78.2	9.44	0.05	0.05	0.13	0.22	1.06	0.38
26R-5	346.58	10.86	90.5	—	—	—	—	—	—	—
27R-2	352.05	10.64	88.6	—	—	—	—	—	—	—
28R-1	360.16	10.29	85.7	—	—	—	—	—	—	—
28R-3	362.91	9.84	82.0	9.64	0.00	0.02	0.17	0.29	—	—
28R-5	365.45	9.47	78.9	9.52	0.05	0.02	0.21	0.27	2.08	0.24
29R-1	369.87	10.28	85.6	—	—	—	—	—	—	—
29R-3	372.48	10.03	83.6	—	—	—	—	—	—	—
30R-1	379.78	10.84	90.3	—	—	—	—	—	—	—
30R-3	382.71	9.20	76.7	8.49	0.00	0.00	0.15	0.12	—	—
31R-1	389.30	11.15	92.9	—	—	—	—	—	—	—
31R-2	390.74	11.64	97.0	—	—	—	—	—	—	—
32R-1	398.87	9.56	79.6	9.74	0.18	0.00	0.07	0.09	—	2.63
32R-2	399.95	11.26	93.8	—	—	—	—	—	—	—
33R-1	408.41	11.50	95.8	—	—	—	—	—	—	—
33R-2	409.45	11.90	99.2	—	—	—	—	—	—	—
33R-3	410.90	11.15	92.9	—	—	—	—	—	—	—
34R-1	418.00	11.02	91.8	—	—	—	—	—	—	—
34R-2	419.48	9.49	79.0	9.34	0.00	0.00	0.00	0.17	—	—
34R-3	420.63	11.05	92.0	—	—	—	—	—	—	—

Notes: IC = inorganic carbon, TC = total carbon, TOC = total organic carbon, C/N = carbon/nitrogen, C/S = carbon/sulfur. — = not analyzed.

Table T12. Results of Rock-Eval analyses on sediments, Site 1194.

Core, section	Depth (mbsf)	T_{max}	S_1	S_2	S_3	HI	OI	TOC (wt%)
194-1194A-								
1H-2	2.20	383	0.01	0.03	5.72	200	45,400	0.01
2H-2	6.90	400	0.07	0.27	5.96	142	3,136	0.19
2H-4	9.90	411	0.15	0.49	0.64	168	220	0.29
2H-6	12.90	406	0.11	0.47	5.15	162	1,775	0.29
3H-2	16.40	410	0.08	0.49	4.81	196	1,924	0.25
3H-4	19.40	402	0.11	0.46	5.98	135	1,758	0.34
3H-6	22.40	401	0.09	0.37	4.93	142	1,896	0.26
4H-2	25.90	401	0.11	0.36	24.08	109	7,296	0.33
4H-4	28.90	408	0.14	0.57	8.39	142	2,097	0.40
4H-6	31.90	410	0.10	0.54	25.34	150	7,038	0.36
5H-2	35.40	388	0.14	0.37	22.55	77	4,697	0.48
5H-4	38.40	405	0.28	0.37	1.96	119	632	0.31
5H-6	41.40	409	0.06	0.30	8.17	136	3,713	0.22
6H-2	44.90	398	0.07	0.35	4.84	120	1,668	0.29
6H-6	50.90	402	0.13	0.44	6.43	104	1,530	0.42
7H-2	54.40	405	0.09	0.44	22.99	137	7,184	0.32
7H-4	57.40	409	0.11	0.52	13.54	179	4,668	0.29
7H-6	60.40	395	0.06	0.24	22.63	82	7,803	0.29
8H-2	63.90	401	0.08	0.30	20.33	136	9,240	0.22
8H-4	66.90	394	0.09	0.17	4.02	100	2,364	0.17
8H-6	69.90	387	0.11	0.36	23.32	112	7,287	0.32
9H-2	73.40	400	0.08	0.35	16.50	87	4,125	0.40
9H-4	76.40	412	0.08	0.51	4.96	188	1,837	0.27
9H-6	79.40	394	0.08	0.35	18.98	112	6,122	0.31
10H-2	82.90	396	0.06	0.21	13.19	77	4,885	0.27
10H-4	85.90	400	0.08	0.38	6.19	80	1,317	0.47
10H-6	88.90	401	0.05	0.28	15.42	103	5,711	0.27
11H-2	92.40	402	0.05	0.25	11.59	138	6,438	0.18
11H-4	95.40	404	0.08	0.17	2.91	100	1,711	0.17
11H-6	98.40	397	0.06	0.24	7.80	75	2,437	0.32
12H-2	101.90	396	0.06	0.27	15.68	112	6,533	0.24
12H-4	104.90	400	0.04	0.26	1.99	136	1,047	0.19
12H-6	107.90	406	0.06	0.36	6.36	150	2,650	0.24
13H-2	111.40	404	0.06	0.16	3.69	160	3,690	0.10
13H-4	114.40	411	0.05	0.26	0.00	162	0	0.16
14X-1	118.15	—	0.03	0.00	1.51	—	—	0.00
20X-1	160.61	368	0.04	0.01	0.41	—	—	0.00
194-1194B-								
2R-2	112.20	410	0.03	0.28	0.00	164	0	0.17
2R-4	115.00	411	0.04	0.28	3.46	164	2,035	0.17
3R-1	120.37	398	0.03	0.05	0.41	29	241	0.17
4R-1	129.64	347	0.07	0.03	0.00	35	0	0.07
5R-1	139.24	395	0.09	0.11	0.08	73	53	0.15
6R-1	148.90	401	0.10	0.11	0.00	137	0	0.08
6R-2	149.98	404	0.11	0.22	0.00	157	0	0.14
7R-1	159.07	392	0.06	0.07	0.00	140	0	0.05
8R-1	168.41	393	0.05	0.07	1.02	162	2,535	0.04
8R-2	169.56	400	0.03	0.10	0.00	142	0	0.07
9R-1	177.43	397	0.31	0.31	21.91	81	5,765	0.38
10R-1	187.30	393	0.39	0.37	5.90	94	1,512	0.39
10R-3	189.75	398	0.22	0.19	0.00	126	0	0.15
11R-1	196.92	415	0.11	0.15	4.98	125	4,150	0.12
12R-1	206.50	395	0.00	0.13	0.00	185	0	0.07
13R-1	215.80	398	0.09	0.12	0.00	200	0	0.06
14R-CC	225.40	422	0.07	0.21	0.00	300	0	0.07
15R-1	235.40	383	0.14	0.14	3.48	65	1,694	0.21
16R-1	244.60	392	0.12	0.25	0.00	227	0	0.11
17R-1	254.54	387	0.15	0.10	0.90	90	818	0.11
17R-2	255.97	408	0.12	0.11	1.11	183	1,850	0.06
18R-CC	264.19	407	0.07	0.10	0.00	200	0	0.05
19R-1	273.77	396	0.11	0.29	12.04	263	10,945	0.11
20R-1	283.46	405	0.08	0.11	2.79	275	6,975	0.04
21R-1	293.25	423	0.13	0.29	1.11	263	1,009	0.03
22R-1	302.69	408	0.12	0.17	7.81	121	6,004	0.14
23R-1	312.76	394	0.08	0.07	6.00	67	5,459	0.11
24R-1	322.28	409	0.08	0.09	5.65	141	9,408	0.06
24R-2	323.63	393	0.35	0.18	10.50	67	3,537	0.27
25R-1	331.84	413	0.05	0.20	6.64	109	4,489	0.18
25R-3	334.37	414	0.05	0.21	6.22	109	3,125	0.20
25R-5	336.94	407	0.04	0.21	0.00	100	0	0.21
26R-1	341.32	413	0.07	0.19	0.00	172	0	0.11
26R-3	344.08	404	0.17	0.19	1.76	135	1,257	0.14
26R-5	346.58	401	0.09	0.08	0.85	114	1,214	0.07
27R-6	352.05	414	0.09	0.13	1.41	173	1,570	0.09
28R-1	360.16	408	0.13	0.25	1.22	166	813	0.15
28R-5	365.45	409	0.05	0.24	1.59	141	935	0.17
29R-1	369.87	412	0.07	0.32	1.27	213	846	0.15
29R-3	372.48	410	0.08	0.22	4.19	169	3,223	0.13
30R-1	379.78	408	0.05	0.13	1.05	216	1,750	0.06
30R-3	382.71	398	0.02	0.17	0.00	106	0	0.16
31R-1	389.30	389	0.01	0.07	1.60	200	6,521	0.03
31R-2	390.74	402	0.04	0.05	0.71	166	2,366	0.03
32R-1	398.87	410	0.02	0.09	0.00	112	0	0.08
32R-2	399.95	410	0.01	0.04	1.07	142	4,385	0.03
33R-3	410.90	412	0.05	0.19	1.29	158	1,075	0.12
34R-2	419.48	403	0.10	0.06	0.00	85	0	0.07
34R-3	420.63	—	0.07	0.01	2.34	50	23,400	0.01

Notes: T_{max} = temperature of maximum hydrocarbon generation during pyrolysis in °C, S_1 = milligrams of free hydrocarbons per gram of rock, S_2 = milligrams of pyrolyzed hydrocarbons per gram of rock, S_3 = milligrams of carbon dioxide per gram of rock, HI = hydrogen index in milligrams of hydrocarbon per gram of TOC, OI = milligrams of carbon dioxide per gram of TOC, TOC = total organic carbon. — = not available.

Table T13. Summary of logging operations, Hole 1194B.

Date (Jan 2001)	Time (local)	Comments
25	0530	Hole preparation complete. Rig up wireline.
	0715	RIH with MGT-HNGS-APS-HLDS-DITE (+TAP).
	0755	Uplog with triple combo at 900 ft/hr from 425 mbsf to seafloor. Rig into hole to TD.
	0950	Uplog with MGT at 700 ft/hr from 425 to 75 mbsf. Rig into hole for short repeat.
	1135	Uplog with MGT at 700 ft/hr from 134.5 to 65 mbsf. Pull out of hole.
	1345	Rig up NGT-DSI-FMS.
	1425	RIH with NGT-DSI-FMS.
	1515	Uplog at 900 ft/hr from 425 mbsf to pipe. Pull out of hole.
	1630	Rig up NGT-LSS-FMS.
	1810	Uplog at 900 ft/hr from 425 to pipe. Pull out of hole.
	2130	Rig up WST.
	1045	Tight spot prevents the tool from going deeper than 157 mbsf. Start check shots.
	1150	Pull out of hole and rig down.
26	0030	End of logging operations.

Notes: RIH = run in hole, MGT = Lamont multisensor gamma ray tool, HNGS = hostile-environment natural gamma ray sonde, APS = accelerator porosity sonde, HLDS = high-temperature lithodensity sonde, DITE = dual induction tool, TAP = high-temperature/acceleration/pressure tool. TD = total depth. NGT = natural gamma ray tool, DSI = dipole shear sonic imager, FMS = Formation MicroScanner, LSS = long-spaced sonic tool, WST = well seismic tool. Drillers total depth = 427.1 mbsf, water depth = 384.8 mbrf, end of pipe = 78.93 mbsf.